# INAUGURAL – DISSERTATION

zur
Erlangung der Doktorwürde
der
Naturwissenschaftlich-Mathematischen
Gesamtfakultät
der
Ruprecht-Karls-Universität
Heidelberg

vorgelegt von
M. Sc. Nikolaus Wollscheid
aus Trier

Tag der mündlichen Prüfung: 18. Dezember 2020

# The Ultrafast Singlet Fission Dynamics in Solution and Thin Film

Gutachter: Dr. Tiago Buckup

Prof. Dr. Andreas Dreuw

**Abstract:**

Singlet fission (SF) is a process where two triplet charge-carriers are generated from one photoexcited singlet state. This opens up the possibility to increase the efficiency limit for single-junction solar cells by one third from 33% to 44%. In this work, the long-lasting question of the effect of competing pathways on the efficiency of SF is addressed by time-resolved spectroscopy and a novel global fit approach. This is demonstrated on two examples. First, SF is established in a new class of molecules, the tetraazaperopyrenes. Here, substituent-dependent factors, namely excimer formation as well as vibronic and spin-orbit coupling, are identified to be decisive for SF efficiency. Subsequently, solutions of (hetero-) acenes are investigated, in which comparisons between ambient conditions and deaerated solutions highlight the importance of molecular oxygen for SF: A new, sequential mechanism including atmospheric oxygen as a catalyst is resolved, which allows for a step-wise doubling of triplet states even at low chromophore concentrations. In concentrated solutions, diffusion-controlled SF outcompetes other reaction pathways resulting in triplet yields close to 200%. The absence of any intermediate species emphasises the efficiency of this process.

**Kurzzusammenfassung:**

Singulettspaltung (SF) ist ein Prozess, durch den zwei Triplett-Ladungsträger aus einem angeregten Singulettzustand erzeugt werden. Diese Ladungsträgervervielfachung birgt das Potential, das theoretische Effizienzlimit für Solarzellen um ein Drittel von 33% auf 44% zu steigern. Die vorliegende Arbeit beschäftigt sich mit der Frage, welchen Einfluss Konkurrenzprozesse auf die Effizienz von SF haben. Hierfür wird zeitaufgelöste Spektroskopie und ein neuer Ansatz für eine globale Anpassung verwendet. Die Herangehensweise wird an zwei Beispielen demonstriert. Zunächst wird SF in einer neuen Klasse von Molekülen, den Tetraazaperopyrenen, nachgewiesen. Für diese werden drei von den Substituenten beeinflusste Faktoren identifiziert, welche von entscheidender Bedeutung für die Effizienz von SF sind. Diese sind die Bildung von Exzimerzuständen sowie vibronische und Spin-Bahn-Kopplung. Im Anschluss daran werden Lösungen von (Hetero-) Acenen untersucht, für welche der Vergleich zwischen Umgebungs- und sauerstofffreien Bedingungen die Signifikanz von molekularem Sauerstoff herausstellt: Ein neuer, sequentieller SF Mechanismus mit Luftsauerstoff als Katalysator wird aufgeklärt, welcher zu einer schrittweisen Verdoppelung der Triplettzustände führt. In konzentrierten Lösungen übertrifft diffusionskontrollierte SF andere Reaktionswege, was zu Triplettausbeuten von knapp 200% führt. Die Abwesenheit von Intermediaten unterstreicht die Effizienz dieses Prozesses.

# Publications:

*Diffusion-Controlled Singlet Fission in a Chlorinated Phenazinothiadiazole by Broadband Femtosecond Transient Absorption*. Wollscheid, N.; Lustres, J.L.; Brosius, V.; Motzkus, M.; Bunz, U.H.F; and Buckup, T.; Journal of Physical Chemistry B, *accepted,* DOI: 10.1021/acs.jpcb.0c05056

*Ultrafast Singlet-Fission and Intersystem Crossing in Halogenated Tetraazaperopyrenes.* Wollscheid, N.; Günther, B.; Rao, V.; Berger, F.; Lustres, J.L.; Motzkus, M.; Zaumseil, J.; Gade, L.; Höfener, S.; and Buckup, T.; Journal of Physical Chemistry A **2020**, 124 (39), 7857-7868.

*Oxygen-catalysed sequential singlet fission*. Wollscheid, N.*; Lustres, J.P.L.*; Kefer, O.; Hahn, S.; Brosius, V.; Bunz, U.H.F.; Motzkus, M.; and Buckup, T.; Nature Communications, **2019**, 10, Art. Numb. 5202. *Authors contributed equally to this work.

*Charge Transfer from Photo-Excited Semiconducting Single-Walled Carbon Nanotubes to Wide-Bandgap Wrapping Polymer.* Kuang, Z.; Berger, F. J.; Lustres, J.L.P.; Wollscheid, N.; Li, H.; Lüttgens, J.; Balci Leinen, M.; Flavel, B. S.; Zaumseil, J.; and Buckup, T.; *submitted*.

*Singlet Fission in Tetraaza-TIPS-Pentacene Oligomers: From fs Excitation to µs Triplet Decay via the Biexcitonic State*. Alagna, N.; Lustres, J.L.P.; Wollscheid, N.; Luo, Q.; Han, J.; Dreuw, A.; Geyer, F.L.; Brosius, V.; Bunz, U.H.F.; Buckup, T.; and Motzkus, M.; Journal of Physical Chemistry B, **2019**, 123 (50), 10780–10793.

*Tailoring Ultrafast Singlet Fission by the Chemical Modification of Phenazinothiadiazoles.* Alagna, N.; Han, J.; Wollscheid, N.; Lustres, J.L.P.; Herz, J.; Hahn, S.; Koser, S.; Paulus, F.; Bunz, U.H.F.; Dreuw, A.; Buckup, T.; and Motzkus, M.; Journal of the American Chemical Society, **2019**, 141, 8834-8845.

*Substituting Coumarins for Quinolinones: Altering the Cycloreversion Potential Energy Landscape.* Paul, N.; M. Jiang, N.; Bieniek, Lustres, J.L.P; Li, Y; Wollscheid, N; Buckup, T; Dreuw, A; Hampp, N; and Motzkus, M; Journal of Physical Chemistry A, **2018**, 122, 7587-7597.

# Conference Contributions

*Tracking Homogeneous and Heterogeneous Carrier Multiplication via Singlet Fission in Solution.* Wollscheid, N.; Lustres, J.L.P.; Kefer, O.; Buckup, T.; and Motzkus, M.; Conference on Lasers and Electro-Optics/Europe 2019, München, Germany.

*Investigating diffusion controlled singlet fission of a chlorinated phenazinothiadiazole.* Wollscheid, N.; Alagna, N.; Lustres, J.L.P.; Brosius, V.; Geyer, F.; Bunz, U.; Buckup, T.; and Motzkus, M.; DPG Frühjahrstagung 2019, Regensburg, Germany.

*Diffusion Controlled Singlet Fission of a Phenazinothiodiazole in Solution.* Wollscheid, N.; Alagna, N.; Lustres, J.L.P.; Buckup, T.; Hahn, S.; Bunz, U.H.F.; and Motzkus, M.; 2nd International Symposium on Singlet Fission and Photon Fusion 2018, Gothenburg, Sweden.

*Diffusion controlled singlet fission of a tetracene derivative in solution.* Wollscheid, N.; Alagna, N.; Lustres, J.L.P.; Buckup, T.; Hahn, S.; Bunz, U.H.F.; and Motzkus, M.; DPG Frühjahrstagung 2018, Erlangen, Germany.

# Table of Contents

# List of Abbreviations

| | |
|---|---|
| CA | Coherent artefact |
| CPM | Cross-phase modulation |
| CT | Charge transfer |
| DADS | Decay associated difference spectrum |
| DFT | Density functional theory |
| ESA | Excited state absorption |
| ESR | Electron spin resonance |
| FFT | Fast Fourier transform |
| FWHM | Full width at half maximum |
| GSB | Ground state bleach |
| HOMO | Highest occupied molecular orbital |
| HONO | Highest occupied natural orbital |
| IC | Internal conversion |
| IRF | Instrument response function |
| ISC | Intersystem crossing |
| iSF | Intramolecular singlet fission |
| IVS | Impulsive vibrational spectroscopy |
| LUMO | Lowest occupied molecular orbital |
| LUNO | Lowest occupied natural orbital |
| NOPA | Non-collinear optical parametric amplifier |
| PAH | Polycyclic aromatic hydrocarbon |
| SADS | Species associated difference spectrum |
| SE | Stimulated emission |
| SF | Singlet fission |
| SRA | Stimulated Raman amplification |
| SSA | Singlet-singlet annihilation |
| TA | Transient absorption |
| TCSPC | Time-correlated single photon counting |
| TPA | Two-photon absorption |
| tr-ESR | Time-resolved electron spin resonance |
| TTA | Triplet-triplet annihilation |
| VCS | Vibrational coherence spectroscopy |

# 1 Motivation

Out of the ten years with the highest average temperature in Germany, nine occurred since the start of the 21st century.[1] This clearly shows the impact of climate change. In order to combat this, Germany and 194 other countries signed the Paris Agreement in 2015, in which they commit themselves to limit global warming to 1.5 °C above pre-industrial levels.[2] This aim can only be achieved if energy production is shifted to carbon-neutral, renewable sources. Hereof, a promising candidate is photovoltaics, whose contribution to the total power consumption in Germany has increased drastically from 0.2% in 2005 to 8.2% in 2019 (Figure 1.1).[3] Over the same time period, the cost of solar modules has decreased by about 75 %. Combined with the increasing scarcity and bad image of fossil fuels, prices of power generated by photovoltaics have become competitive. A decisive parameter in photovoltaics is the conversion efficiency, with modern commercially available solar cells averaging about 17.5%.[4] While technological improvements result in a steady increase of this number, there is a physical limitation. This is based on the bandgap of the utilised semiconductors, of which the most widespread is silicon. Here, the energy difference between valence and conduction band amounts to 1.12 eV, allowing for about 80 % of the solar spectrum to be covered (Figure 1.2). However, incident photons with an energy exceeding the band gap will result in excess heat being generated in the semiconductor due to thermalization.

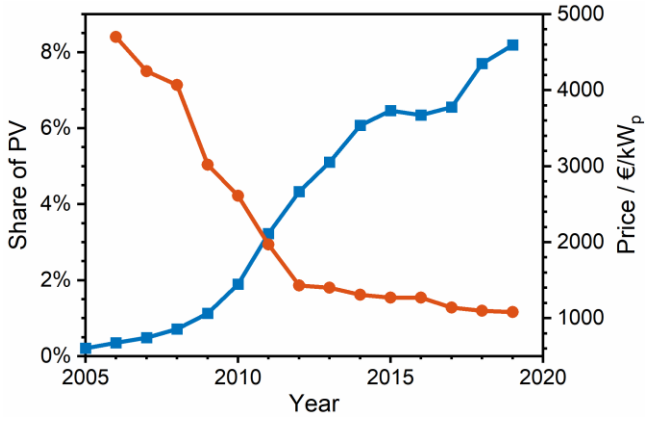


***Figure 1.1:*** *The share of photovoltaics in the total power consumption in Germany shows a steady increase from 0.2 % in 2005 to 8.2 % in 2019 (blue line). Simultaneously, the average price for rooftop photovoltaic systems (orange line) decreased from 4700 to 1080 €/kW$_p$, which contributes to the increasing competitiveness of power generated by photovoltaics.*[3-4]

This is the main contributor to the so-called Shockley-Queisser limit, *i.e.*, the maximum conversion efficiency of 33% for silicon-based solar cells.[5] Charge-carrier multiplication processes, during which a high-energy photon is converted into two charge carriers of lower energy, are envisioned to overcome these thermalization losses. A prominent example of this is singlet fission (SF).[6-7] Here, an incident energy-rich photon promotes an organic chromophore to its excited singlet state. Upon interaction with a second chromophore, two triplet excitons of lower energy are created. Subsequently, these electron-hole pairs are separated to generate two free charge carriers, which can be transferred to a semiconductor. In consequence, SF allows to efficiently harvest the blue part of the solar spectrum hence mitigating thermalization losses and raising the Shockley-Queisser limit by one third to 44% under ideal circumstances.[8] The feasibility of this approach has been proven experimentally with reported photon-to-electron conversion rates exceeding 100%.[9-10] In order to achieve efficient SF, triplet has to outcompete other reaction channels of the excited chromophore $A^*$, which can be broadly categorised into intra- and intermolecular pathways (Figure 1.3). Intramolecular processes only contain the excited chromophore as an active species. Consequently, they are molecule-specific, and their timescales can in general not be significantly altered without chemical modification. Examples are re-formation of the ground state *via* non-radiative transitions or fluorescence, both of which typically occur on the nanosecond timescale.

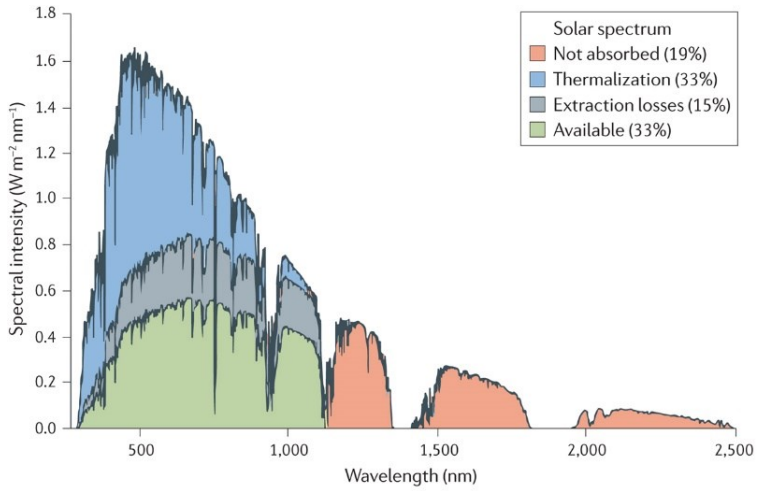


***Figure 1.2:*** *Loss channels leading to efficiency losses in solar cells. Low-energy photons are not absorbed by silicon. In contrast, high-energy photons result in excess energy being deposited into the semiconductor, which is dissipated as heat. This thermalization is the main loss channel for silicon solar cells, which leads to an upper efficiency limit of 33%. Reprinted with permission from ref. 11. Copyright © 2017, Macmillan Publishers Limited.*

In addition, the excited chromophore may undergo intersystem crossing (ISC), resulting in a single triplet exciton. Finally, a photoreaction may occur, which can be completed on the sub-picosecond timescale, as exemplified by the photoisomerization of retinal.[12] In turn, intermolecular pathways require an interaction between two reactants. If a reaction system contains only the chromophore itself as a reactive species, possible bimolecular channels competing with SF are either dimerization or excimer formation. However, when working under ambient conditions, interactions of the chromophore with molecular oxygen have to be considered. Most notably for this work, this includes the sensitisation of molecular oxygen from its triplet ground state ($^3O_2$) to the reactive singlet oxygen species ($^1O_2$).[13-14] Crucial parameters for the rates of intermolecular pathways are on the one hand the concentration of the reactants and on the other hand inter-chromophore geometry. The effects of both parameters further depend on the physical state of the reaction system.

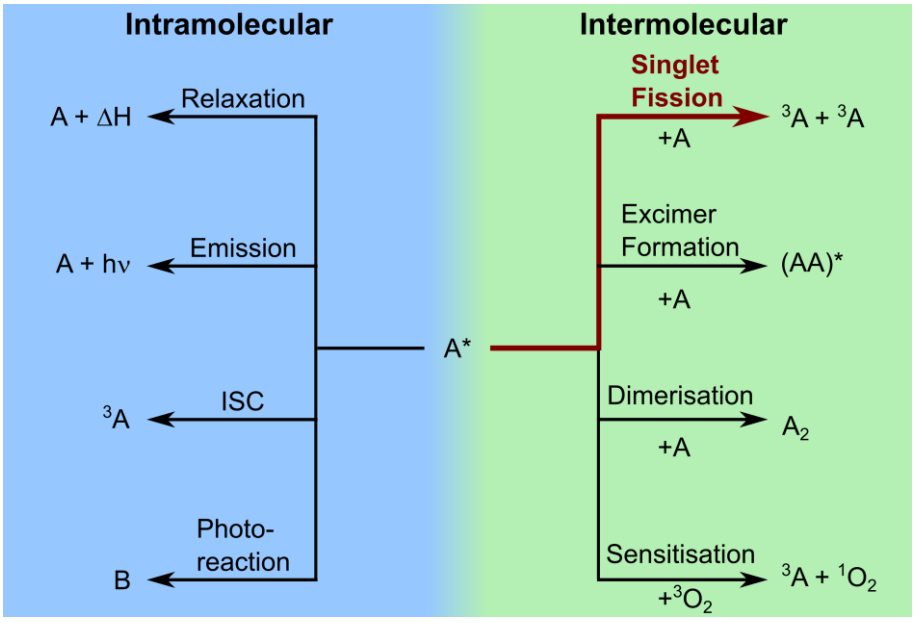


***Figure 1.3:*** *Overview of selected pathways of an excited chromophore* $\boldsymbol{A}^*$ *competing with SF, grouped into intra- and intermolecular processes. Examples for intramolecular pathways are the re-formation of the ground state* ***A*** *either via non-radiative relaxation or fluorescence. In addition, the chromophore can undergo ISC, resulting in a triplet chromophore* $^3A$*. Finally, the reactant may undergo a photochemical reaction to a different molecular species. Intermolecular pathways include the reversible formation of a weakly-bound excimer state* $(\boldsymbol{AA})^*$*. Unlike for dimerization, no new covalent bonds are formed. The final intermolecular pathway includes atmospheric molecular oxygen (*$^3O_2$*). Upon interaction with the excited chromophore,* $^3\boldsymbol{A}$ *and a reactive singlet oxygen species (*$^1O_2$*) are generated.*

In the solid state, the densely packed chromophores are within contact distance. Thus, an efficient interaction of reactants and in consequence high rates are expected. However, the individual chromophores in a molecular crystal are immobilized with a well-defined inter-chromophore geometry. Thus, if this geometry is unfavourable, processes can be decelerated or even inhibited. In contrast, dissolved reactants possess more degrees of freedom. Consequently, they can orientate themselves in a favourable geometry before a reaction occurs. However, the frequency of chromophore interactions is governed by diffusion, which may allow intramolecular pathways to become competitive.

The effects of these general implications have been observed in SF. For example, sub-ps rate constants were observed for SF in crystalline samples[15-18] with them being highly dependent on the inter-chromophore geometry.[19-21] In addition, depending on the packing motif, excimer formation is encourage or prevented as a competing pathway.[22-24] In solution, SF is diffusion-controlled, which necessitates a careful evaluation of competing intramolecular processes.[25-27] Furthermore, it has been shown that the effect of molecular oxygen on chromophore dynamics should not be underestimated, as it opens up additional pathways.[28-29] This stresses that in order to achieve efficient SF, a careful optimisation of molecular properties and experimental parameters is required.

In this thesis, time-resolved spectroscopy is employed to investigate ultrafast SF dynamics in solution and solid state. Competitive processes reducing SF efficiencies are identified. In an effort to increase the overall triplet yield, possibilities on how to avoid them are suggested. The thesis is subdivided into the following chapters:

- In **chapter 2**, fundamentals of SF are explained and crucial variables responsible for an efficient triplet generation pointed out. This is followed by examples of how these features can be tuned to achieve highest efficiencies.
- **Chapter 3** details the sample preparation and main experimental techniques used throughout this thesis. Special focus is laid on the processing and analysis of the multidimensional transient absorption data. A global multiexponential fit approach is developed and applied to disentangle the non-trivial photophysics of SF.

- **Chapter 4** establishes ultrafast SF in a new class of molecules. First, investigations of dilute solutions are carried out to gain insight into spectral features of electronic species and intramolecular processes. This knowledge is used to identify the coherent formation of the correlated triplet pair and its subsequent dissociation in solid state. In addition, connections between efficient SF and competing excimer formation as well as vibronic coupling are drawn.
- In **chapter 5**, solution-based SF is investigated. It is demonstrated that at low to intermediate chromophore concentrations, molecular oxygen can be used as a catalyst to greatly enhance triplet yields in a sequential SF process. In addition, high chromophore concentrations are demonstrated to outcompete intramolecular deactivation pathways, leading to quantitative SF.
- The observations made for the different reaction systems will be summarized in **chapter 6**. Decisive parameters for efficient SF are pointed out and potential improvements for future development are suggested.

# 2 Photophysics of Singlet Fission

## 2.1 Introduction and Basic Concepts

SF describes the conversion of one singlet exciton into two triplet excitons. During this process, the overall spin is conserved, allowing for SF to occur on ultrafast timescales. SF was originally invoked as the reverse process of triplet-fusion to explain unexpectedly low fluorescence quantum yields in anthracene and tetracene crystals.[30-31] However, despite SF being demonstrated in other materials such as perylene[19] and a polydiacetylene,[32] the interest in this unique phenomenon slowly faded away. This changed in 2006, when Hanna and Nozik published a study in which the use of SF in photovoltaics was pointed out.[8] Based on SF being a multiple exciton generation process, they calculated that the combination of an organic SF material with silicon solar cells may increase the Shockley-Queisser efficiency limit for single-junction solar cells[5] by one third from 33 to 44%. This prospect led to a massive increase in research interest, which was summarized in a seminal review of Smith and Michl in 2010.[6] Here, the authors presented the state-of-the art understanding of the SF mechanism as well as design guidelines for efficient SF chromophores. While this review was published ten years ago, many of its core statements still hold true. Since then, progress on SF has been summarized in a number of reviews focusing on different aspects of SF, *e.g.* its theoretical modelling[33], applications in photovoltaic devices,[11] mechanistic studies,[34-36] or design principles of chromophores.[37-38]

Early reports on the SF mechanism in (poly-) crystalline solids authored by Merrifield suggested the presence of an intermediate triplet pair $^1(TT)$.[39] This multiexciton state describes two triplet states located on neighbouring chromophores, which are electronically coupled to yield an overall singlet spin state. Upon separation of the correlated triplet pair, two independent ("free") triplet states are generated (Figure 2.1a):

$$S_1 + S_0 \leftrightharpoons {}^1(TT) \rightleftharpoons T_1 + T_1 \qquad \text{Eq. 1}$$

While this model experienced widespread acceptance, varying interpretations on the nature of the intermediate required a more detailed description of the process. In consequence, Scholes proposed an extended perspective on the correlated triplet pair.[40] He suggested to discern between two different types of triplet pairs: First, the correlated triplet pair $^1(TT)$ is formed, which is characterised by a significant orbital overlap of the constituent triplets. Upon electronic decoherence, *e.g.*, due to spatial separation or coupling to the phonon bath, a second triplet pair, labelled $(T \cdots T)$, is formed. While not necessarily being located on adjacent chromophores anymore, the spins of both constituent triplets remain entangled. Finally, as soon as spin thermalization occurs, two separate ("free") triplets $T_1$ are generated. Following this approach, the SF mechanism is written as

$$S_1 + S_0 \leftrightharpoons {}^1(TT) \leftrightharpoons (T \cdots T) \rightleftharpoons T_1 + T_1 \qquad \text{Eq. 2}$$

Since its inception, the validity of this model has been experimentally verified on several occasions.[28-29, 34, 41-42] This also raises the question as to which state constitutes the formal "end" of SF. The importance is seen for a variety of polycyclic aromats, which exhibit a formation of the $^1(TT)$ state on timescales below 100 fs, but in some cases also a rapid recombination to the excited singlet.[7, 15-16, 21, 41, 43-46] Thus, it is most sensible to define SF not as the formation of $^1(TT)$ but of $(T \cdots T)$, as the latter lacks the strong inter-chromophore coupling.[40] However, especially for older reports, this definition is not always adhered to. A further, recently emerged aspect of SF deals with the overall spin of the correlated triplet pair. Due to the interaction of the spins of the two constituent triplets, different overall spin states can be generated. The origins as well as the implications of this effect will be discussed in more detail in section 2.1.2.

A crucial prerequisite for SF to occur is the adherence to the law of the conservation of energy (Figure 2.1b). This means, that the energy of the excited singlet has to be equal or higher than twice the energy of the triplet state, leading to the energy matching criterion

$$\Delta E_{\mathrm{SF}} = E(S_1) - 2\,E(T_1) \geq 0 \qquad \text{Eq. 3}$$

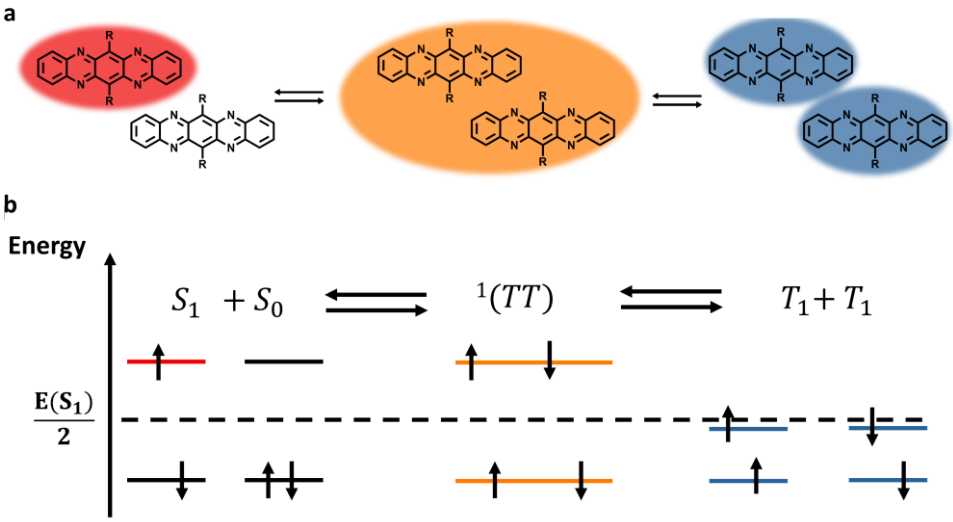


***Figure 2.1:*** *a) Schematic representation of SF. Upon photoexcitation, the locally excited singlet (**$S_1$**, red) interacts with a ground state chromophore to generate the correlated triplet pair (**$^1(TT)$**, yellow). After decorrelation, two free triplets (**$T_1$**, blue) are generated. b) During SF, the energy conservation law has to be adhered to. Consequently, the energy of the excited singlet must be equal or higher than two times the triplet state.*

However, the efficiency of SF does not exclusively hinge on large values for $\Delta E_{SF}$, which can be seen in two selected examples. In a tetracene derivative, $^1(TT)$ is formed coherently despite an endothermic SF energy balance.[47] Contrarily, low SF rates are observed in rubrene despite favourable energetics.[46] In order to understand this seemingly contradictory behaviour, two closely connected properties have to be considered: the electronic coupling between $S_1+S_0$ (in the following labelled $S_1S_0$) and $^1(TT)$ (section 2.1.1) as well as vibrational dynamics (section 2.1.3).

While an efficient formation of the correlated triplet pair outcompetes other loss channels like emission or non-radiative relaxation, it does not automatically result in a high yield of free triplets due to the reversibility of the process. Thus, an equilibrium between $S_1S_0$ and $^1(TT)$ is formed. In consequence, delayed fluorescence is introduced as an additional loss channel.[28-29, 48] Additionally, a weak direct photoluminescence from $^1(TT)$ has been reported, which may lower the triplet yield.[47] Furthermore, the two constituent triplets of any of the two triplet pairs may undergo triplet-triplet annihilation (TTA).[21, 29] This results in the loss of a triplet excitation, effectively halving the overall yield. In total, both processes demonstrate the

importance of efficiently separating the correlated triplet pair. This can be difficult to achieve in molecular crystals, as the chromophores possess a fixed structure with a well-defined geometry. In consequence, the separation of $^1(TT)$ is driven by the diffusion of its constituent triplets. This may, however, be hindered by the energetic stabilisation of the correlated triplet pair with regard to the free triplets (*cf.* section 2.1.2) or low-lying trap states.[47] In contrast, solution-based SF enables the chromophores to diffuse apart immediately after SF occurs and to overcome the binding energy by collisions with solvent molecules. Depending on the strength of its stabilisation, $^1(TT)$ may be detected as a short-lived intermediate.[25-26] However, the viability of SF becomes strongly dependent on the timescales of competing processes which deactivate the excited state. A more detailed discussion of diffusion-controlled SF in solution will be made in section 2.1.4.

While so far, SF has been described as an intermolecular process between two separated molecules, it is also possible to design molecules with two or more chromophores. This approach retains short inter-chromophore distances as found in molecular crystals, allowing for intramolecular SF (iSF) to occur. In addition, due to the variety of possible chemical modifications, important parameters for SF such as electronic coupling or inter-chromophore geometry can be finely tuned. This substantially increased the understanding *e.g.* of the separation of $^1(TT)$ and the role of charge transfer (CT) states in SF. Observations of iSF and the ensuing conclusions will be reviewed in section 2.2.3.

### 2.1.1 Electronic Coupling

As mentioned in the previous section, the electronic coupling between $S_1S_0$ and $^1(TT)$ significantly influences SF dynamics. Its importance can be derived by prevalent models predicting reaction rates. According to Fermi's golden rule, the transition rate between two electronic states is directly proportional to the square of their electronic coupling.[49] For SF, the states in question are the initial $S_1S_0$ and $^1(TT)$. In a diabatic framework, their coupling strength is obtained as the off-diagonal element of the

electronic Hamiltonian and correlates to the overlap of their respective wavefunctions.[33] However, it has been demonstrated that higher order perturbations, *i.e.*, superexchange coupling involving a virtual CT state, have to be considered to accurately predict SF rates (Figure 2.2).[21, 50] This second-order perturbation has been proposed to allow for efficient SF despite unfavourable alignment of singlet and triplet energy levels.[20, 51-52] In some studies, the CT state has been observed as a real intermediate within the SF mechanism.[53-55] Pinpointing the exact role of CT states in SF is still an active field of research.[36]

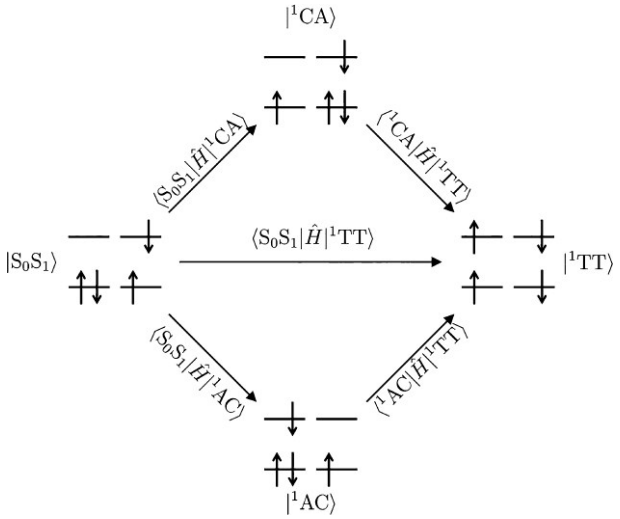


***Figure 2.2**: Electronic coupling between states involved in SF. In a direct coupling model, the excited singlet state $|\boldsymbol{S_0S_1}\rangle$ is only connected to the correlated triplet pair $|\boldsymbol{^1TT}\rangle$. However, it has been shown that the involvement of superexchange contributions via CT states ($|\boldsymbol{^1CA}\rangle$, $|\boldsymbol{^1AC}\rangle$) has to be considered to accurately predict SF rates. Reprinted with permission from ref. 33. Copyright © 2018, American Chemical Society.*

## 2.1.2 Electronic Structure of the Correlated Triplet Pair

The significance of electronic coupling values hinges on the correct modelling of the involved states. While this can be readily achieved for $S_1S_0$, new approaches are needed for $^1(TT)$. In a first-order approximation, $^1(TT)$ can be viewed as a doubly excited state involving four electrons in total. As such, spin-interactions play an important role in deriving the electronic structure. Two common methods to construct the wavefunction of $^1(TT)$ are the 9- and 16-spin state approach. Both procedures as well as their limitations will be briefly discussed at this point, while comprehensive explanations can be found in the literature.[6, 33-35, 37, 39-40]

The 9-spin state approach was originally proposed by Merrifield to explain TTA in oligoacene crystals.[39] Here, the correlated triplet pair is constructed as a linear combination of its two constituent triplet states. This yields nine orthonormal spin functions, in which the individual triplets couple to varying spin states. In total, these include one singlet $^1(TT)$, three triplet $^3(TT)$ and five quintet states $^5(TT)$.[37] While in general, the singlet state will be of the lowest energy, the respective energy between the different spin states is determined by the strength of inter-triplet coupling. In systems with weak triplet interactions, the individual spin states become energetically close. In contrast, a strongly coupled system will result in a stabilisation of the singlet state and introduce a binding energy for the triplet pair, which has to be overcome for free triplet states to be generated. This poses a dilemma for SF, given that the previous step, the formation of the correlated triplet pair, is also more efficient for strongly coupled systems. Thus, a delicate balance of the inter-triplet interactions must be found, which is one of the biggest challenges in SF.

The main limitation of the 9-spin state approach arises from its negligence of coherent contributions within the triplet pair, *i.e.*, its lacking representation of wave-function overlap. In consequence, inter-molecular two-electron exchange integrals are non-existent, leading to erroneous energies for the correlated triplet pair.[34] This inaccuracy is addressed in the 16-spin state approach. Here, the triplet pair is viewed as being comprised of four electrons located on two sites A and B. Thus, using the common notation of $|\alpha\rangle$ and $|\beta\rangle$ for spin-up and spin-down one-electron eigenstates, respectively, 16 different permutations are obtained as $|\alpha\alpha\alpha\alpha\rangle$, $|\alpha\alpha\alpha\beta\rangle$ … $|\beta\beta\beta\beta\rangle$ (Figure 2.3a). While these product states are no eigenstates of the four-electron spin operator, they represent a suitable basis set to construct the six spin eigenstates of the correlated triplet pair.[40] Of these pure spin wavefunctions, total multiplicities account for two singlet ($|S_1\rangle$, $|S_2\rangle$), three triplet ($|T_1\rangle$, $|T_2\rangle$, $|T_3\rangle$) and one quintet state $|Q\rangle$ (Figure 2.3b). Given that only $|S_1\rangle$ and $|Q\rangle$ will be relevant in the ensuing discussion of SF, the reader is referred to a recent review by Musser *et al.* for a detailed description for all six eigenstates.[35]

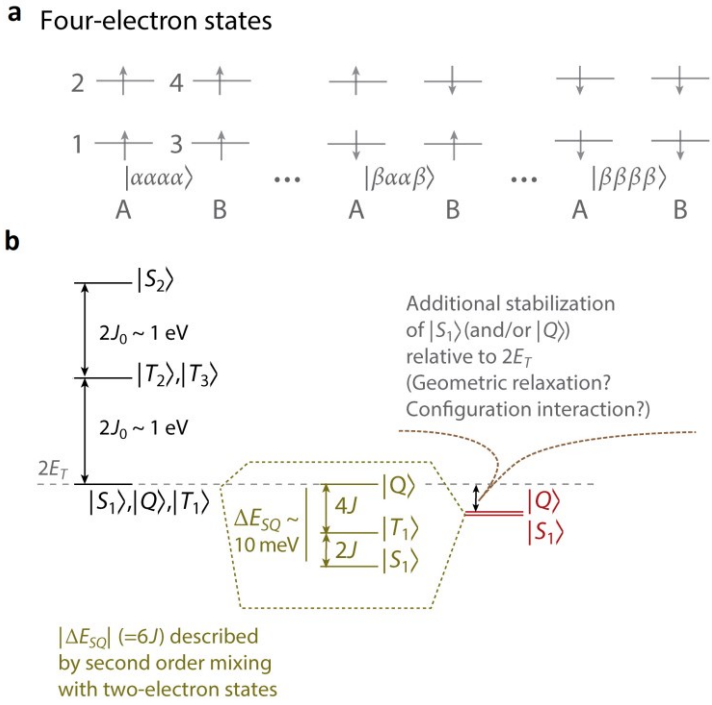


***Figure 2.3:*** *a) Four-electron product states used as a basis for the description of the eigenstates of the correlated triplet pair.* $|\alpha\rangle$ *and* $|\beta\rangle$ *denote the spin-up and spin-down one-electron eigenstates. b) Relative energies of the four-electron states.* $|S_1\rangle = {}^1(TT)$ *and* $|Q\rangle = {}^5(TT)$ *are described as a combination of a pair of triplet excitations. Considering the exchange interactions,* ${}^1(TT)$ *experiences a stabilisation of 6 J with regard to the energy of the two free triplet states* $2E_T$*.Adapted with permission from ref. 35. Copyright © 2019, Annual Reviews, Inc.*

In the framework of a weak interaction between the electrons at the sites A and B, the expressions for $|S_1\rangle$ and $|Q\rangle$ can be described as a combination of a pair of triplet excitations, showing the connection between this and the 9-spin state approach. Furthermore, both states, that is $|S_1\rangle = {}^1(TT)$ and $|Q\rangle = {}^5(TT)$, possess the same energy of two times the isolated triplet state ($2E_T$). However, if the interaction between the two constituent triplets is considered, the degeneracy between ${}^1(TT)$ and ${}^5(TT)$ is lifted. In the absence of spin-orbit coupling and external magnetic fields, the ensuing fine-structure originates from exchange interaction, characterised by the parameter $J$. Here, a stabilisation of ${}^1(TT)$ by 6 $J$ is expected, whereas ${}^5(TT)$ remains unaffected at an energy of $2E_T$. This energy difference constitutes the previously mentioned binding energy of ${}^1(TT)$. Recent studies quantified its value to be on the order of 10 meV.[56-58] While the 16-spin state approach depicts the nature of the correlated

triplet pair and its stabilisation with regard to the two free triplet states more accurate than the 9-spin state approach, it still is not without flaw.

For example, geometric relaxation or mixing with CT states is not considered, which may affect the relative and absolute energies of $^1(TT)$ and $^5(TT)$. First experimental evidence of the $^5(TT)$ was presented simultaneously by Weiss *et al.* and Tayebjee *et al.* with both studies employing time-resolved electron spin resonance (tr-ESR) experiments. [59-60] This method takes advantage of the Zeeman-effect, *i.e.*, the splitting of states with a multiplicity $S > 0$ into $2S + 1$ sublevels in the presence of a static magnetic field and probes the transitions between those states at varying delays after optical excitation. Weiss *et al*. investigated thin-films of a tetracene derivative, for which SF has been demonstrated.[47, 59] At room temperature, the observed tr-ESR signal originates from the individual triplets of $^1(TT)$ (Figure 2.4). In contrast, an additional signal was observed at low temperatures (10 K), which the authors attributed to the strongly exchange-coupled quintet state, proving the mutual existence of $^1(TT)$ and $^5(TT)$ states within the SF mechanism. Similar observations have been made by Tayebjee *et al.* in pentacene dimers linked by two and three phenylene moieties, respectively (BP2 and BP3).[60] At early times after optical excitation (20-100 ns), the ESR signal of BP3 is dominated by transitions within the quintet manifold

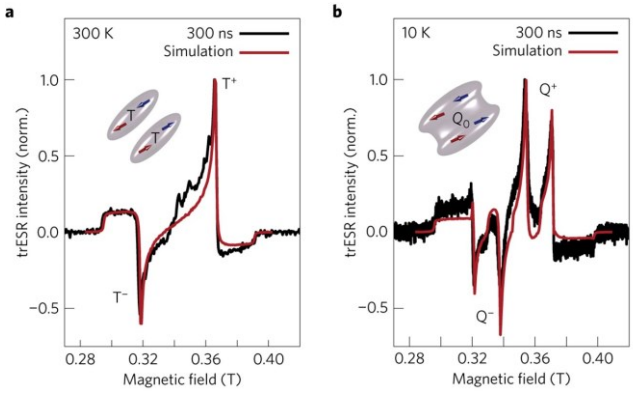


***Figure 2.4:*** *a) The signal obtained by time-resolved electron spin resonance (tr-ESR) in a tetracene thin film at room temperature shows a characteristic structure which originates from the constituent triplets of* $^1(TT)$. *b) In contrast, experiments carried out at low temperatures (10 K) exhibit an additional signal, which is assigned to the strongly exchange-coupled* $^5(TT)$. *Reprinted with permission from ref. 61. Copyright © 2016, Nature Publishing Group.*

. In turn, after several microseconds the signal is described as a combination of the $^5(TT)$ and dissociated triplets. For BP2, a stronger coupling of the triplet pair is observed, which the authors attributed to the shorter phenyl bridge. Here, no signal of the dissociated triplets is observed, as the triplet pair remains weakly coupled even on the microsecond timescale. This observation reiterates the non-trivial task of tuning the inter-triplet coupling to simultaneously allow for efficient SF and dissociation of the triplet pair, and is reinforced by a study conducted by Basel *et al*. on an adamantyl-linked pentacene dimer.[62] This linker breaks the conjugation and thus reduces the coupling between the individual chromophores while still allowing SF to occur. Expectedly, tr-ESR experiments demonstrated the same behaviour that was observed for BP3, *i.e.*, the decorrelation of $^5(TT)$ into two free triplets. The dissociation of the quintet state into free triplets was also investigated by Lubert-Perquel *et al,* who applied angular-resolved tr-ESR experiments on highly ordered pentacene film to elucidate the influence of intermolecular geometries.[61] This allowed the authors to identify the parallel packing motif within the herringbone crystal structure as beneficial for the generation of free triplet states. In contrast, the edge-on motif resulted in the eventual recombination of the triplet pair. Furthermore, a very recent study revealed the importance of terahertz motions on the dissociation of the correlated triplet pair, highlighting the importance of vibrational motions on the SF process.[63]

### 2.1.3 Vibrational Dynamics

Descriptions of the electronic structure of $^1(TT)$ typically apply the Born-Oppenheimer approximation, *i.e.*, nuclear motions are neglected. However, recent reports emphasise the effect of vibrational dynamics on SF. While it has become consensus that they can play a crucial role in the coherent formation of the triplet pair, the respective explanations are varying. In order to understand implications of commonly employed experimental techniques, the fundamentals of vibrational coherence spectroscopy (VCS) will be discussed briefly. A comprehensive description of VCS techniques and the underlying principles can be found in the literature.[64] Furthermore, as VCS shares several aspects with transient absorption (TA)

spectroscopy, the reader is referred to section 3.2.2. One technique applied in VCS is impulsive vibrational spectroscopy (IVS). Here, the sample is initially excited by an ultrashort (≈10 fs) laser pulse, which possesses a broad spectrum due to the Heisenberg uncertainty principle. Thus, several vibrational sub-levels of the excited states can be populated simultaneously. This introduces a coherent superposition of vibrational quantum states, in short vibrational coherence, both in the ground and excited state (Figure 2.5). The vibrational coherence is subsequently interrogated by a spectrally broad probe pulse after a set time delay $\tau$ and results in periodic oscillations within the transient absorption kinetics, with their frequencies corresponding to Raman modes of the respective electronic state. From this measurement, dephasing times, modulations of the amplitudes or frequency shifts can be extracted, which complement population dynamics. However, the simultaneous presence of modes originating from ground and excited state often hinders a straightforward assignment of vibrational modes to electronic states, prompting the need for more complex experiments. One example to extract the pure contributions of the excited state vibrations is pump-IVS. Here, a third pulse is introduced with its wavelength being tuned to be resonant solely to an absorption feature of the excited state. In consequence, the excited state population is depleted and its contribution to the vibrational coherence is removed. Thus, the differences observed between IVS and pump-IVS measurements directly relates to vibrations originating from the excited state.

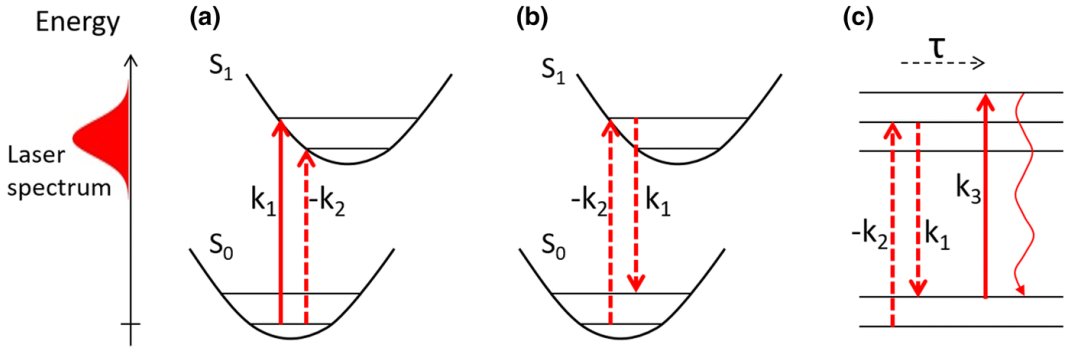


***Figure 2.5:*** *Basic principle of vibrational coherence spectroscopy (VCS). Upon excitation with an ultrashort laser pulse, vibrational sub-levels in (a) ground and (b) excited state are populated impulsively. c) After a set time delay* ***τ****, this vibrational coherence is probed by a third pulse. Reprinted with permission from ref. 64. Copyright © 2018, Springer Nature Switzerland AG.*

This method has been employed in an early study of Musser *et al.*, in which the authors report vibrational coherences in $^1(TT)$ in a triisopropylsilyl-ethynyl substituted pentacene (TIPS-Pn) thin film.[65] Given the unlikeliness of a spontaneously generated coherence in the correlated triplet pair, they conclude that the vibrational coherence has to originate from $S_1$ and is passed on *via* a conical intersection. In addition, the authors identified particular modes driving the excited state population to the conical intersection. (Figure 2.6). This concept was later expanded on with the identification of different types of vibrational modes first allowing for achieving the suitable inter-chromophore geometry ("tuning mode") followed by another mode driving SF itself ("coupling mode").[66-67] In addition, vibrational modes have been reported to increase the electronic coupling between $S_1S_0$ and $^1(TT)$.[44, 68-69] This is based on the additional vibrational energy compensating the energy mismatch between the excited singlet and triplet pair, leading to an increased density of states and consequently transition probability. Furthermore, molecular vibrations may alter the inter-chromophore geometry. The possible implications have been shown by Miyata *et al.*, who demonstrated a coherent formation of $^1(TT)$ in rubrene despite a vanishing coupling value at relaxed geometry (Figure 2.7).[46]

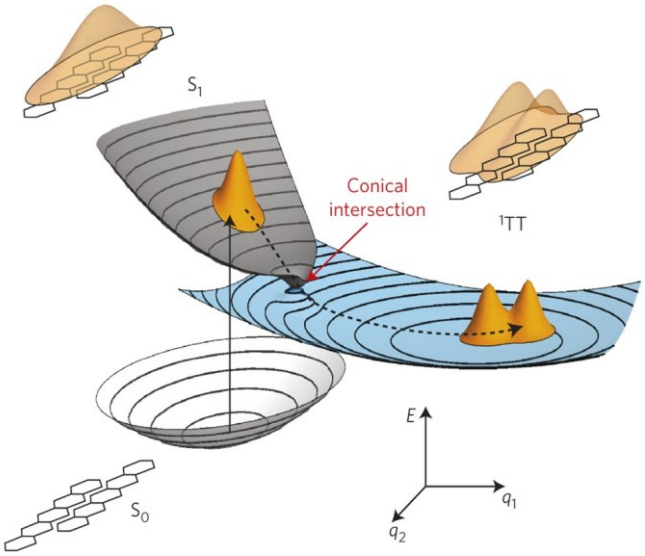


***Figure 2.6:*** *The excitation of a triisopropylsilyl-ethynyl substituted pentacene (TIPS-Pn) thin film by an ultrashort laser pulse generates a vibrational coherence in* $\boldsymbol{S_1}$*, which is passed on to* $^1(\boldsymbol{TT})$ *via a conical intersection. Reprinted with permission from ref. 65. Copyright © 2015, Nature Publishing Group.*

This was attributed to an antisymmetric torsional mode of the tetracene backbone breaking the inter-chromophore symmetry.

A commonality of the aforementioned studies is their usage of acenes and their derivatives. Thus, it is not known whether vibronic coupling is specific to this class of molecules or a common element of SF. This will be addressed in the discussion on vibrational dynamics in TAPPs (section 4.2), which provides new insights on the generality of vibronic coupling with regard to SF.

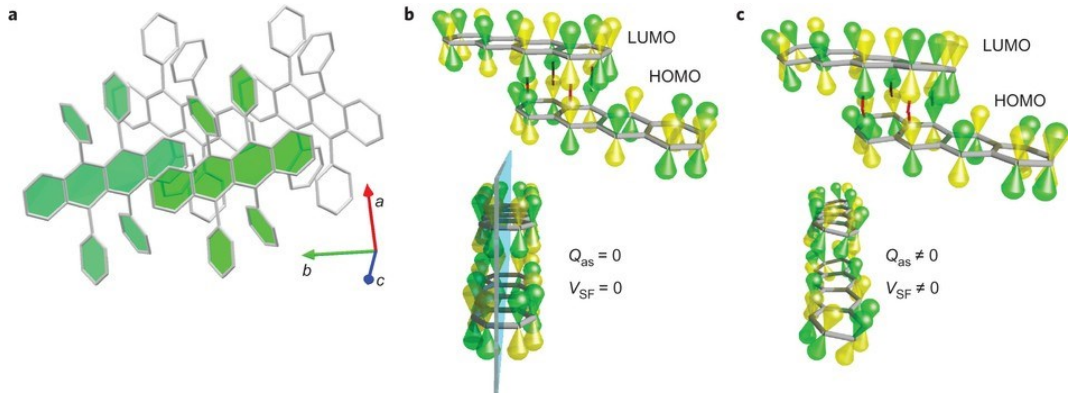


***Figure 2.7:*** *a) In rubrene crystals, the aromatic systems of the individual chromophores are shifted along the long axis of the molecule. b) Due to the molecular symmetry, this results in a vanishing coupling value between the excited singlet and* $^1(\boldsymbol{TT})$*. However, antisymmetric torsional modes within the tetracene backbone break the symmetry, resulting in non-zero coupling values. Reprinted with permission from ref. 46. Copyright © 2017, Nature Publishing Group.*

## 2.1.4 Diffusion-Controlled Singlet Fission

As depicted in Figure 2.1, SF is not a unidirectional process but contains several reversible sub-steps. In addition, even if chromophores exhibit high triplet yields, they can be diminished considerably by TTA. Both issues are mitigated in solution-based SF. Here, generated triplet chromophores start to diffuse apart immediately after SF, lessening the reversibility of SF. In addition, the weak binding energy of $^1(TT)$ (≈10 meV, *vide supra*) can be overcome by collisions between chromophore and solvent molecules. Due to diffusion being significant slower than SF itself, the former becomes the rate-determining step. Nonetheless, it has been shown that the reaction rates in concentrated solutions result in diffusion-controlled SF with triplet yields up to 200%.[26] In addition, the group of Friend suggested the presence of an excimer

intermediate based on the occurrence of a red-shifted emission in concentrated solutions.[25-26] This was, however, disputed by Dover *et al.*, who assigned the excimer to a trap state (Figure 2.8).[70] In general, only few studies exist on diffusion-controlled SF in solution, which focus on molecules based on tetracene or pentacene.[25-27, 71] Thus, in order to work towards a general mechanism for SF in solution, especially with regard to the disputed presence of an excimer intermediate, concentration dependent dynamics of a tetrachlorinated phenazinothiadiazole in solution will be investigated (section 5.2).

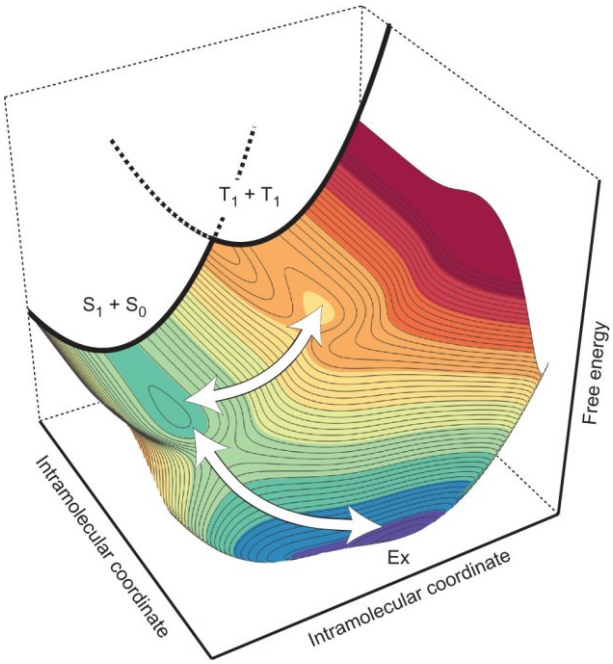


***Figure 2.8:*** *The schematic representation of the potential energy surface for SF in a tetracene derivative assigns the excimer observed in experiments to a trap state. Thus, it does not possess enough energy to dissociate into two separated triplet states. Reprinted with permission from ref. 70. Copyright © 2018, Nature Publishing Group.*

## 2.2 Materials for Singlet Fission

### 2.2.1 Diradical Character of Singlet Fission Chromophores

The viability of SF is influenced by a plenitude of molecular and environmental parameters as described in section 2.1. In consequence, predicting efficient SF is no trivial task. Nonetheless, the energy matching condition (Eq. 3) helps to screen possible candidates. However, while $S_1$ energy is readily accessible *via* optical spectroscopy, determining the energy of $T_1$ is more challenging due to it being a dark state. In consequence, $\Delta E_{SF}$ is often quantified by open-shell quantum chemical calculations of the participating energy levels. In an effort to establish a clear relationship between chemical concepts and energy levels, Nakano and co-workers pioneered the diradical character approach. In several reports since 2011, he and co-workers established a connection between the diradical character of a chromophore and its $T_1$ energy.[38, 72-79] Within the spin-projected, unrestricted Hartree-Fock method, the multiradical character $y_i$ is defined as the occupation number of the $i^{\text{th}}$ unoccupied natural orbital (LUNO), given by

$$y_i = 1 - 2\frac{N_i}{1 + N_i^2} \qquad \text{Eq. 4}$$

with $N_i$ referring to the orbital overlap of the highest occupied natural orbital (HONO) and the respective LUNO+$i$.[72] Most important for SF are the di- and tetraradical character, denoted as $y_0$ and $y_1$, respectively, which correlate with the energies of the first and second triplet state. This has been modelled initially for a symmetric, linear $H_4$ molecule with varying interatomic distances.[72] The advantage of choosing this simple system is that the application of the full configuration interaction method is feasible, which yields exact results for molecular properties. Based on this model, the feasibility of SF is assessed on the $y_0$-$y_1$ plane. The defining parameter is the energy efficiency $\eta$, which the authors defined as

$$\eta = \frac{2E(T_1) - E(S_1)}{E(S_1)} \qquad \text{Eq. 5}$$

This simple model correctly predicts SF in several known SF chromophores (Figure 2.9). Thus, a design strategy for molecules capable of SF was established: Chromophores should have an intermediate diradical character ($0.1 < y_0 < 0.4$), which enables SF without generating excess energy. In addition, a low tetraradical character is favourable to avoid TTA. The main benefit of this approach is that it provides a readily accessible tool to assess the $T_1$ energy by applying "typical" chemical concepts. For example, the stabilisation of a diradical can be visualized by resonance structures. As larger aromatic systems allow for a higher degree of delocalisation, the diradical character will increase accordingly. Furthermore, diradicaloid resonance structures may include the formation of extra Clar-sextets, resulting in additional stabilisation (Figure 2.10). In contrast, the influence of heteroatoms such as nitrogen does not allow for a straightforward prediction. On the one hand, nitrogen tends to stabilise radicals by hyperconjugation, while on the other hand its higher electronegativity compared to carbon reduces the overall aromaticity. Based on the diradical character view, a wide variety of potential chromophores was screened computationally.[38, 73-82] In an early study, larger polycyclic aromatic hydrocarbons (PAHs) such as oligorylenes were investigated.[74] Here, suitable conditions were predicted for terrylene, which was later proven experimentally.[83]

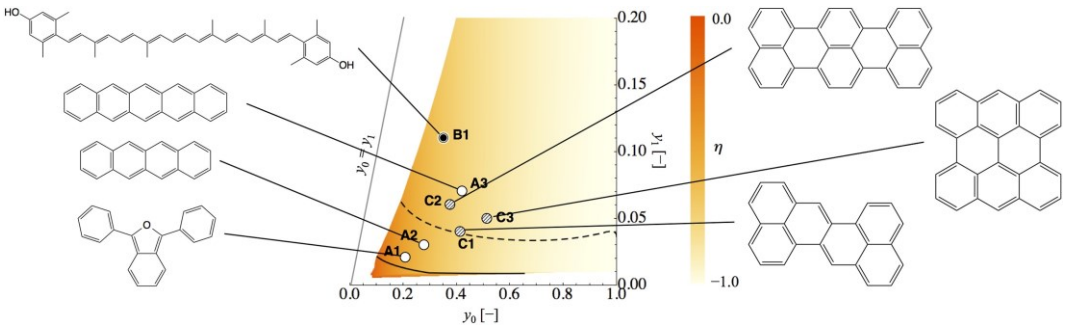


***Figure 2.9**: Energy efficiency η of SF with regard to the diradical ($y_0$) and tetraradical character ($y_1$), calculated based on a linear $H_4$ model on full CI level. Darker regions correspond to higher efficiencies, i.e., less excess energy. Labelled symbols represent calculated values for $y_0$ and $y_1$ for known SF chromophores (A1 (1,3-diphenylisobenzofuran), A2 (tetracene), A3 (pentacene), B1 (zeaxanthin), C1 (zethrene), C2 (terrylene), C3 (bisanthene)), calculated at the PUHF/6-31G* level of approximation. Respective molecular structures are indicated. Dashed and solid lines correspond to changes of the symmetry within $S_1$. Reprinted with permission from ref. 38. © 2018 Elsevier B.V.*

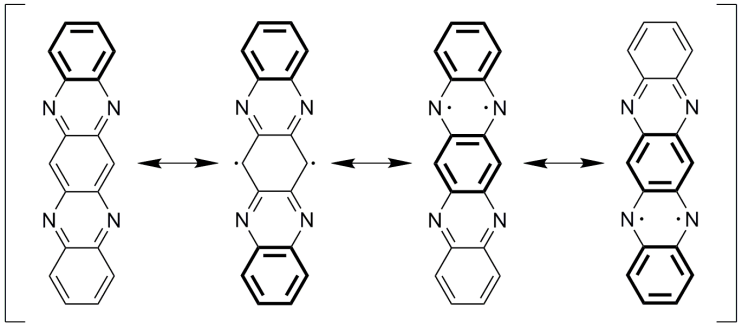

***Figure 2.10:*** *Selected resonance structures of tetraaza-pentacene. The formation of additional Clar-sextets (highlighted in bold) result in a stabilisation of the diradicaloid structures, decreasing the $T_1$ energy. Nitrogen substitution has two contrasting effects. On the one hand, the lone electron pair of nitrogen tends to stabilise radicals by hyperconjugation. On the other hand, the higher electronegativity results in a reduced aromaticity of the π-system.*

In addition, studies on the effect of the introduction of heteroatoms to the aromatic core were carried out. Chen *et al.* suggested that the substitution of an aromatic carbon by a $sp^2$-hybridised nitrogen slightly reduces $y_0$ due to a higher localisation of electron density at the nitrogen atoms,[84] which was corroborated by a later report of Ito *et al.*[76] In consequence, this approach was recommended to increase the energy efficiency in chromophores exhibiting exothermic SF such as pentacene. Indeed, Herz *et al.* has shown an acceleration of SF dynamics by a factor of two in aza-derivatives of pentacene, which may originate from a more suitable energy level alignment.[15] Furthermore, the $(\beta,\beta)$-connection of a thiophene moiety to a terminal benzene unit in anthracene and tetracene was predicted to significantly increase the $y_0$ (Figure 2.11).[84] The effect of introducing both sulphur and nitrogen to the aromatic core was investigated in a combined experimental and theoretical by a cooperation of Buckup and co-workers and the group of Prof. Dreuw (Universität Heidelberg).[21] As predicted, it was demonstrated that in tetracene, substituting a terminal benzene unit by a thiadiazole increases $y_0$, changing SF energetics from being endo- to exothermic. Moreover, further aza-substitution slightly decreases $y_0$, thus increasing the energy efficiency. Both approaches combined clearly show the ability to fine-tune SF by chemical modifications of the aromatic core. A further proposition to adjust $y_0$ in PAHs includes a twist of the aromatic plane.[78] This is achieved by the introduction of halide substituents, with the resulting in steric pressure deforming the aromatic system. Thus, the aromaticity decreases and diradical resonance structures become

unfavourable. Experimentally, the only report regarding SF in core-twisted chromophores covers bromine-substituted perylene-diimides (PDIs).[22] However, as this study focused on the long-time dynamics of triplets, no definitive conclusions for the effects of π-plane twisting on the early dynamics of SF can be drawn. Thus, further research is warranted in this regard, which could include structurally similar bay-substituted TAPPs.[85]

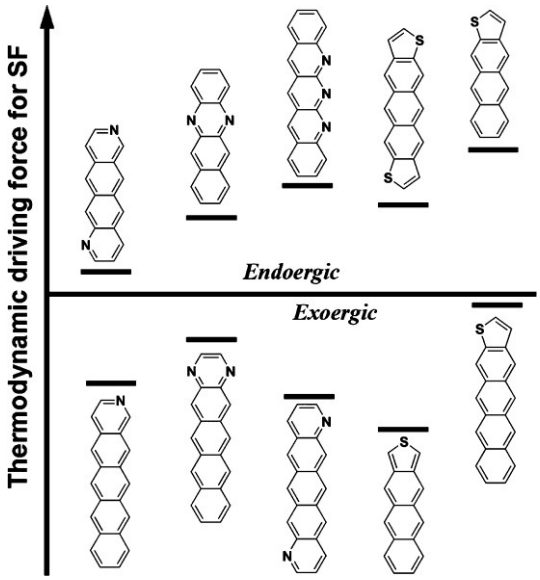


***Figure 2.11:*** *Heteroacene chromophores modelled by Chen et al. with regard to their feasibility for SF. The study clearly shows the influence of the incorporation of nitrogen and sulphur atoms to the aromatic core on the energetics of SF. Reprinted with permission from ref. 84. Copyright © 2014, American Chemical Society.*

## 2.2.2 Intermolecular Singlet Fission

### *2.2.2.1 Acenes*

SF has been demonstrated first in anthracene and tetracene.[30-31, 86] Taking the diradical model described in section 2.2.1 into account, this is not surprising as the acene motif allows for the stabilisation of diradical resonance structures (*cf.* Figure 2.10). In addition, acenes exhibit a systematic shift upon increasing the size of the aromatic system, notably including an increase of the singlet-triplet energy gap.[87-88] The implications of this can be clearly seen for SF in anthracene, tetracene, and pentacene (Figure 2.12). In the former case, SF only occurs out of higher sublevels within the first excited singlet state due to $\Delta E_{\mathrm{SF}} < 0$.[30] In tetracene, SF is only slightly

endothermic with $\Delta E_{SF} \approx 0$, leading to high efficiencies and SF time constants of 80-90 ps.[89-91] Finally, pentacene exhibits quantitative SF on the sub-ps timescale due to $\Delta E_{SF} > 0$.[18] In consequence, pentacene and its derivatives have become model systems for SF.[15-18, 26, 29, 37, 54, 62, 92-104] However, the application of pentacene itself is impeded by its low solubility as well as its photochemical instability in the presence of oxygen (Figure 2.13a).[105] Both issues are addressed by introducing triisopropylsilyl-ethynyl (TIPS-ethynyl) sidechains: The sterically demanding TIPS group reduces π–π-interactions in solid state and consequently improves solubility. The additional stabilisation of the lowest occupied molecular orbital (LUMO) further results in an excellent photostability in solution (Figure 2.13b).[106] In combination with the relative energy of $S_1$ and $T_1$, this allows for the sensitisation of molecular oxygen, whose the implications will be discussed in section 5.1. The effects of other chemical modifications of acenes on SF have been explored both theoretically[84, 107-109] and experimentally.[15-16, 41, 45, 110-111] For example, the aza-substitution of aromatic CH group accelerates the SF dynamics by a factor of two, which has been attributed to an enhanced intermolecular coupling.[15-16] In addition, halogenation of the aromatic core has been suggested as a tool to achieve favourable morphologies by promoting solid-state order in the molecular crystal.[110] Both approaches combined were investigated by Alagna *et al.* in a tetrachloro-phenazinothiadiazole.[21] In this class of molecules, a terminal benzene unit of TIPS- substituted tetracene (TIPS-Tn) is formally substituted by a thiadiazole.

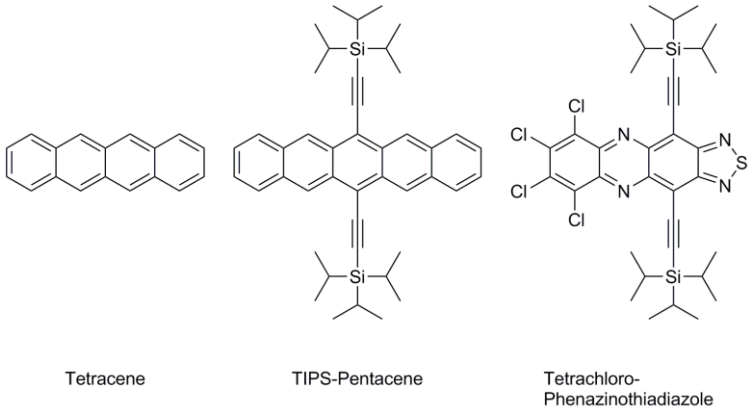


***Figure 2.12:*** *Molecular structures of acene-based chromophores investigated with regard to SF.*

In addition, two aromatic CH groups are replaced by a nitrogen. These substitutions lead to a decrease of the energy of $T_1$ compared to TIPS-Tn, resulting in more favourable SF energetics. In consequence, dynamics are accelerated from the pico- to femtosecond timescale and quantitative SF is achieved.[21] This study further unveiled the coupling between $S_1S_0$ and $^1(TT)$ to be the determining factor for SF and its sensitivity to inter-chromophore geometry. In addition, valuable insight into the availability of the triplets is gained: While a quantitative SF has been established, TTA effectively halves the number of triplets on the nanosecond timescale. This stresses the importance of finding an efficient way to separate the generated triplet pair.

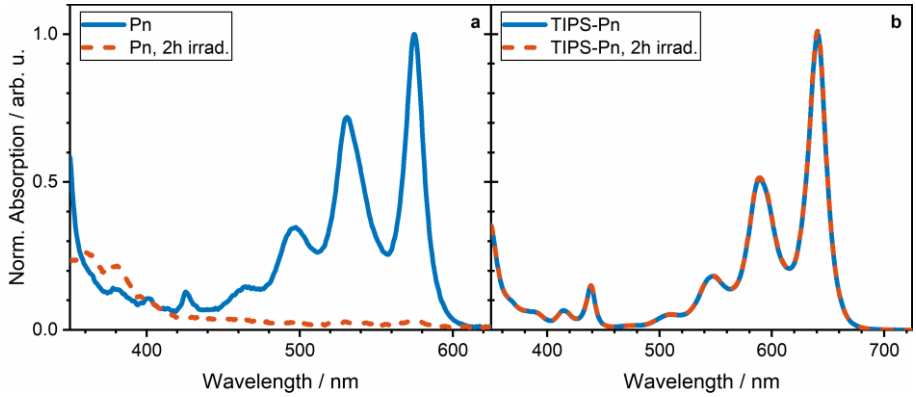


***Figure 2.13:*** *UV/Vis spectra of a) pentacene (Pn) and b) TIPS-Pentacene (TIPS-Pn) in THF before and after irradiation for 2 h. While the change in the spectrum of Pn points towards a photodegradation, TIPS-Pn exhibits an excellent photostability.*

### *2.2.2.2 Rylene-Based Molecules*

Besides the acene family, rylene-based chromophores have emerged as suitable SF candidates. Rylenes are best known in their use as industrial dyes due to their high extinction coefficients and photostability.[112] These optical properties, combined with their electron accepting ability, are also sought-after in the field of organic electronics, which led to rylenes becoming an actively researched group of molecules.[113-115] With regard to SF, especially PDIs (Figure 2.14) exhibit suitable properties including their favourable $S_1$ and $T_1$ energies as well as their slip-stacked packing motif.[19-20, 22, 43, 51-52, 116] Furthermore, the feasibility of SF in the chemically similar peropyrenes[23-24] as well as higher rylene homologues, *i.e.*, terrylenes,[51, 53, 83] has been assessed. The earliest report of SF in rylenes is from Albrecht *et al.*, who studied two different crystal

structures of perylene, *i.e.*, $\alpha$- and $\beta$-perylene.[19] This study elucidated the interplay between the excimer state and SF. In $\alpha$-perylene, the chromophores stack in a face-to-face arrangement, which benefits the formation of the excimer state. Here, the stabilisation experienced due to the delocalisation of the photoexcitation results in the excimer state being lower than $2E(T_1)$, thus hindering efficient SF. Nonetheless, SF was observed upon increasing the excitation energy, resulting in a more energy-rich excimer state proposed as SF precursor. In contrast, the edge-on geometry in $\beta$-perylene crystals hinders efficient excimer formation. Thus, SF was observed at significantly lower excitation energies. This early study reveals important information for the correlation between excimer formation and SF in perylenes: SF *may* occur out of an excimer state *if* its energy exceeds $E(2T_1)$. If this condition is not fulfilled, the excimer acts as a trap state, inhibiting SF. This has been supported by subsequent experimental observations, which indicate efficient SF for PDIs for which excimer formation is absent. Eaton *et al.* investigated a core-substituted PDI, which exhibits a triplet yield of 140%[116] This value is surpassed by *N*-substituted PDIs, for which Le *et al.* reported triplet yields up to 178%.[20, 52] Aulin *et al.* even reported quantitative SF for the same compound using a different approach to calculate the triplet yield.[43] This high efficiency is especially remarkable regarding the presence of a thermal barrier of ≈190 meV. It was proposed that the ability of the chromophores to overcome the activation barrier is based on superexchange coupling *via* a virtual CT state with the strength of the coupling strongly depending on inter-chromophore geometry.[51] Felter *et al.* investigated a set of excimer-forming PDIs with bromide substituents in the bay-positions.[22]

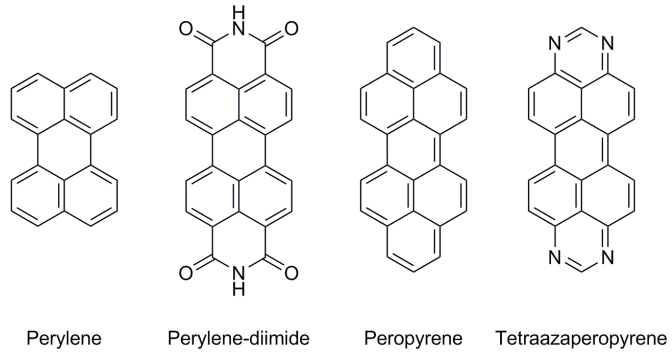


***Figure 2.14:*** *Molecular structures of rylene-based classes of chromophores investigated with regard to SF.*

This chemical modification results in a twist of the aromatic system due to the steric hinderance of the halide substituents (Figure 2.15). Upon decreasing the planarity of the aromatic system, a decrease in excimer formation is observed, which in turn increases SF efficiency. Thus, a direct competition between excimer formation and SF could be established. The promising results regarding SF in perylene and its derivatives also sparked interest in a similar class of molecules, peropyrenes, which can be viewed as a symmetrical extension of the aromatic system of perylene.[23-24] Here, no SF is observed despite $\Delta E_{SF} > 0$ in solution. This has been attributed to an efficient formation of an excimer trap state outcompeting SF. In the present work, TAPPs are suggested as a new class of chromophores (chapter 4). In total, four selected TAPP derivatives will be investigated, which contain a perfluorated alkyl sidechain to enhance solubility. In addition, halide substituents are introduced which have shown to systematically tune the physical properties of the chromophores.[117]

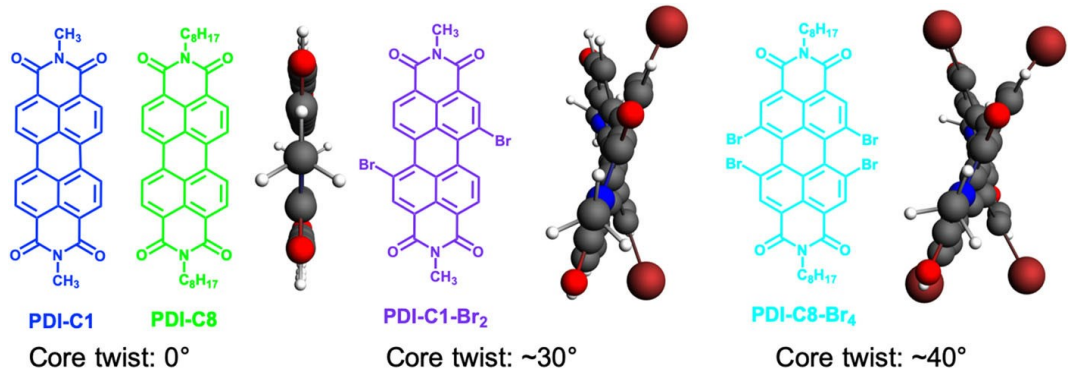


***Figure 2.15:*** *Upon bay-substitution, PDIs exhibit a twist of the aromatic system due to the steric hindrance introduced by the halide substituents. This leads to a disfavoured excimer formation with regard to the unsubstituted, planar molecule and consequently higher SF yields. Reprinted with permission from ref. 22. Copyright © 2019, AIP Publishing.*

## 2.2.3 Intramolecular Singlet Fission

A major drawback of intermolecular SF in solid state is the lack of tuneability, given that chromophores crystallise in well-defined intermolecular geometries. However, the versatility of chemical synthesis allows known SF chromophores to be connected by specifically designed linker moieties. These targeted modifications of either the chromophores themselves or the linker enable gradual variations of molecular

properties. In consequence, iSF presents a great tool to unveil the influence of *e.g.* electronic coupling or inter-chromophore geometry while keeping other parameters constant.

The first group of molecules for which iSF was reported are phenylene-linked tetracene dimers.[118-119] Here, connecting the tetracene moieties at the *para* position of the linker resulted in weak (≈3%) SF, which was completely absent in the *meta*-derivatives. This study reveals an important feature of iSF. Due to the spatial separation, the π-systems of the individual tetracene subunits cannot overlap. Consequently, the electronic coupling of the chromophores has to occur *via* conjugation including the linker itself. This rationalises the absence of iSF for the *meta*-derivative, in which the tetracene moieties are cross-conjugated. The simple phenylene-linker, however, does not allow to synthesise the *ortho*-isomer, as the steric hinderance between the chromophores becomes too high. This problem can be addressed by introducing an additional ethynyl-bridge between the central phenylene and the chromophores. This connection pattern has been investigated by Buckup and co-workers with tetraaza-pentacene moieties used as active SF chromophores.[29] In this study, the *ortho* and *meta* regioisomers (o-TTPn and m-TTPn) as well as the point-symmetric trimer (t-TTPn) were investigated. While all three compounds exhibit iSF, the rate in o-TTPn is one order of magnitude faster compared to m-TTPn and t-TTPn. In turn, iSF dynamics in the latter are accelerated by one third compared to m-TTPn, which are attributed to an increased interaction probability given the doubled amount of available reaction partners. While a triplet yield of 160-180% was achieved for all compounds, TTA diminished the number of free triplet states on the nanosecond timescale (Figure 2.16). These results are corroborated by a study of Zirzlmeier *et al.*, who investigated identically linked pentacene dimers.[100] In addition, they identified the main coupling pathways to be π-stacking and linear conjugation for the *ortho* and *para* isomer, respectively. In turn, the comparatively low yields in the *meta* dimer were explained by a limited coupling due to the cross-conjugation of the individual chromophores. Both studies highlight the delicate balance required for efficient iSF: A strong electronic coupling between the two chromophores accelerates iSF while simultaneously benefitting TTA.

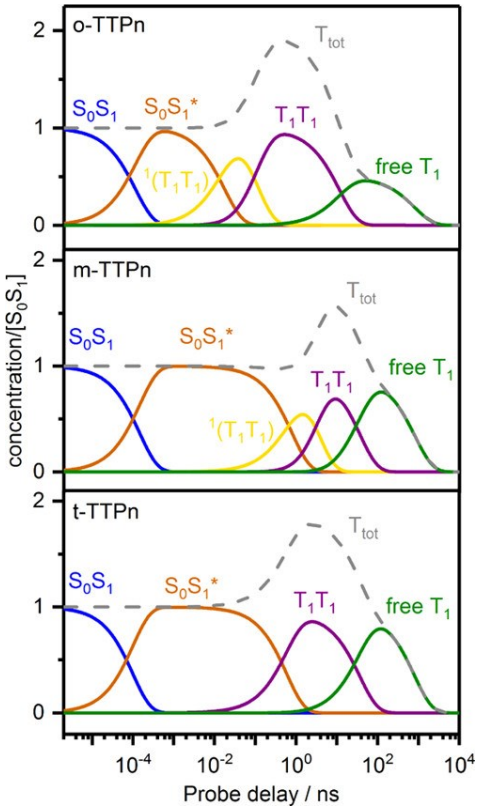


***Figure 2.16:*** *Population dynamics for ethynyl-phenylene linked tetraaza-pentacene (TTPn) oligomers. A high triplet yield (>160%) is observed in all three compounds. The respective rate is fastest in o-TTPn, followed by t-TTPn and m-TTPn. TTA diminishes the yield of free triplet states in all three oligomers on the nanosecond timescale. Reprinted with permission from ref. 29. Copyright © 2019, American Chemical Society.*

This is in line with the predictions derived from the modelled electronic structure of $^1(TT)$ (*cf.* section 2.1.2). Based on this knowledge, Basel *et al.* replaced the central phenylene by an adamantyl subunit.[62] Both linkers result in almost the same inter-chromophore geomtery (Figure 2.17). However, as the adamantyl-linked chromophores are not conjugated, the electronic coupling is reduced significantly. Despite this resulting in iSF dynamics being slowed down by up to two orders of magnitude compared to conjugated linkers, a high triplet yield (188%) was observed. In addition, the weaker coupling allowed for an efficient decoherence of the triplet pair. Another approach to tune the inter-chromophore electronic coupling was reported by Fuemmeler *et al.* in a series of directly linked pentacene derivatives.[68] By introducing varying substituents, the dihedral angle between the chromophores was gradually altered.


***Figure 2.17:*** *A comparison of the structure of a) an ethynyl-phenylene linker and b) an ethynyl-adamantyl linker shows that c) both result in an almost identical inter-chromophore geometry. However, the adamantyl subunit does not allows for a conjugation of the chromophores, significantly reducing the electronic coupling. Adapted with permission from ref. 120. Copyright © 2018 Wiley- VCH Verlag GmbH & Co. KGaA.*

This systematically decreased the iSF rate, in agreement with their predictions for a direct-coupling mechanism. Simultaneously, the triplet recombination rate decreased, reinforcing that both iSF and TTA depend on the strength of the electronic coupling. This is corroborated by a report of Sanders *et al.*, in which the electronic coupling between two pentacene chromophores is systematically varied by the length of the linker (Figure 2.18).[99] While all three compounds exhibit a quantitative formation of the triplet pair, its lifetime is extended drastically from 0.45 to 270 ns with increasing chromophore separation. Efficient SF in the face of a weak electronic coupling between $S_1$ and $^1(TT)$ was further reported by Busby *et al.*, who investigated iSF in donor-acceptor materials.[121] Here, high triplet yields up to 170% were reported, which were suggested to originate from a the involvement of a virtual CT state.

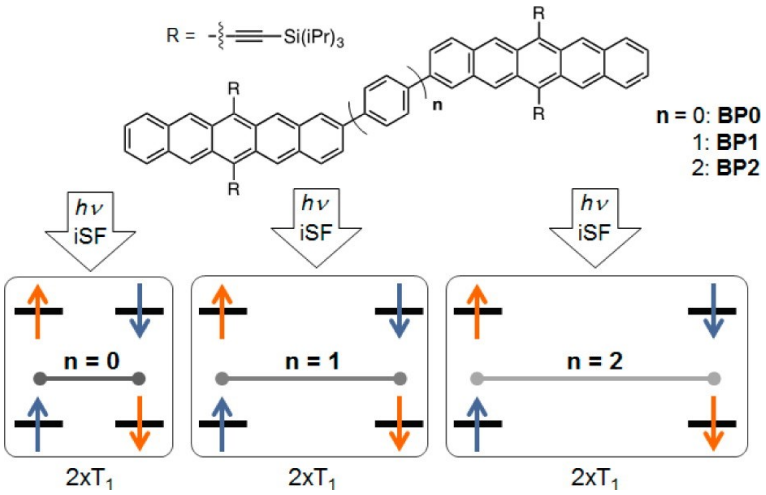


***Figure 2.18:*** *The variation of the length of the phenylene-based linker has strong implications for the recombination of the triplet pair. Regardless of linker size, a quantitative formation of the triplet pair is observed. In turn, its lifetime increases drastically from 0.45 to 270 ns upon increasing the distance between the pentacene moieties. Reprinted with permission from ref. 99. Copyright © 2015, American Chemical Society.*

The connection between CT states and SF has been the study of several reports over the last year. Given that iSF can be monitored in solution, a variation of the solvent presents an easy way to change the polarity and thus directly affect the energy of the CT state. This approach was applied in a study conducted by Zirzlmeier *et al*., who observed an increase of the triplet quantum yield in a phenylene-linked pentacene dimer from 126% to 145% with increasing solvent polarity.[100]Thus, they suggested that a mixing of the excited singlet state with the CT state allows for the activation barrier for iSF to be surpassed. However, the authors were not able to determine whether the CT state participates as a virtual or intermediate state. This was addressed in two consecutive studies of Lukman *et al*.[55, 122] Here, the authors investigated two covalently linked pentacene dimers with TIPS-ethynyl (DP-TIPS) and mesitylene (DP-Mes) side groups, respectively. Due to the steric hindrance of the chromophores, the chromophores adopt an almost orthogonal orientation and thus are expected to have a negligible electronic coupling. Nonetheless, iSF with high triplet yields (>120%) was demonstrated in both compounds. Intriguingly, DP-Mes exhibits a systematic decrease of the yield with increasing solvent polarity, while the opposite is observed for DP-TIPS. The authors attributed this effect to different iSF mechanisms for both compounds (Figure 2.19). Upon photoexcitation, DP-TIPS mainly populates a CT intermediate, whose energy can be tuned by varying solvent polarity. Consequently, more polar solvents favour the population of the CT state and thus the subsequent iSF. In turn, an increasingly polar environment favours the formation of the solvent-stabilised singlet $S_{\mathrm{stab}}$ in DP-Mes, whereas CT-mediated iSF becomes less prevalent. Thus, the authors concluded that seemingly slight chemical modifications can have strong implications for the iSF mechanism. A similar dependence of solvent polarity on iSF yields has been established for an adamantyl-linked pentacene dimer.[123] Here, a weak triplet pair formation (18%) was observed in the non-polar solvent cyclohexane, whereas a quantitative process occurs in benzonitrile. This reinforces the importance of CT mediations in molecules without strong electronic coupling. Intriguingly, Alagna *et al.* recently observed efficient iSF in a set of directly linked azaarene-dimers which possess an orthogonal orientation of the aromatic systems.[28]

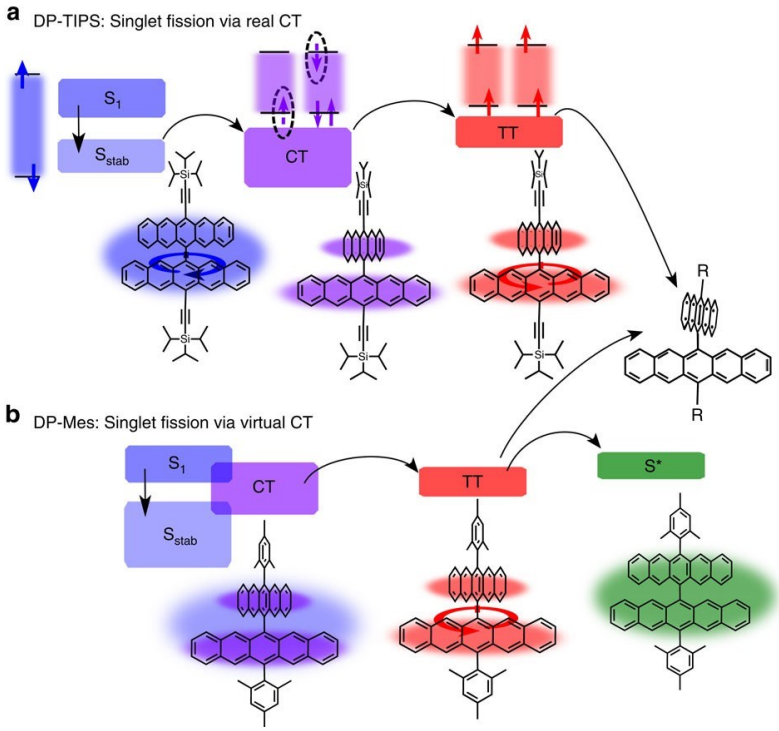


***Figure 2.19:*** *Comparison of the iSF mechanism in directly linked pentacene dimers with a) TIPS (DP-TIPS) and b) mesitylene substituents (DP-Mes). In DP-TIPS, a solvent-stabilised CT state is populated directly, which subsequently forms the correlated triplet pair. In turn, iSF in DP-Mes occurs via a virtual CT state. This allows for the formation of a solvent-stabilised excited singlet state to compete with iSF. Reprinted with permission from ref. 55 under the terms of the Creative Commons CC BY license.*

While this study focused on the effects of chemical modification on iSF, aforementioned reports imply that the high efficiencies for the formation of the triplet pair originate from a CT mediated process. Due to the commonly observed recombination of the triplet pair generated *via* iSF, avoiding TTA to allow for an efficient extraction of free triplets is crucial for eventual applications. To a certain degree, this problem is already addressed when moving from typical solution-based iSF studies to the solid state. Here, the presence of neighbouring molecules means that the correlated triplet pair is no longer confined to a single molecule. Instead, the intermolecular transfer of the constituent triplets aids the decorrelation process. This has been demonstrated by Korovina *et al.*, who investigated the *ortho* regioisomer of a tetracene dimer using an ethynyl-phenylene linker.[124] In this molecule, the tetracene moieties adopt an almost parallel orientation, which allows for a strong overlap of both π-systems. In consequence, an ultrafast (2 ps) and quantitative formation of $^1(TT)$ was observed in solution. However, due to the spatial confinement, the correlated

triplet pair in an isolated molecule exhibits a short lifetime of 500 ps. In contrast, an amorphous film of the dimer allows for an energy transfer to neighbouring molecules, which resulted in a triplet yield of 156%. For comparison, an identically prepared film of the monomer exhibits a triplet yield of only 90%. These results illustrate on the one hand the importance of intermolecular triplet transfer in order to efficiently separate the correlated triplet pair. On the other hand, the pre-orientation within the iSF compound itself clearly benefits the triplet yield even in disordered materials. Similar observations have been made in other studies.[125-127]

As a final part on iSF, three selected examples of recent advances in the design of chromophores and/or linkers are discussed. Antiaromats were proposed to be suitable SF candidates as early as 2012 due to their unique properties resulting in a high diradical character at a small size of the chromophore.[73] This assumption was proven correct in 2017, when Wu *et al*. demonstrated SF in a dibenzopentalene (Figure 2.20).[126] Given the small size of the system compared to other molecules exhibiting iSF, it is most remarkable that an efficient formation of the correlated triplet pair is observed. While a rapid triplet recombination is observed in solution, efficient triplet exciton diffusion results in a free triplet yield of 142%.

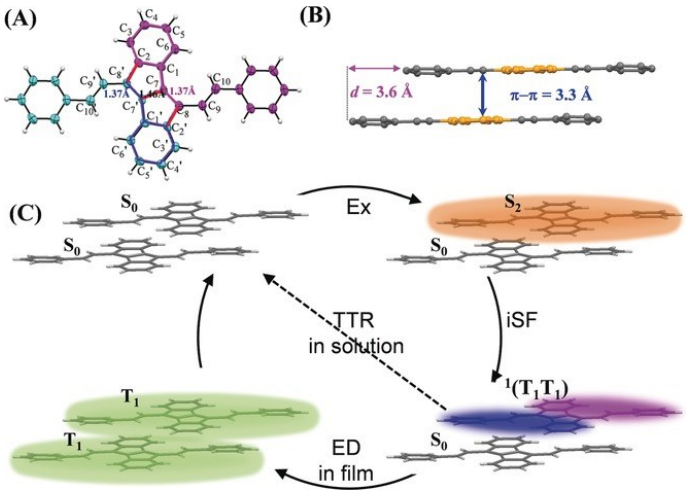


***Figure 2.20:*** *a) Within the structure of the antiaromatic dibenzopentalene, two separate conjugated structures can be separated, indicated by purple and blue colours. The short intermolecular distances (b) allow for an efficient triplet exciton diffusion in solid state (c), which allows for an efficient separation of the correlated triplet pair generated via iSF. Reprinted with permission from ref. 126. Copyright © 2017 Wiley- VCH Verlag GmbH & Co. KGaA.*

Korovina *et al.* investigated a series of bridged perylene oligomers, for which an endothermic energy balance is expected for iSF. Nonetheless, the formation of a separated triplet pair was observed for longer oligomers, which the authors attributed to the decoupling of the correlated triplet pair due to rotational diffusion along the axis of the linker.[127] Thus, this study invokes the separation of the correlated triplet pair in supramolecular structures *via* dynamic conformational changes. Finally, Yamakado *et al.* investigated a set of acene dimers linked by a cyclooctatetraene (COT) moiety (Figure 2.21).[128] For tetracene and pentacene as active chromophores, fast (<5 ps) and efficient iSF was reported with reported triplet pair yields of 180% and 200%, respectively. The exact mechanism is interesting due to the conformational flexibility of the COT linker. While higher acene substituents favour the bent geometry in both ground and excited singlet state, planarization was observed for naphthalene and anthracene.

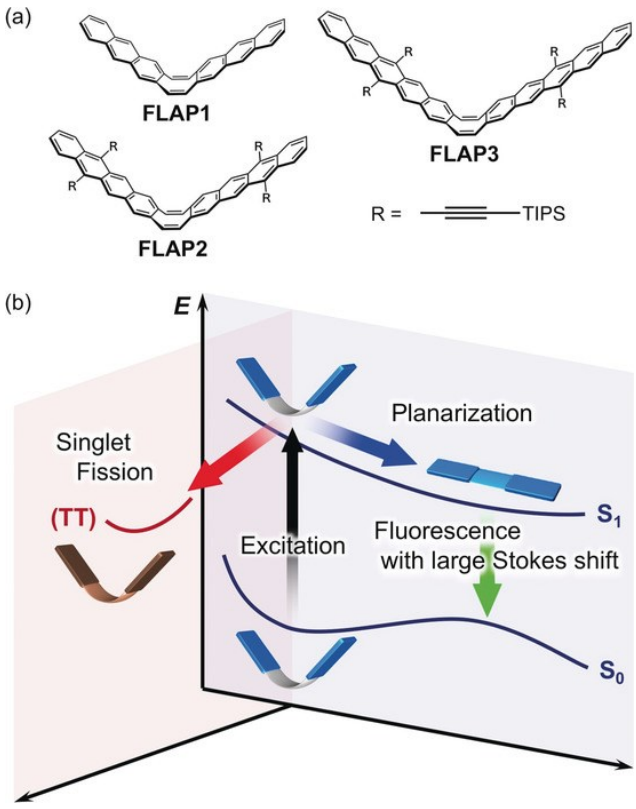


***Figure 2.21:*** *a) Acene-based dimers connected via a cyclooctatetraene moiety exhibit a bent ground state geometry. b) Upon photoexcitation, planarization is dominant for naphthalene and anthracene chromophores, while efficient SF is observed for higher acene homologues, i.e., tetracene and pentacene. Reprinted with permission from ref. 128. Copyright © 2018 Wiley- VCH Verlag GmbH & Co. KGaA.*

Thus, given the known influence of external stimuli such as mechanical force or hydrostatic pressure on COT conformations, the authors suggested that iSF dynamics may be selectively switched on or off by those factors.

### *2.2.3.1 Singlet Fission in Polymers*

SF in polymers can be viewed as a special case of iSF. While several reports on iSF in polymers exist, the discussion will be limited to new insights on the iSF process.[6, 32, 129-136] Pace *et al.* studied the influence of local microstructures on the decorrelation of the triplet pair in poly(benzothiophene dioxide).[130] While in solution, individual chains exhibited a free triplet yield of 4%, this value was increased by a factor of six in thin films. The authors attributed this effect to the presence of different intra- and interchain microstructures. While intrachain excitations result in a rapid recombination of $^1(TT)$, suitable interchain reaction sites allow for its efficient decorrelation (Figure 2.22). Another approach to efficiently separate $^1(TT)$ was presented by Musser *et al.*, who assessed the heavy-atom effect on iSF dynamics.[131]

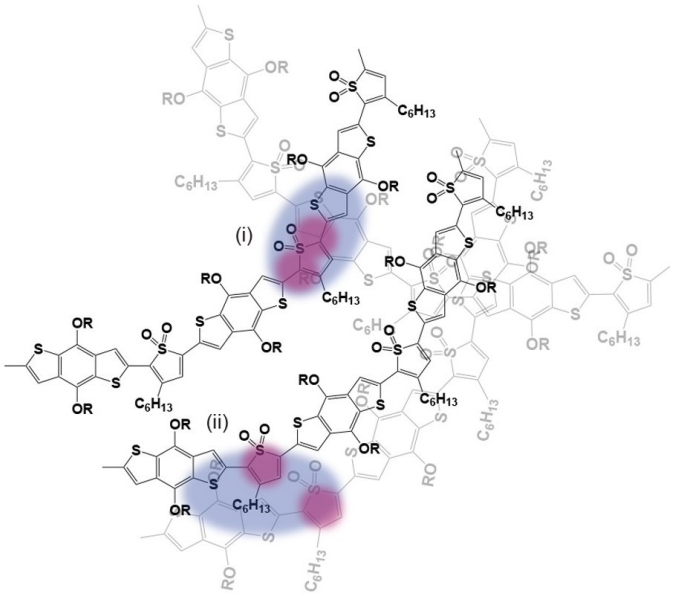


***Figure 2.22:*** *Schematic representation of microstructures in poly(benzothiophene dioxide) leading to different iSF dynamics. Blue highlighted regions denote a delocalised singlet excitation, while purple areas represent triplet excitons. Upon intrachain excitations (i), a correlated triplet pair is generated which rapidly recombines. In contrast, interchain excitations (ii) allow for the formation of free triplet states. Adapted with permission from ref. 132. Copyright © 2017, American Chemical Society.*

Three conjugated polymers were investigated, which contained thiophene, selenophene and tellurophene subunits, respectively. The authors demonstrated that the formation of the triplet pair is basically unaffected by the heteroatom. In turn, it was shown that the heavier selenium and tellurium atoms allowed for a faster decorrelation of the triplet pair, which was assigned to enhanced spin-orbit coupling. Thus, heavy-atom substitution was suggested as an additional concept allowing for the efficient generation of free triplet states. Finally, Pun *et al*. reported the successful triplet energy transfer of polytetracene to various acceptor molecules.[129] Notably, this constitutes the first example for a successful extraction of free triplet states generated by iSF.

# 3 Experimental Methods

## 3.1 Sample Preparation

The tetrachloro-phenazinothiadiazole ($TDCl_4$, Figure 2.12) as well as the TAPP derivatives (TAPP-H, TAPP-Cl, TAPP-Br, and TAPP-I, Figure 4.1) were synthesised by the groups of Prof. Bunz and Prof. Gade (both Universität Heidelberg), respectively, following procedures described in the literature.[137-140] TIPS-Pn was purchased from Sigma-Aldrich (≥99%) and used without further purification. Depending on the experiment, the compounds were dissolved either in acetonitrile (Sigma-Aldrich, ≥99.8%), tetrahydrofuran (THF, Sigma-Aldrich, inhibitor-free, ≥99.9%) or toluene (Sigma-Aldrich, ≥99.9%). Stationary optical spectra were measured in fused silica cuvettes with a pathlength of 10 µm (Starna, Type 48/Q) for concentrations $c > 2$ mM and 2 mm (Hellma) for $c \leq 2$ mM. The respective cuvettes were used for all subsequent experiments.

UV-VIS spectra were measured in a UV-2600 absorption spectrometer (Shimadzu). For $TDCl_4$ in toluene, a molar extinction coefficient of $\varepsilon_{670} = 16773\ M^{-1}\ cm^{-1}$ at 670 nm was determined using a sample with a well-defined concentration of $30\ mg\ ml^{-1}$. The extinction coefficient was used to obtain the exact molar concentration of all other samples. The concentrations of TAPP-H, TAPP-Cl, TAPP-Br, and TAPP-I in acetonitrile were determined to be 13.7, 9.5, 6.9 and 5.8 µM, respectively, using the extinction coefficients reported previously.[117] In addition, stationary absorption spectra were measured before and after light irradiation to assess the photo-stability of the samples. No indications of photodegradation were observed. Deaerated solutions were prepared using a freeze-pump-thaw method in a home-built setup. Initially, the sample was frozen using liquid nitrogen. Subsequently, a turbomolecular pump was used to evacuate the flask until a constant pressure was observed. At this point, the sample was vented with dry $N_2$. The cycle was repeated three to five times until a pressure below $5 \times 10^{-5}$ mbar was achieved. The TAPP-Cl and TAPP-Br thin film samples were prepared by Vaishnavi Rao (Prof. Zaumseil, Universität Heidelberg) on pre-cut glass substrates with a thickness of 0.5 mm. On top

of the substrate, a 50 nm thick layer of cross-linked benzocyclobutene (BCB, Dow CYCLOTENE 3022-35) was used to create a homogeneous surface. This was achieved by diluting a BCB precursor with mesitylene in a volumetric ratio of 1:6. The solution was deposited *via* spin-coating (500 rpm for 3 s followed by 8000 rpm for 60 s) and cross-linked for 60 s at 290°C in a nitrogen glovebox. Solutions of TAPP-Cl and TAPP-Br were prepared by dissolving the respective compound in o-xylene (Sigma-Aldrich, anhydrous, 97%) with a concentration of 5 mg/ml. To avoid aggregation, the solutions were sonicated for 5 min and heated at 110°C for 15 min. The thin films were prepared *via* zone-casting.[141] Here, the glass/BCB substrates were heated to 130°C and films with ribbon-like features were obtained. UV/Vis spectra of thin films were measured using a Cary 6000i absorption spectrometer (Agilent).

## 3.2 Experimental Details

### 3.2.1 Emission Measurements

Stationary emission measurements in dilute solution (<0.1 mM) were carried out in a JASCO FP 8200 spectrofluorometer using a 1 cm quartz cuvette. Samples were excited at their most red-shifted absorption feature. For concentrated solutions, a LifeSpec II lifetime spectrometer from Edinburgh Instruments was used. Here, a right-angle geometry was adopted in order to minimise inner filter effects. For this, cuvettes were placed at 45° regarding the incident excitation beam and the collection optics. Three separate diode lasers (Edinburgh Instruments) with wavelengths of 375 (EPL-375), 475 (EPL-475), and 635 nm (EPL-635), pulse durations of 100 ps, and selectable repetition rates (20 kHz to 20 MHz) were available as excitation. Hereof, the most suitable source regarding the absorption spectrum of the respective chromophore was selected. Obtained emission spectra were corrected for instrumental factors with the correction function supplied by the manufacturer and converted to cross-section for stimulated emission ($\sigma_{SE}$) by multiplication with $\lambda^4$.[142]

Emission lifetime measurements of dissolved chromophores were carried out within the same LifeSpec II setup *via* time-correlated single photon counting (TCSPC). The repetition rate was set under consideration of the time scale of the emission decay (<100 ns) and typically amounted to 5 MHz. Furthermore, in order to avoid a pile-up effect, the intensity of the excitation beam was adjusted so that the stop rate amounted to ≈0.2% of the repetition rate. The instrument response was obtained by inserting a dispersive element into the beam path.

Emission spectra and decay of thin films were obtained with the collaboration of Felix Berger using a home-built setup in the group of Prof. Zaumseil (Universität Heidelberg). Using the spectrally filtered output of a pulsed supercontinuum laser source (Fianium WhiteLase SC400, 20 MHz repetition rate, ≈10 ps pulse width), the samples were excited at 450 nm. A 20× objective was used to focus the excitation beam and to collect the photoluminescence. In order to spectrally resolve the emitted

light, it was dispersed by an Acton SpectraPro SP2358 spectrograph (grating 150 lines $mm^{-1}$) and detected by a liquid nitrogen cooled InGaAs line camera (Princeton Instruments OMA V). Scattered light of the excitation beam was blocked by a longpass filter (495 nm cut-on wavelength). Time-resolved emission measurements were realised by focusing the output of the spectrograph onto a silicon avalanche photodiode (Micro Photon Devices). Respective decay traces were obtained using PicoHarp 300 (PicoQuant) single photon counting electronics.

### 3.2.2 Transient Absorption

Fundamental femtosecond pulses were obtained from a regenerative Ti:Sa amplified laser system (Coherent Astrella). The generated pulses possess a temporal width of 70 fs (FWHM) and an energy of 1.5 mJ at a repetition rate of 4 kHz. Hereof, 0.65 mJ were routed to an optical parametric amplifier (TOPAS Prime, Light Conversion), which was used to generate the femtosecond pump pulses. The pulses typically do not exhibit a significant temporal broadening, as exemplified for a wavelength of 422 nm (Figure 3.1). TA measurements were carried out using two commercially available setups located within the same housing, which allows for a shared optical pathway. For probe delays up to 8 ns ("short-time" setup), a HELIOS Fire setup from Ultrafast Systems was used (Figure 3.2a).

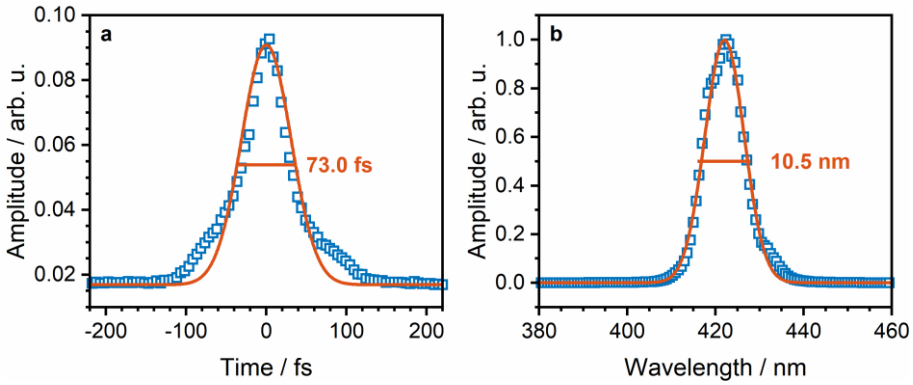


***Figure 3.1:*** *a) Autocorrelation trace and b) spectrum of a pump pulse with a centre wavelength of 422 nm (blue squares). The respective Gaussian fits (orange lines) show a FWHM of 73.0 fs in the temporal and 10.5 nm in the spectral domain.*

"Long-time" measurements up to 400 µs were carried out using an EOS Fire setup (Ultrafast Systems, Figure 3.2b). For both setups, the pump pulses initially pass through a chopper before being routed to a concave mirror, which focuses the beam onto the sample cell with an approximate spot size of 0.3 mm. In contrast, generation and delay of probe pulses differ between both setups. In order to generate the probe delay in the short-time setup, a part of the fundamental beam (≈0.1 mJ) is routed through a mechanical delay stage. Using this method, a minimal time step of 13 fs is achieved. Subsequently, the fundamental beam is focused onto a sapphire substrate. Due to self-modulation, a linearly polarized continuum is generated which covers a spectral window ranging from 440 to 760 nm. After collimation, the probe beam is focused onto the sample cell using parabolic mirrors. An average pump-probe cross-correlation with an FWHM of ≤100 fs across the full spectral window is achieved (*cf.* section 3.3.2). For solution measurements, the relative polarisation of pump and probe beams was set to 54.7° ("magic angle") in order to account for molecular reorientation dynamics.[143] Thin film measurements were carried out with a parallel relative polarisation.

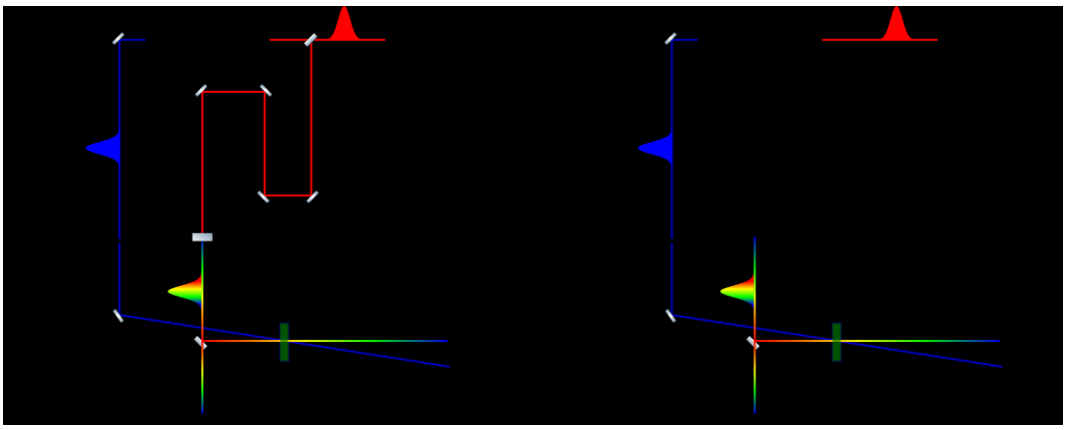

***Figure 3.2:*** *Schematic representation of the experimental setup for a) short and b) long-time TA measurements. Both setups share the pathway for the pump pulse but differ in white light generation and realisation of probe delay. In the short-time setup, the fundamental beam is routed through a mechanical delay stage, allowing for time steps of up to 13 fs. Subsequently, a supercontinuum is generated by focusing the beam onto a sapphire substrate, resulting in a spectral window ranging from 440 to 760 nm. An instrument response of ≈100 fs is achieved over the whole spectral range. The long-time setup utilises a supercontinuum laser with a spectral window from 350 to 900 nm and an electronically generated pump-probe delay. The instrument response of ≈350 ps is mainly determined by the pulse duration of the supercontinuum laser.*

In the long-time setup, the probe pulse is generated by a supercontinuum laser with a spectral window from 350 to 900 nm and a repetition rate of 2 kHz. The pump-probe delay was achieved electronically. Due to the timing jitter between pump and probe pulse as well as the pulse duration of the supercontinuum laser, the instrument response amounts to ≈350 ps.

## 3.3 Data Processing and Analysis for Transient Absorption Measurements

In TA, a small fraction of chromophores is excited at a specific wavelength by an ultrashort (<100 fs) *pump* pulse. Subsequently, the absorption of the excited sample is interrogated by a spectrally broad *probe* pulse arriving with a defined time-shift $\tau$ (*probe delay*) regarding the pump pulse. By comparing the obtained spectrum with the ground state absorption, a difference spectrum $\Delta A(\lambda, \tau)$ is obtained which consists purely of contributions of the excited sample. According to Lambert-Beers law, the difference spectrum is calculated as

$$\Delta\mathrm{A}(\lambda, \tau) = -\log\left(\frac{I(\lambda, \tau)_{\mathrm{on}}}{I(\lambda, \tau)_{\mathrm{off}}}\right) \qquad \text{Eq. 6}$$

Here, $I(\lambda, \tau)_{\mathrm{on}}$ and $I(\lambda, \tau)_{\mathrm{off}}$ represent the wavelength dependent intensity of the probe pulse with and without excitation, respectively. Experimentally, $\Delta A$ is obtained by introducing a chopper in the beam path of the pump, which blocks every second pulse. By varying the probe delay, snapshots of the excited state spectrum at the given probe delay, called *transient spectra*, are obtained. Akin to *e.g.* cameras, a high density of snapshots in a given time window allows for a continuous depiction of occurring processes. The spectral features themselves can be separated into two groups, *i.e.*, sequential and coherent contributions, also called *coherent artefact* (CA). The former constitutes the molecular response, which describes the interaction of the probe pulse with the photoexcited chromophore. In turn, coherent contributions are observed even in transparent media, *e.g.* the solvent or glass substrate. They originate from nonlinear interactions between pump and probe pulse around time-zero, *i.e.*, the temporal overlap of both pulses. The effects of sequential and coherent contributions on the TA signal will be discussed in the following section.

### 3.3.1 Sequential and Coherent Contributions to the TA Signal

*Sequential Contributions.*

In a photostable chromophore, three distinct sequential contributions to the transient spectrum can be discerned. First, the chromophore population in the excited state reduces the number of chromophores in the ground state. Thus, a higher fraction of the initial probe intensity arrives at the detector. This manifests itself in the transient spectrum as a negative *ground state bleach* (GSB), mirroring the spectral profile of the ground-state absorption (Figure 3.3). Second, the probe pulse may induce the emission of a photon by *stimulated emission* (SE). Thus, the number of incoming photons reaching the detector is increased. Consequently, a negative signal is observed in the transient spectrum. Due to SE and GSB having the same Einstein coefficients, the transition probabilities are identical.[144] The final contribution to the transient spectrum is excited state absorption (ESA). Here, the excited chromophore absorbs a photon and is subsequently promoted to an even higher excited state. As this results in a reduced number of photons reaching the detector, ESA corresponds to a positive signal. This allows for TA to monitor states which are optically inaccessible from the ground state ("dark" states). This is exemplified by triplet states, whose optical excitation constitutes a spin-forbidden transition. However, the initial photoexcited state can undergo a photophysical process, *e.g.* ISC or SF, generating a triplet. This emerging species can be probed in the same way as a singlet state, *i.e.*, promoting the chromophore to a higher level within the triplet manifold. Here, the spin is conserved, and the transition is optically allowed, resulting in a characteristic ESA signal.

*Coherent Contributions.*

While sequential contributions require the excitation of a chromophore, coherent contributions are observed even in a transparent medium. In order to explain this phenomenon, three nonlinear effects have to be considered, which are two-photon absorption (TPA), stimulated Raman amplification (SRA) and cross-phase modulation (CPM).[145-146] TPA describes the simultaneous absorption of a pump and probe photon.

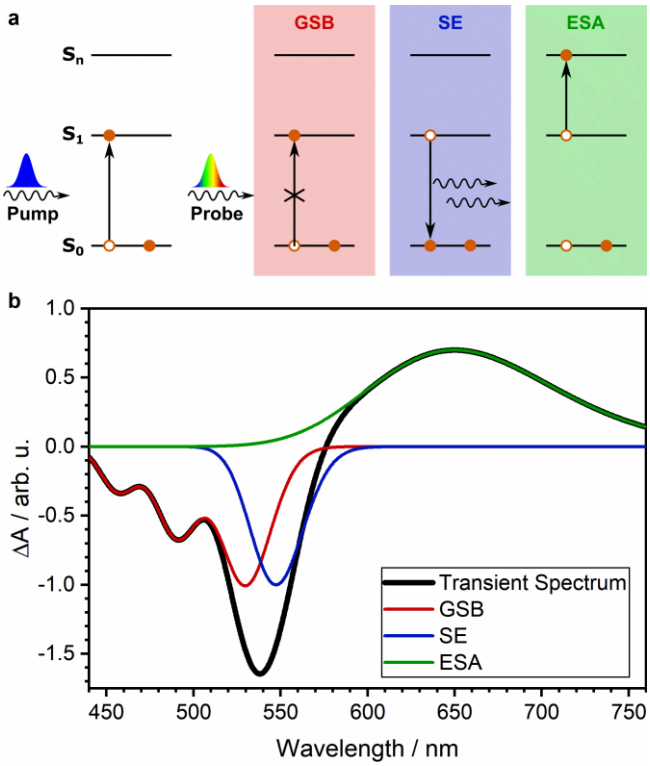


***Figure 3.3**: a) Upon photoexcitation of the chromophore by the pump pulse, three distinct processes generate characteristic spectral features in the transient spectrum. Due to the population of the excited state, the number of ground-state chromophores is reduced. Thus, more probe intensity is transmitted, resulting in a negative ground-state bleach (GSB) signal mirroring the absorption features. Furthermore, an incident photon can incite stimulated emission (SE), which doubles the number of detected photons. Consequently, SE manifests itself as a negative contribution mirroring the spontaneous emission spectrum. Finally, the photon may interact with an excited chromophore and promote it to an even higher excited state. This process is called excited state absorption (ESA). A simulation of the spectral features arising from the three aforementioned processes and the resulting transient spectrum is depicted in panel b.*

A prerequisite for it to occur is the presence of a suitable transition corresponding to the sum of the energy of both photons. TPA is typically only observed for near-UV pulses in organic solvents.[145, 147] Thus, given the excitation wavelengths used in this work exclusively exceed 450 nm, its contribution can be disregarded. The second coherent contribution, SRA, is based on Raman scattering. Initially, the pump pulse populates a virtual energy level. Subsequently, the probe pulse may stimulate an emission back to different vibrational sub-levels of the electronic ground state. This results in an increase of the number of photons, which appears as a negative contribution in the TA signal. Individual vibrational sub-levels can be identified by the characteristic spectral shift of the emitted photons with regard to the pump wavelength.

This effect can clearly be seen in the transient spectrum at time-zero of acetonitrile for a pump wavelength of 470 nm (Figure 3.4). Here, spectral dips are observed at 505, 527 and 547 nm, corresponding to a Stokes-shift of about 1500, 2300 and 3000 $cm^{-1}$, respectively. These values correlate perfectly with reported Raman spectra of acetonitrile.[148] Due to the short lifetime of virtual states, the temporal shape of the SRA signal can be expressed as a Gaussian function

$$\Delta A_{\mathrm{SRA}}(t) = a_{\mathrm{SRA}}\, e^{-2\left(\frac{t-t_0}{\sigma}\right)^2} \qquad \text{Eq. 7}$$

with the amplitude $a_{\mathrm{SRA}}$ , pump-probe cross-correlation $\sigma$, and the time-zero offset $t_0$. The third component within the CA is CPM. It originates from the modulation of the refractive index of the solvent by the intense pump pulse. In consequence, this results in a non-linear frequency shift of the probe pulse. The temporal evolution of the CPM can be approximated as[145]

$$\Delta A_{\mathrm{CPM}}(t) = a_{\mathrm{CPM}}(t-t_0)\, \mathrm{e}^{-2\left(\frac{t-t_0}{\sigma}\right)^2} \times (t-t_0-\tau_{\mathrm{GVD}})\, \mathrm{e}^{-2\left(\frac{t-t_0-\tau_{\mathrm{GVD}}}{\sigma}\right)^2} \qquad \text{Eq. 8}$$

with the amplitude $a_{\mathrm{CPM}}$ and the wavelength-dependent group velocity dispersion $\tau_{\mathrm{GVD}}$. In total, the CA can be described as the sum of SRA and CPM.

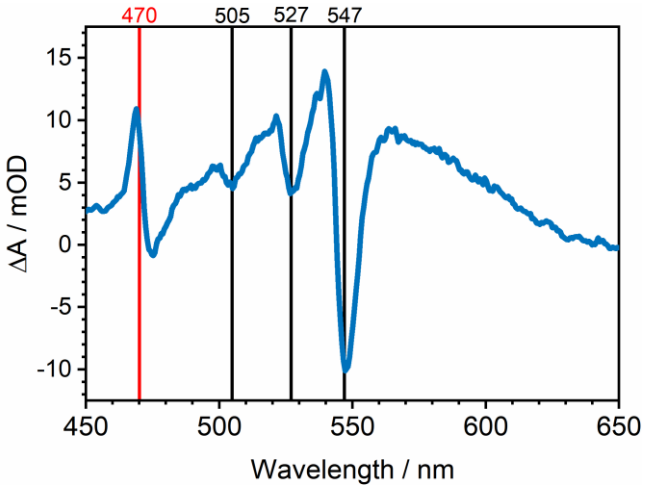


***Figure 3.4:*** *Transient spectrum of acetonitrile at time-zero for an excitation wavelength of 470 nm (red line). The spectrum clearly shows pronounced local minima at 505, 527 and 547 nm (black lines). Their spectral shift with regard to the excitation wavelength amounts to 1500, 2300 and 3000 $cm^{-1}$, respectively. As this coincides with reported values for Raman signals of acetonitrile, the spectral dips are assigned to SRA.*

### 3.3.2 Dispersion Correction

Raw TA data exhibits a wavelength dependent shift in the onset of the transient signal. This effect originates from the chromatic dispersion of the broad probe pulse: If light travels through a medium with a refraction index higher than one, its propagation speed is reduced. In addition, due to the wavelength dependence of the refraction index, the propagation speed of blue-shifted wavelengths is affected more strongly. This introduces a so-called chirp to the probe pulse, which describes a decrease of wavelengths within the envelope of the pulse and increases the overall pulse duration. While the use of reflective optics greatly reduces the amount of chirp imprinted on the probe pulse, the dispersion introduced by the sample itself cannot be removed. In TA measurements, the chirp results in a wavelength dependent shift of time-zero. While the dispersion curve could in principle be determined from the sample data itself, it is typically obtained from measurements of the pure solvent, or a blank substrate. If the experimental parameters are kept constant, the obtained dispersion curve is directly transferrable to the measurement of the sample. Two main benefits of this approach are, on the one hand, that any unwanted sequential contributions of the solvent or substrate are identified. On the other hand, the CA can be fitted to precisely determine the pump-probe cross-correlation and thus time resolution of the experiment as well as the shape of the CA. This method is demonstrated for TAPP-Cl in acetonitrile (Figure 3.5a). In a first step, the CA of the pure solvent is modelled as the sum of a Gaussian function and its first five derivatives with time-zero $t_0$ and pump-probe cross-correlation $\sigma$ as fitting parameters (Figure 3.5b). This approach perfectly describes the solvent signal over the whole spectral range, allowing to extract the FWHM of the pump-probe cross correlation (Figure 3.5c). This shows that the experimental time resolution is <100 fs over the whole spectrum, except for a few outliers at the blue edge. In addition, the wavelength dependent $t_0$ is fitted with a second order polynomial function to obtain the dispersion curve (Figure 3.5d), which is subsequently used to correct the timescale of the raw TA data (Figure 3.5e). The presented example clearly illustrates the feasibility of the approach.

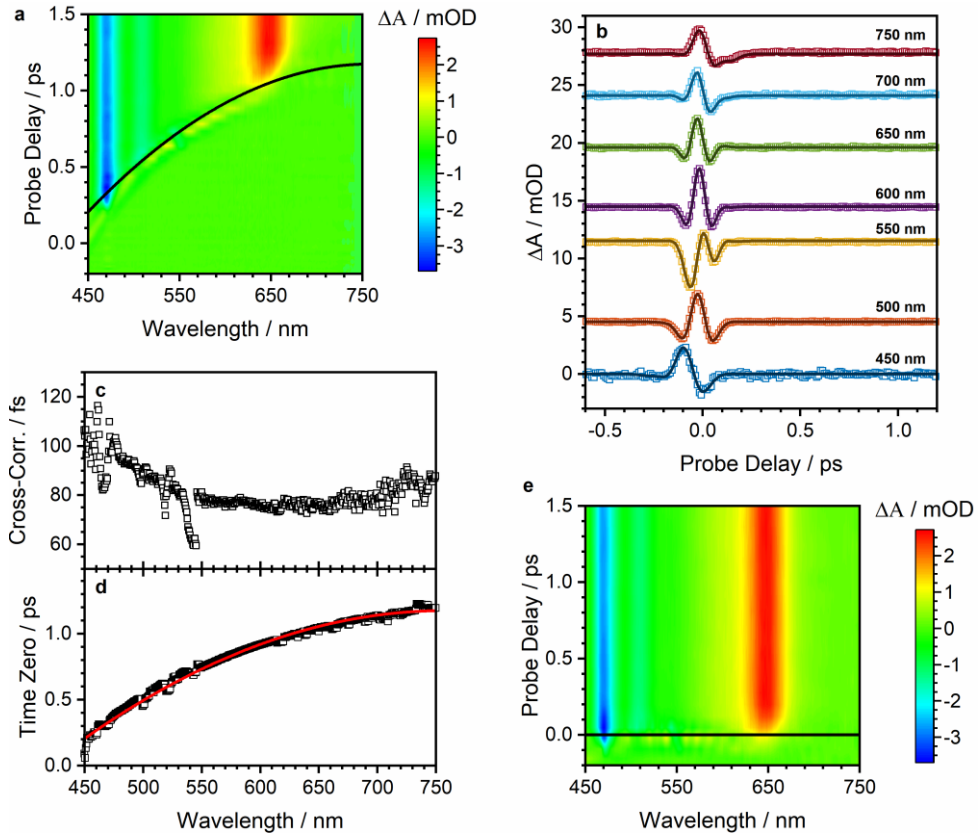


***Figure 3.5:*** *a) Raw 2D TA data of TAPP-Cl in acetonitrile. The chromatic dispersion results in a wavelength-dependent shift of the temporal overlap of pump and probe pulse (black line). The shape of the dispersion curve can be obtained by fitting the coherent artefact in the pure solvent. b) CA at selected probe wavelengths with respective fit traces obtained by modelling the signal as the sum of a Gaussian and its first five derivatives. A perfect fit is achieved over the whole spectral range. c) Barring a few outliers at the blue edge of the spectrum, the FWHM of the pump-probe cross-correlation lies below 100 fs over the spectral range, representing the temporal resolution of the measurement. d) The extracted fit outputs for time-zero are fitted with a 2$^{nd}$ degree polynomial function to obtain the dispersion curve. e) The corresponding dispersion corrected 2D TA data exhibits a uniform onset at $t_0 = 0$, proving the feasibility of the approach.*

### 3.3.3 Global Analysis

Fitting and interpreting TA data allows for the identification of a reaction scheme and rate constants of its comprising steps. This can be done either by fitting single transients by themselves or the whole 2D matrix itself, *i.e.*, a global analysis. Hereof, the latter is preferable, as it typically leads to more accurate data, and allows for the extraction of spectra of individual species. In the following, a method to globally analyse the TA data will be discussed. Initially, the correct temporal evolution of the TA signal has to be obtained, for which reaction kinetics have to be considered. For

photophysical processes, reactions typically follow first order or, given the low fraction of excited chromophores, pseudo-first order kinetics.[149-150]

Thus, regardless of number and combination of consecutive and parallel pathways present in the overall reaction scheme, the population dynamics can be described as the sum of $n$ exponential decays.[149] However, it has to be taken into account that the excitation of the chromophores does not occur instantaneously but over a timespan defined by the temporal width of the pump pulse. Thus, the exponential decay is convoluted with the instrument response $\sigma$. Assuming a Gaussian shape, an analytical solution is available with the result formally corresponding to a probability density function. Thus, for a reaction system with $n$ exponential decays and respective rate constants $k_i$ and amplitudes $a_i$, the TA signal for a single wavelength corresponds to

$$\Delta A(t) = \sum_{i}^{n} a_i \exp\left[\frac{1}{2}(k_i\,\sigma)^2 - k_i(t-t_0)\right] \cdot \operatorname{erfc}\left[\frac{1}{\sqrt{2}}\left(k_i\,\sigma - \frac{t-t_0}{\sigma}\right)\right] \qquad \text{Eq. 9}$$

$$= \sum_{i}^{n} a_i \cdot e_i$$

It is noted that this approach does not include coherent contributions to the signal. However, for the sake of readability and conciseness, the corresponding term will be omitted. A comprehensive description is made in the appendix, section A. Using matrix notation, Eq. 9 can be rewritten as

$$\Delta\mathrm{A(t)} = \sum_{i=1}^{n} a_i \cdot e_i = (a_1\ a_2\ \cdots\ a_n)\begin{pmatrix} e_1 \\ e_2 \\ \vdots \\ e_n \end{pmatrix} = \vec{a} \cdot \vec{e} \qquad \text{Eq. 10}$$

Thus, the vectors $\vec{a}$ and $\vec{e}$ contain the individual preexponential factors and exponential decay, respectively. However, experimentally not only a single wavelength but a broad spectral range is probed, resulting in a 2D matrix (**TA**) for the TA signal. Thus, $\vec{a}$ is be

expanded including one pre-exponential factor for each of the $w$ wavelengths, resulting in matrix $\boldsymbol{A}$:

$$\mathbf{TA} = \sum_{i=1}^{n}\sum_{j=1}^{w} a_{j,i}(\lambda)\cdot e_i(t) = \begin{pmatrix} a_{1,1} & \cdots & a_{1,n} \\ \vdots & \ddots & \vdots \\ a_{w,1} & \cdots & a_{w,n} \end{pmatrix}\begin{pmatrix} e_1 \\ \vdots \\ e_n \end{pmatrix} = \boldsymbol{A}\cdot\vec{e} \qquad \text{Eq. 11}$$

While this expression is analytically correct, it requires an infinitesimal difference between the scanned probe delays, which cannot be achieved. Consequently, $\vec{e}$ is rewritten as a matrix $\boldsymbol{E}$ for the T probe delays:

$$\mathbf{TA} = \sum_{i=1}^{n}\sum_{j=1}^{w}\sum_{l=1}^{T} a_{j,i}\cdot e_{i,l} = \begin{pmatrix} a_{1,1} & \cdots & a_{1,n} \\ \vdots & \ddots & \vdots \\ a_{w,1} & \cdots & a_{w,n} \end{pmatrix}\begin{pmatrix} e_{1,1} & \cdots & e_{1,T} \\ \vdots & \ddots & \vdots \\ e_{n,1} & \cdots & e_{n,T} \end{pmatrix} = \boldsymbol{A}\cdot\boldsymbol{E} \qquad \text{Eq. 12}$$

This expression can be used to globally fit the experimentally obtained data. The columns in the resulting matrix $\boldsymbol{A}$ contain the spectral information of the preexponential factors for each of the $n$ exponential decays and are called *decay associated difference spectra* (DADS). While these DADS represent the best mathematical description of the experimental data, they do not inherently possess physical meaning due to the contributions within the preexponential factor. As the TA signal is detected by observing optical transitions within the excited state manifold, $a$ is proportional to the extinction coefficient $\epsilon$ of a given species and its concentration $c$. Thus, for a total of $s$ species, Eq. 12 can be rewritten as

$$\mathbf{TA} = \sum_{i=1}^{n}\sum_{j=1}^{w}\sum_{l=1}^{T}\sum_{m=1}^{s} \epsilon_{j,m}\cdot c_{m,i}\cdot e_{i,l}$$

$$= \begin{pmatrix} \epsilon_{1,1} & \cdots & \epsilon_{1,s} \\ \vdots & \ddots & \vdots \\ \epsilon_{w,1} & \cdots & \epsilon_{w,s} \end{pmatrix}\begin{pmatrix} c_{1,1} & \cdots & c_{1,n} \\ \vdots & \ddots & \vdots \\ c_{s,1} & \cdots & c_{s,n} \end{pmatrix}\begin{pmatrix} e_{1,1} & \cdots & e_{1,T} \\ \vdots & \ddots & \vdots \\ e_{n,1} & \cdots & e_{n,T} \end{pmatrix} = \boldsymbol{S}\cdot\boldsymbol{C}\cdot\boldsymbol{E} \qquad \text{Eq. 13}$$

Here, the columns of $\boldsymbol{S}$ correspond to the absorption spectrum of the individual species, which are called *species associated difference spectra* (SADS). Comparing the coefficient matrices of Eq. 12 and Eq. 13 and yields

$$\boldsymbol{A} = \boldsymbol{S} \cdot \boldsymbol{C} \qquad \text{Eq. 14}$$

where the concentration matrix $\boldsymbol{C}$ depends on the underlying kinetic model. In order to demonstrate this, a system with the three species X, Y and Z is considered. In principle, two different types of coupled reaction systems are possible: A two-step sequential decay of an initial species and a simultaneous formation of Y and Z.

**Two-step sequential decay ($X \xrightarrow{k_1} Y \xrightarrow{k_2} Z$).** In the first case, species X is initially excited by the pump pulse and subsequently reacts to an intermediate species Y with the rate constant $k_1$. This is followed by the conversion of Y to the final species Z with $k_2$. The final species is assumed to be either a species with its lifetime exceeding the observed temporal range or the ground state. The respective time dependent concentrations are determined by solving the corresponding set of differential equations, yielding the following solutions:

$$\begin{aligned} [X] &= [X]_0 \, e^{-k_1 t} \\ [Y] &= [X]_0 \, \frac{k_1}{k_2 - k_1} \, ( e^{-k_1 t} - e^{-k_2 t}) \\ [Z] &= [X]_0 \left( 1 - \frac{k_2 \, e^{-k_1 t} - k_1 \, e^{-k_2 t}}{k_2 - k_1} \right) \end{aligned} \qquad \text{Eq. 15}$$

In matrix notation, this can be expressed as

$$\begin{pmatrix} [X] \\ [Y] \\ [Z] \end{pmatrix} = [X]_0 \begin{pmatrix} 1 & 0 & 0 \\ \frac{k_1}{k_2 - k_1} & -\frac{k_1}{k_2 - k_1} & 0 \\ -\frac{k_2}{k_2 - k_1} & \frac{k_1}{k_2 - k_1} & 1 \end{pmatrix} \begin{pmatrix} e^{-k_1 t} \\ e^{-k_2 t} \\ 1 \end{pmatrix} = \boldsymbol{C_s} \cdot \boldsymbol{E} \qquad \text{Eq. 16}$$

This shows that the concentrations of the individual components only depend on the product of the scalar initial concentration of A and preexponential coefficients. The resulting matrix $\boldsymbol{C_s}$ is a 3x3 square matrix. Thus, the matrix for the excited species $\boldsymbol{S}$ can be obtained by right multiplying both sides of Eq. 9 with the inverted concentration matrix $\boldsymbol{C_s^{-1}}$, resulting in $\boldsymbol{S = A \cdot C_s^{-1}}$.

**Parallel decay ($\mathbf{X} \xrightarrow{k_1} \mathbf{Y}$; $\mathbf{X} \xrightarrow{k_2} \mathbf{Z}$).** For a parallel reaction, a single exponential decay of A is observed, which comprises the sum of $k_1$ and $k_2$. Species Y and Z again represent a long-lived species or the ground state. Both are formed with the same rate and their concentration is only dependent on the ratio between $k_1$ and $k_2$. The corresponding time dependent concentrations are

$$\begin{pmatrix}[X]\\[Y]\\[Z]\end{pmatrix} = [X]_0 \begin{pmatrix} 1 & 0 \\ -\frac{k_1}{k_2+k_1} & \frac{k_1}{k_2+k_1} \\ -\frac{k_2}{k_2+k_1} & \frac{k_2}{k_2+k_1} \end{pmatrix} \begin{pmatrix} e^{-(k_1+k_2)t} \\ 1 \end{pmatrix} = \boldsymbol{C_p \cdot E} \qquad \text{Eq. 17}$$

In contrast to the sequential model, $\boldsymbol{C_p}$ is not a square matrix and thus cannot be inverted. Thus, to solve Eq. 9 for $\boldsymbol{S}$, both sides are first multiplied from the right with the transposed matrix $\boldsymbol{C_p^T}$.

$$\boldsymbol{A \cdot C_p^T = S \cdot \left(C_p C_p^T\right)} \qquad \text{Eq. 18}$$

The product matrix $\boldsymbol{\left(C_p C_p^T\right)}$ is a square matrix and thus invertible. Consequently, $\boldsymbol{S}$ is obtained as

$$\boldsymbol{S = A \cdot C_p^T \cdot \left(C_p C_p^T\right)^{-1}} \qquad \text{Eq. 19}$$

# 4 Ultrafast Singlet Fission in Tetraazaperopyrene Thin Films

Investigating SF in new materials allows for the distinction between chromophore-specific properties and general characteristics of SF. A promising new class of molecules are TAPPs, as their large aromatic system suggests that they should exhibit a significant diradical character (*cf.* section 2.2.1). In addition, they pack in a slip-stacked geometry, which allows for a crucial overlap of the π–orbitals.[21, 116] Furthermore, reports on PDIs as well as heteroacenes show that aza-substitution has a favourable effect on energetics and dynamics of SF (*cf.* section 2.2.2).[15-16, 21, 29] Thus, it is a valid assumption that SF is feasible in the TAPPs. A further benefit of the TAPPs is that their physical properties can be systematically tuned by substitutions of the aromatic core,[85, 117, 137-138, 151-154] which makes them viable for a wide range of applications ranging from fluorescence markers[138, 152] to n-channel semiconductors.[117, 137, 151]

In this chapter, special focus is laid onto core-halogenated TAPPs and their unsubstituted counterpart (Figure 4.1). Initially, measurements of dilute solutions of TAPP-X are evaluated to determine photophysical properties and dynamics of isolated chromophores (section 4.1). This provides additional insight on the previously observed ISC process[117] as well as on characteristic spectral properties of electronic species in the singlet and triplet manifold. In addition, clear trends between substituents and photophysical properties are established. Subsequently, photophysical processes in TAPP-Cl and TAPP-Br thin films are probed and discussed (section 4.2). Both chromophores exhibit a face-to-face packing with a short interplanar distance of 3.38 and 3.39 Å, respectively, and an almost equal horizontal and vertical displacement.[117] Thus, the effects of changes in the electronic properties can be studied while reducing geometrical factors to a minimum. Coherent formation of the correlated triplet pair is demonstrated, and influences of competing excimer formation and vibrational dynamics on SF are elucidated.

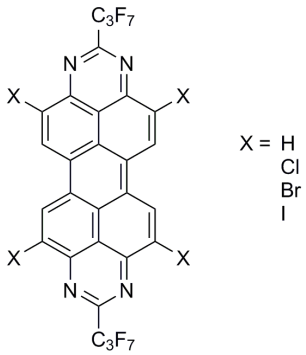


Tetraazaperopyrene (TAPP-X)

***Figure 4.1:*** *Molecular structure of TAPPs investigated in this work.*

## 4.1 Intersystem Crossing in Dilute Solutions of TAPP-X

### 4.1.1 Substitution and Solvent Effects on Stationary Spectra

In a first step, the stationary absorption and emission spectra of dilute solutions of TAPP-X in acetonitrile are evaluated. The spectra for all four chromophores show a pronounced vibronic progression with three distinctive peaks. Regardless of substitution, a separation of ≈1450 $cm^{-1}$ is observed for all compounds (Figure 4.2a). This suggests that the vibrational mode responsible for the spacing is not related to a vibration including the substituents, as their weight differences should result in a significant change of vibrational frequency. In turn, the similarity of the spectra points towards a vibration involving the aromatic core. This is supported by HREELS measurements and quantum chemical calculations, which assign this mode to an asymmetric C-N stretching vibration.[117, 138] While the vibrational progression does not change for different substituents, a systematic red-shift of the absorption maximum from 435 nm for TAPP-H to 488 nm for TAPP-I is observed.

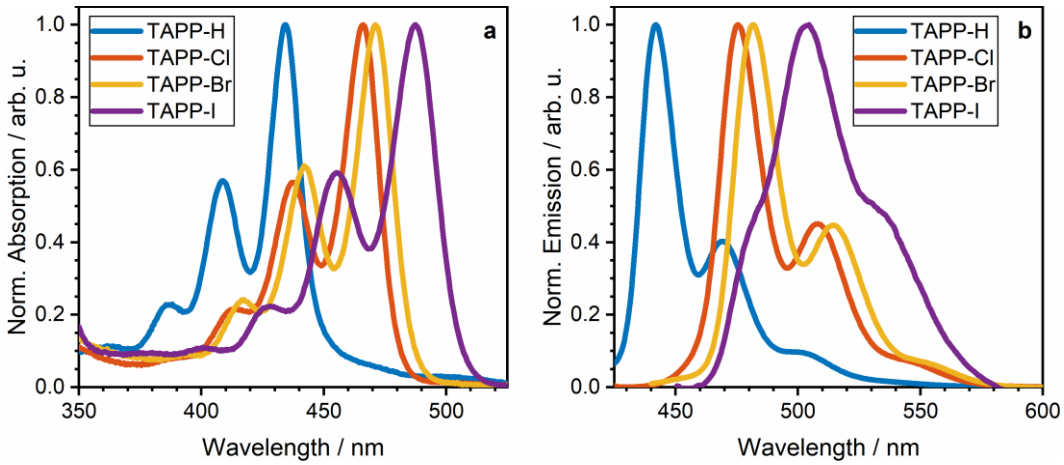


***Figure 4.2:*** *a) The stationary absorption spectra of TAPP-X in acetonitrile exhibit a systematic red-shift with increasing substituent weight due to the destabilisation of the LUMO by the halide substituents. Regardless of substitution, three vibronic peaks are identified with a separation of ≈1450 $cm^{-1}$, which originates from the asymmetric C-N stretch vibration.[117, 138] Quantum chemical calculations allow for an assignment of initial and final state to the $S_0$ and $S_1$, respectively. b) The emission spectra mirror the absorption spectra with the same separation of the vibronic peaks, indicating a rigid molecular structure as well as a similar potential curve. This is supported by quantum chemical calculations, which predict the 0-0 transition to be dominant.[154-155] Reprinted with permission from ref. 155. Copyright © 2020, American Chemical Society.*

This behaviour is rationalized by the interaction of the substituents with the aromatic system. As halides are π-donors, they destabilize the frontier orbitals, *i.e.*, HOMO and LUMO. However, the HOMO energy is increased disproportionally due to a negligible contribution of the substituents on the LUMO.[117] This results in a lower HOMO-LUMO gap and consequently in the observed red-shift. The stationary emission spectra mirror the pronounced vibronic progression of the absorption spectrum and the separation of the vibronic peaks does not change (Figure 4.2b). This is in agreement with quantum chemical calculations, which predict a similar vibrational spectrum for the ground and first excited state.[155] An additional similarity is the low Stokes shift, which increases systematically from 364 to 650 $cm^{-1}$ for TAPP-H and TAPP-I, respectively (Table 4-1). In general, the properties of the stationary spectra point towards a rigid molecular structure with similar potential curves for ground and first excited state. This is in agreement with studies on the hydrocarbon analogue of the TAPPs, peropyrene,[156] and confirmed by a computational study of the absorption and emission spectra using time-dependent DFT.[154] Here, it is demonstrated that TAPP-X has a strong allowed 0-0 transition. Furthermore, the initial and final electronic state has been identified to be the $S_0$ and $S_1$, respectively. In order to elaborate on the nature of the excited state, TAPP-X was dissolved in solvents with different polarities, *i.e.*, relative permittivity $\epsilon_R$. Here, no systematic change in the position of absorption and emission maxima is observed (see appendix section B.1). Thus, a CT character of the excited chromophore, as observed *e.g.* in TAPPs with thiophene substituents,[151] is excluded. Instead, the results point towards an equally nonpolar nature of both ground and excited state, in agreement with reports on peropyrene.[23] This insensitivity on solvent polarity is further predicted by quantum chemical calculations.[155]

***Table 4-1:*** *Absorption and emission maxima and Stokes shift for TAPP-X.*

| Chromophore | $\lambda_{abs}$ / nm | $\lambda_{Em}$ / nm | Stokes shift /$cm^{-1}$ |
|---|---|---|---|
| **TAPP-H** | 435 | 442 | 364 |
| **TAPP-Cl** | 466 | 476 | 450 |
| **TAPP-Br** | 471 | 482 | 484 |
| **TAPP-I** | 488 | 504 | 650 |

### 4.1.2 Substitution Effect on Intramolecular Dynamics

*Temporal Evolution of Transient Spectra.*

All four molecules exhibit a similar temporal evolution of the transient spectra (Figure 4.3). Initially, a negative signal is observed, located in the same spectral region as stationary absorption and emission spectra. Thus, it is assigned to a combination of GSB and SE. Furthermore, a broad ESA band is observed, which exhibits the same dependence as the absorption spectrum, *i.e.*, a systematic red-shift with increasing substituent weight. Its maximum shifts from 620 to 740 nm for TAPP-H and TAPP-I, respectively. This signal as well as the SE vanishes completely on the nanosecond timescale. In line with the emission decay (see appendix section B.2), the transients disclose a systematic acceleration of the decay of the initial species for the halogenated compounds (Figure 4.3). Concomitantly, a non-decaying, blue-shifted ESA band with its blue edge overlapping with GSB emerges, which remains as a non-decaying offset. For all compounds, a transient isosbestic point is observed, which exhibits a systematic red-shift of 20 nm upon increasing substituent weight, moving from 530 nm (TAPP-H) to 590 nm (TAPP-I). This is indicative of a direct state-to-state conversion. The emerging signal possesses two separate peaks for all chromophores but TAPP-I, for which a broad signal without a well-defined maximum is observed. The latter points towards a flatter potential surface with a small sub-level separation. Similar to the initial ESA, a red-shift for the offset is observed, albeit less pronounced, with the maximum moving from 510 nm (TAPP-H) to 530 nm (TAPP-Br). Alongside the spectral changes, the relative signal intensity of the offset with regard to the initial ESA increases. A qualitative comparison of the strength for both ESA can be made by comparing the maxima of the initial ESA and the offset. Here, a weak relative signal intensity of 5.5% and 14% is observed at latest probe delays for TAPP-H and TAPP-Cl, respectively, whereas TAPP-Br (41%) and TAPP-I (29%) exhibit a significantly higher ratio. In general, this change in relative intensity could be either related to a change in population density or a variation of extinction coefficients. Yet, the main contribution becomes apparent when considering the fluorescence quantum yields of the TAPPs.

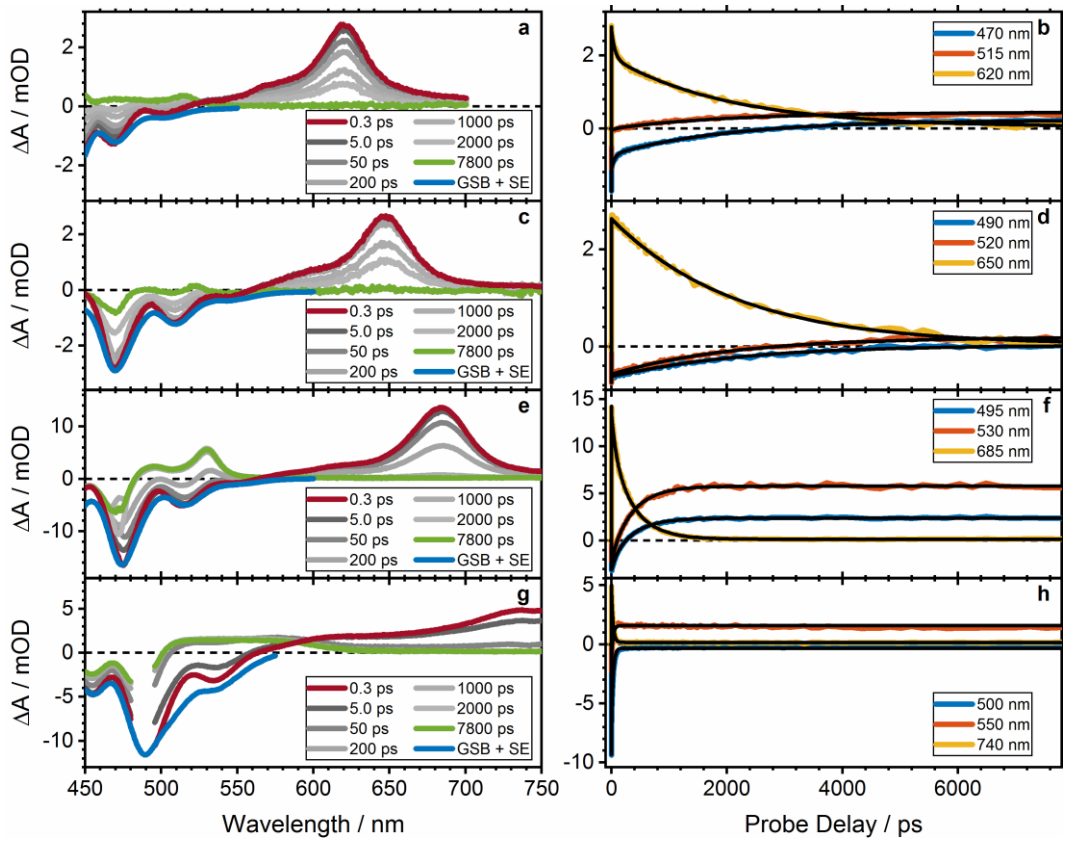


***Figure 4.3:*** *Transient spectra at selected probe delays (left) and selected kinetics with fit traces (right) for (a,b) TAPP-H, (c,d) TAPP-Cl, (e,f) TAPP-Br and (g,h) TAPP-I in acetonitrile. A similar temporal evolution of the transient spectra is observed for all four compounds. Initially, a blue-shifted negative signal, attributed to a combination of GSB and SE, as well as red-shifted ESA is observed. SE and ESA decay on the nanosecond timescale. Simultaneously, a second ESA band emerges, overlapping with the GSB. Two distinct peaks are identified with the exception of TAPP-I, for which a broad signal is observed. The formation of the emerging ESA displays an acceleration with increasing substituent size and its spectral features remain as a non-decaying offset. Reprinted with permission from ref. 155. Copyright © 2020, American Chemical Society.*

A high quantum yield correlates to a loss in excited state chromophores, directly competing with the formation of the second ESA. Thus, an inverse dependence of quantum yield and relative intensity of the latter is expected. This behaviour is qualitatively observed for all compounds but TAPP-I. This deviation can be explained by the broad signal, which suggests an even distribution of oscillator strength over a wide spectral range. Thus, a comparison of the integrated ESA bands would be advisable. This is, however, not advisable in this case due to (i) the overlap of the ESA with GSB, and (ii) the red-shifted part ESA band of TAPP-I exceeding the range of spectral window.

*Characterisation and Quantification of Intramolecular Dynamics by Global Analysis.*

The evolution of the transient spectra is quantified by applying a global multiexponential decay fit to all datasets (Table 4-2). While only one additional distinct set of spectral features is observed besides the initial ESA, two exponential decays are required to obtain a satisfactory fit result. The first time constant, $\tau_1$, corresponds to a homogeneous loss of signal intensity, which is most pronounced for TAPP-H. In addition, no changes in the spectral shape are observed. Within the three halogenated compounds, a systematic decrease of $\tau_1$ with increasing substituent weight from (635 ± 29) ps to (2.36 ± 0.88) ps for TAPP-Cl and TAPP-I, respectively, is observed. This trend does not continue for the unsubstituted TAPP-H, for which a value of (59.6 ± 0.3) ps is obtained. The second time constant, $\tau_2$, describes the transition between the initial ESA band and the non-decaying offset. The obtained values are in good agreement with the emission decay. Consequently, a direct connection between both is drawn, *i.e.*, that $\tau_2$ relates to the decay of the only emissive species. Furthermore, long-time TA measurements were carried out in order to gain insight on the dynamics of the offset spectrum. The temporal resolution of the experimental setup used for these measurements is not sufficient to resolve $\tau_1$ for all compounds as well as $\tau_2$ for TAPP-Br and TAPP-I. In turn, it allows to monitor the dynamics of the second ESA on the microsecond timescale, for which a homogeneous decay is observed in all compounds (see appendix section B.3). This is quantified by global mono- (TAPP-Br, TAPP-I) and biexponential (TAPP-H, TAPP-Cl) decay fit. For the latter two, the results show a good agreement between the first exponential component and $\tau_2$ obtained by short-time TA measurements as well as emission decay (Table 4-2). Thus, the first fitted time constant of the long-time TA measurements is assigned to $\tau_2$. The decay of the second ESA on the microsecond timescale, labelled $\tau_3$, is identical for all halogenated compounds (≈270 ns) and about twice as fast for TAPP-H (159 ± 5 ns). In order to identify the mechanism underlying the observed dynamics, electronic species have to be identified. As the excitation takes place at the lowest absorption band visible in the UV/Vis spectrum, the initial species is assigned to $S_1$, which is supported by quantum chemical calculations.[154] Given that $\tau_1$ is not

related to any spectral changes but a homogeneous decrease in signal intensity, it is assigned to a structural relaxation process. This is accompanied by a redistribution of oscillator strength, which is responsible for the variation in signal intensity. In turn, $\tau_2$ relates to a significant change in the transient spectrum, indicating the formation of a different electronic species. Based on the absent SE in the transient spectrum denoting an optically dark state and its long lifetime (>100 ns), this species is assigned to the triplet manifold. Given that in dilute solution, only intramolecular reaction pathways are to be considered, it can only be generated *via* ISC.

***Table 4-2:*** *Time constants for TAPP-X in acetonitrile, obtained by short and long-time TA measurements.*

| Chromophore | Short-time TA (0-8 ns) | | Long-time TA (0-3 µs) | |
|---|---|---|---|---|
| | $\tau_1$ / ps | $\tau_2$ / ps | $\tau_2$ / ns | $\tau_3$ / ns |
| **TAPP-H** | 59.6 ± 0.3 | 2037 ± 7 | 2.38 ± 0.06 | 159 ± 5 |
| **TAPP-Cl** | 635 ± 29 | 2093 ± 14 | 2.42 ± 0.01 | 281 ± 2 |
| **TAPP-Br** | 81.5 ± 1.9 | 375 ± 3 | n. a. | 268 ± 1 |
| **TAPP-I** | 2.36 ± 0.88 | 29.0 ± 0.8 | n. a. | 275 ± 1 |

*Influence of $S_1 - T_2$ Energy Detuning on Intersystem Crossing Rates.*

As evidenced by the global fit (Table 4-2), the halogenated TAPPs show a systematic decrease of the corresponding time constant with substituent size for halogenated TAPP-X. This is corroborated by fluorescence quantum yields, which clearly show that the dominant decay channel switches from a radiative (TAPP-Cl) to a non-radiative pathway (TAPP-I).

A possible explanation for the observed acceleration is an increasing probability of ISC due to the internal heavy-atom effect. However, if the observations would be based purely on increased spin-orbit coupling, TAPP-H should exhibit a significantly slower time constant, given that the heaviest atom in the molecule is fluorine. In contrast, the time constant for ISC is even slightly lower for TAPP-H in comparison with TAPP-Cl. Thus, further molecular parameters have to be considered. One conceivable property is the energy detuning between energy levels in the singlet and triplet manifold. They can be estimated as vertical transition energies obtained by

single-point DFT calculations using a COSMO model to simulate acetonitrile at the optimised geometry of $S_1$.[155] The results suggest that for all four TAPPs, the energetically closest triplet state to $S_1$ is the second triplet state, $T_2$. Within the accuracy of the method, this transition is predicted to be endothermic by the same amount of 50 meV for TAPP-H and TAPP-Cl. Thus, the energetics of the $S_1 - T_2$ transitions is determined to be the crucial factor for both molecules, outweighing the expected increase of spin-orbit coupling. In addition, a systematic decrease of the $S_1 - T_2$ energy gap is predicted within the halogenated TAPPs with it becoming positive by 10 meV for TAPP-I. Thus, the $S_1 - T_2$ detuning correlates with the observed acceleration of ISC (Figure 4.4a). In summary, the positive feedback regarding more favourable energetics and increased spin-orbit coupling for heavier halide substituents perfectly explain the observed increase of ISC rates. The involvement of $T_2$ would suggest an IC process to $T_1$ according to Kasha's rule.[157] Consequently, an additional time constant for the ESA band assigned to the triplet manifold is expected. However, the fastest observed ISC time constant of 29 ps for TAPP-I is still significantly slower than typical time constants for IC. For example, pyrene exhibits a time constant of 400 fs for the IC from the $S_6$ to $S_1$.[158] Thus, the fast transition of the $T_2$ to $T_1$ is not expected to be resolvable with regard to the timescale of ISC.

### 4.1.3 Identification of Spectral Features of Singlet and Triplet Species

With the identification of the triplet formation process, a comprehensive kinetic model presents itself for all four TAPPs (Figure 4.4b). Upon irradiation, the first excited singlet state $S_1'$ is populated in the Franck-Condon region. Subsequently, a structural relaxation with a concomitant redistribution of oscillator strength takes place, resulting in $S_1$. Due to energetic proximity, the singlet crosses to $T_2$, which undergoes rapid IC to $T_1$. As the timescale of IC is much shorter than ISC, only the lowest triplet state is

observed. Finally, a slow relaxation of $T_1$ occurs on the microsecond timescale. Thus, the observed kinetics depict a sequential model with three steps:

$$S_1' \xrightarrow{\tau_1} S_1 \xrightarrow{\tau_2} T_1 \xrightarrow{\tau_3} S_0 \qquad \text{Eq. 20}$$

Using the approach outlined in section 3.3.3, the corresponding coefficient matrix was formulated and applied to the fit results to obtain the SADS of the respective TAPP-X (Figure 4.4c to e). Here, a red-shift of $S_1'$ with increasing substituent size is observed, in agreement with the transient spectra at early probe delays (*vide supra*). Analogous to the stationary spectra, the origin of this shift is assigned to the expansion of the π-system by the halide substituents, which decrease the energy gaps between electronic states. As expected, the structurally relaxed $S_1$ exhibits the same spectral features as its predecessor, albeit with its amplitude lowered by about one third. This is compatible with the observed loss of signal intensity related to $\tau_1$. For TAPP-H and TAPP-Cl, results from both short- and long-time measurements agree perfectly, showing the transferability between both experimental setups. The final SADS are assigned to $T_1$. They represent the offset for the short-time and a decaying component in long-time TA measurements, respectively. In line with the $S_1$ SADS, a great agreement is achieved between short- and long-time measurements. With the exception of the broad absorption peak observed for TAPP-I, the $T_1$ SADS show two vibronic peaks, which exhibit a slight red-shift for heavier substituents (*vide supra*).

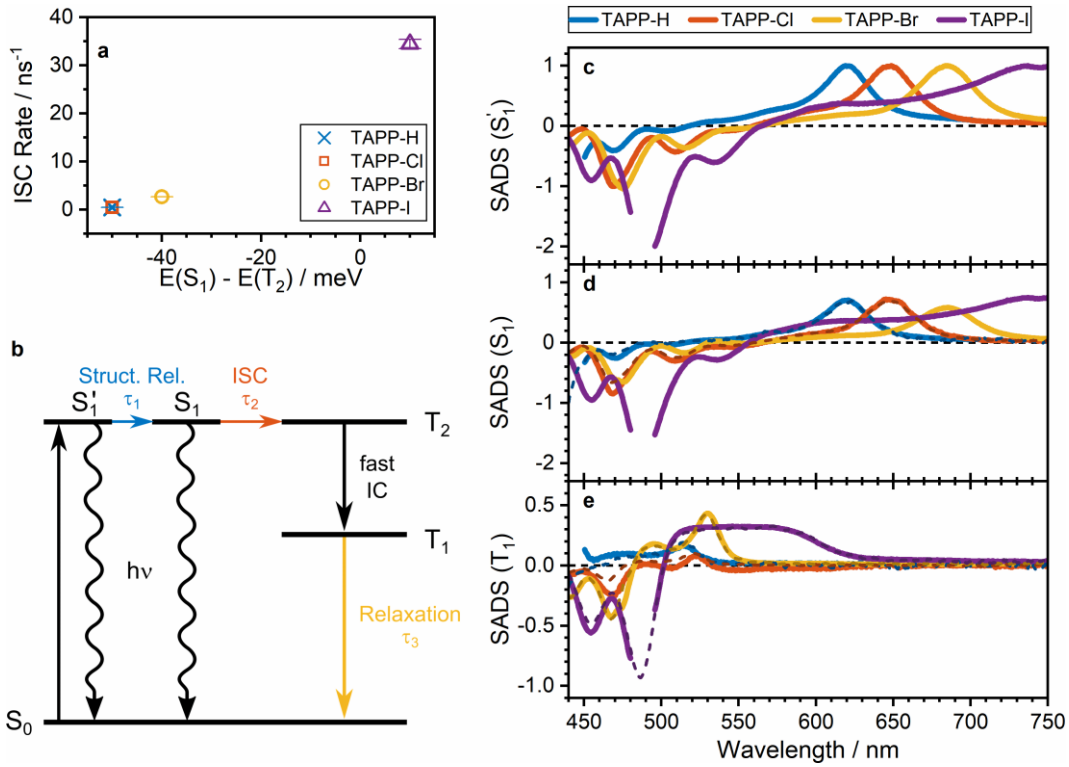


***Figure 4.4:*** *a) The inverse of $\tau_2$, i.e., the ISC rate, correlates with the energy detuning between $S_1$ and $T_2$, indicating a direct transition between both states. This suggests that enhanced spin-orbit coupling is not the singular effect for the observed acceleration of ISC. In turn, the similar energy detuning of TAPP-H and TAPP-Cl explains their similar time constants. b) Proposed kinetic model for TAPP-X. Upon irradiation, the respective chromophore is excited to $S_1'$ in the Franck-Condon region. This is followed by a structural relaxation to $S_1$. Subsequently, the excited singlet crosses to the energetically close $T_2$. In a fast IC process, the lowest state in the triplet manifold, $T_1$, is populated. As this occurs on significantly faster timescales compared to ISC, it is not resolved experimentally. Finally, $T_1$ relaxes to the ground state on the microsecond timescale. This sequential kinetic model is used to determine the SADS of electronic species for both short (solid lines) and long-time TA measurements (dashed lines). Given the great agreement, they are described simultaneously. SADS are normalised for the maximum of the $S_1'$ SADS to allow for a better comparison. c) $S_1'$ exhibits a strong contribution of GSB and SE, as well as a red-shifted absorption feature. In accordance to stationary absorption spectra, the latter is systematically red-shifted with substituent weight. d) $S_1$ possesses the same spectral features as its predecessor, albeit with its intensity being reduced by about one third. e) Within the $T_1$ SADS, two vibronic peaks are observed for TAPP-H, TAPP-Cl and TAPP-Br, which exhibit a slight red-shift with increasing substituent weight. In contrast, a broad signal is observed for TAPP-I, which suggests a flat potential surface. The SADS show a great agreement regardless of the monitored time window. Adapted with permission from ref. 155. Copyright © 2020, American Chemical Society.*

### 4.1.4 Conclusion

First, the missing dependence of stationary spectra on solvent polarity indicates that $S_1$ does not possess CT character. It is, however, noted that a delocalised excitation in the densely packed solid state might result in intermolecular CT states. Second, distinct spectral features of $S_1$ and $T_1$ have been identified, which are crucial electronic species in the SF mechanism and thus may contribute to its identification. Finally, intramolecular photophysical processes, *i.e.*, structural relaxation and ISC, and their respective timescales have been determined. The trends observed for ISC within the four investigated TAPPs allows for the conclusion that the photoexcited $S_1$ crosses to the energetically close $T_2$. The acceleration of this process with increasing substituent size is attributed to a combination of energetic detuning, and the heavy-atom effect. The proximity of $S_1$ and $T_2$ further suggests that TTA may potentially reduce triplet yields achieved by SF. In addition, the time constants (>80 ps) of the photophysical processes are unlikely to compete with an efficient SF on a picosecond timescale. A final aspect to be considered in the subsequent thin-film studies is the potential influence of the heavy-atom effect on SF. As observed in previous studies, this may aid in the separation of the correlated triplet pair into free triplets.[131] Overall, the obtained results yield important pieces of information used for the disentanglement of the dynamics of TAPP-Cl and TAPP-Br thin films discussed in the next section.

## 4.2 Coherent Triplet Formation in Halogenated Tetraazaperopyrenes

### 4.2.1 Aggregation Effects on Stationary Spectra of TAPP-Cl and TAPP-Br

The stationary spectra of TAPP-Cl and TAPP-Br thin films show characteristic differences in comparison to the respective spectra in solution (Figure 4.5). For both compounds, a red-shift of the absorption maximum to 509 and 517 nm is observed, amounting to an energy difference 225 and 234 meV for TAPP-Cl and TAPP-Br, respectively. In addition, the absorption band experiences a broadening of the absorption band, weakening the pronounced vibronic structure. Both effects are attributed to the formation of J-aggregates in solid state.[159] Nevertheless, the three vibronic peaks observed in solution can still be distinguished on solid state. However, the separation of the vibronic peaks previously attributed to the C-N stretching mode is varied. For the first two vibronic peaks, the separation increases from ≈1450 $cm^{-1}$ in solution to 1675 and 1622 $cm^{-1}$ for TAPP-Cl and TAPP-Br thin films, respectively. A qualitatively comparable shift of this mode has been observed for TAPP-Cl and TAPP-Br multilayers.[117] Thus, this observation is attributed to the interaction of the aromatic systems within the molecular crystals, which change the vibrational frequency. In addition, the separation between the second and third vibronic peak is significantly lower at 1150 and 1062 $cm^{-1}$ for TAPP-Cl and TAPP-Br, respectively. This effect can be rationalised by an increased anharmonicity in the solid state. Like the ground-state absorption, the stationary emission spectra exhibit a red-shift and a broadening of the peaks compared to solution measurements. Furthermore, the relative intensity of the second vibronic peak with respect to the emission maximum is increased significantly. In TAPP-Br thin films, this ratio is roughly doubled from 0.45 to 0.87. For TAPP-Cl, the fourfold increase from 0.51 to 2 results in the second vibronic peak becoming the dominant transition.

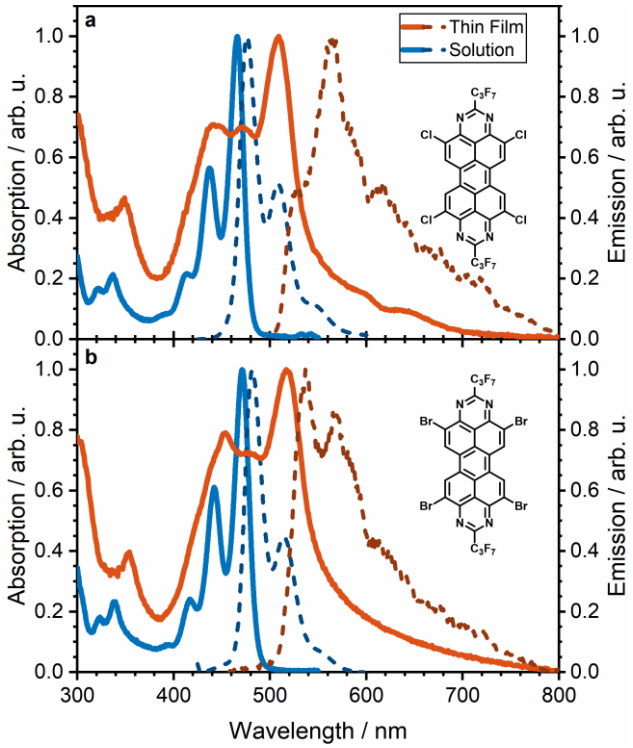


***Figure 4.5:*** *The stationary absorption (solid lines) and emission spectra (dashed lines) of a) TAPP-Cl and b) TAPP-Br show significant differences between measurements in thin film and solution. In general, a red-shift combined with a broadening of the vibronic peaks is observed. Both effects are attributed to π–π-interactions in the solid state. The separation of the first and second vibronic peaks is increased from ≈1450 $cm^{-1}$ to 1675 and 1622 $cm^{-1}$ for TAPP-Cl and TAPP-Br, respectively. This is consistent with the observed shift of the C-N stretching vibration to higher energies in multilayers of the respective compound.[117] Reprinted with permission from ref. 155. Copyright © 2020, American Chemical Society.*

## 4.2.2 Time-Resolved Measurements

*Long-lived Emissive Species Evidenced by Time-Resolved Emission.*

The observations for the stationary emission spectra are complemented by TCSPC measurements. Here, the emission decay at the blue edge of the emission spectra for both TAPP-Cl and TAPP-Br follow the shape of the instrument response function (IRF, Figure 4.6). Thus, an emission decay faster than the temporal resolution of the setup is indicated. In turn, a long-lived component is observed at higher emission wavelengths. This implies the presence of a red-shifted emissive species decaying on a longer timescale than prompt fluorescence. This second component is more pronounced for TAPP-Cl, which speaks for a higher population of the second emissive species.

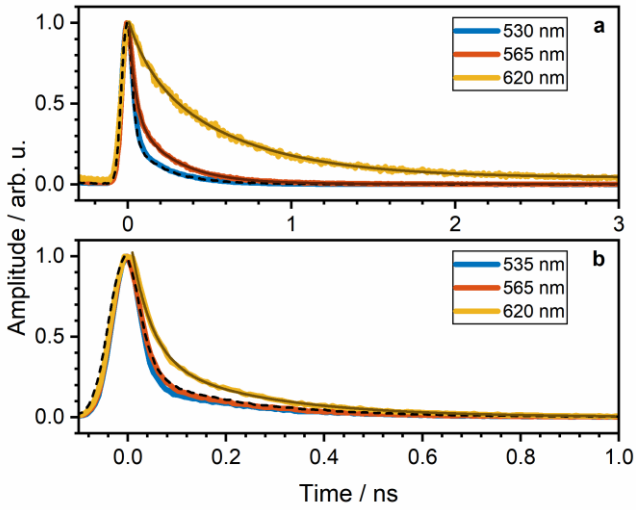


***Figure 4.6:*** *The time-resolved emission traces of a) TAPP-Cl and b) TAPP-Br show a decay faster than the temporal resolution of the setup. At higher wavelengths, an additional long-lived component is observed, indicating the presence of an additional emission band overlapping with prompt fluorescence. For the emission wavelength of 620 nm, a biexponential fit shows a stronger relative contribution of the red-shifted component for TAPP-Cl (76.8%) compared to TAPP-Br (36.6%). The proposed presence of a red-shifted emissive species agrees with the observed increased intensity in the stationary emission spectra at higher wavelengths (Figure 4.5). Reprinted with permission from ref. 155. Copyright © 2020, American Chemical Society.*

The observed effects are quantified by a biexponential fit (Table 4-3). For TAPP-Cl, an increase of the time constants obtained for emission wavelengths of 565 and 620 nm is observed. This is accompanied by a significant increase of the amplitude of the long-lived component, which rises from 42.3% to 76.8%. Both findings agree with the presence of an additional emission band overlapping with the red tail of prompt fluorescence. For TAPP-Br, only the highest monitored wavelength (620 nm) allows for an identification of the long-lived component. In addition, its relative amplitude (36.6%) is significantly weaker compared to TAPP-Cl. This agrees with the observed increased ratio of the vibronic peaks in the stationary emission spectra, suggesting a higher contribution of the red-shifted species in TAPP-Cl.

***Table 4-3:*** *Results for a biexponential fit of TCSPC traces of TAPP-Cl and TAPP-Br thin films. Values in brackets indicate the normalized amplitude of the time constant.*

| Molecule | Wavelength / nm | $\tau_1$ / ps | $\tau_2$ / ps |
|---|---|---|---|
| **TAPP-Cl** | 565 | 39.2±0.5 (57.7) | 257±2 (42.3) |
| | 620 | 127±11 (23.2) | 595±11 (76.8) |
| **TAPP-Br** | 620 | 41.8±1.0 (63.4) | 234±8 (36.6) |

*Spectral Evolution of Transient Spectra.*

In the following, short-time TA measurements are discussed. Due to the intense pump scattering around the excitation wavelength, *i.e.*, 515 and 520 nm for TAPP-Cl and TAPP-Br, respectively, the spectral region ±10 nm is removed. The transient spectra of both compounds share similar spectral features at earliest probe delays (Figure 4.7). For both molecules, an intense negative signal is observed, which coincides with the emission band and is consequently assigned to SE. Besides that, two distinct ESA bands are present, one of which is located in the red part of the probed spectral window (>630 nm). Here, a broad peak is observed with its maximum at 690 and 710 nm for TAPP-Cl and TAPP-Br, respectively. This corresponds to a bathochromic shift of 50 meV for the brominated TAPP. The second ESA band is blue-shifted exhibits a narrow lineshape and overcompensates the expected GSB. Its maximum shifts from 489 nm (TAPP-Cl) to 498 nm (TAPP-Br), which amounts to the same value observed for the broad ESA band. In addition, the relative intensity of the narrow ESA with regard to the red-shifted feature increases from 36% (TAPP-Cl) to 62% (TAPP-Br). Within the first 5 ps after photoexcitation, a significant decrease in signal intensity is observed over the whole spectral range. While this decay is homogeneous for both ESA bands, the SE retains a higher signal intensity around 610 and 615 nm for TAPP-Cl and TAPP-Br, respectively. Following the initial fast decay, the red-shifted ESA continues losing intensity until it is almost completely vanished at a probe delay of 100 ps. In contrast, the signal for narrow ESA peak remains constant at about one third of its initial intensity. Furthermore, an additional weak ESA at 465 nm becomes apparent in the transient spectra for TAPP-Br. At this exact spectral location, a local maximum of the GSB is present at earliest probe delays. Consequently, it is assumed that this feature originates from the same transition corresponding to the peak at 498 nm, albeit initially overcompensated by GSB. A similar feature is vaguely discernible in the transient spectrum of TAPP-Cl. However, it is located at the blue edge of the spectral range and cannot be discerned reliably. Moving to later probe delays, no additional evolution of the transient spectra is observed for TAPP-Cl. Hence, the weak, blue-shifted ESA signal remains as a non-decaying offset on the monitored timescale.

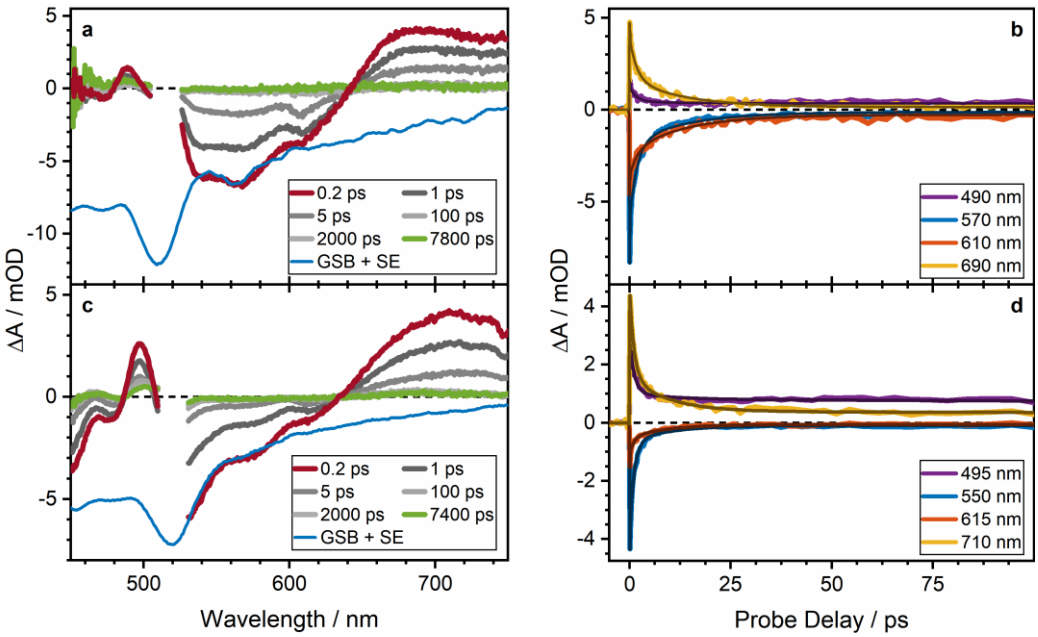


***Figure 4.7:*** *Transient spectra at selected probe delays (left) and transients (right) for (a,c) TAPP-Cl and (b,d) TAPP-Br. Both molecules show a strong contribution of SE at early probe delays. In addition, two positive features are present: A broad ESA at high wavelengths, and a narrow, blue-shifted ESA overcompensating the GSB. Within the initial 5 ps, a significant decrease in signal intensity is observed. This decay is equally strong for the ESA bands. In contrast, the SE features retains more of its original intensity at wavelengths around 610 and 615 nm for TAPP-Cl and TAPP-Br, respectively. The red-shifted ESA subsequently decays almost completely until a probe delay of 100 ps. On the same timescale, the narrow ESA peak retains about one third of its initial intensity. No further evolution is apparent for TAPP-Cl. In contrast, a weak homogeneous decrease occurs in TAPP-Br. For both compounds, a non-decaying offset is observed, with a stronger signal intensity for TAPP-Br. Reprinted with permission from ref. 155. Copyright © 2020, American Chemical Society.*

In turn, a further homogeneous decrease of the transient spectrum is observed for TAPP-Br. Nonetheless, the intensity of the signal remains above that of TAPP-Cl. In consequence, reliable long-time TA data could only be collected for TAPP-Br (see appendix section C.1). As suggested by the non-decaying offset in short-time measurements, both SE and the red-shifted ESA only possess a weak intensity on this timescale. In contrast, the two vibronic peaks of the blue-shifted ESA are clearly discerned at early probe delays (1 ns) and exhibit a homogeneous decay on the microsecond timescale. The qualitative observations of the transient spectra are complemented by a global multiexponential fit (Table 4-4). For the short-time TA data, a biexponential decay fit with an offset is used for TAPP-Cl. In turn, three exponential decays and an offset are required for a satisfactory fit of TAPP-Br. The long-time dynamics of TAPP-Br indicate biexponential decay.

***Table 4-4:*** *Time constants obtained by a global multiexponential fit of the short- and long-time TA data.*

| Molecule | Short-time (0-8 ns) | | | Long-time (0-1 µs) | |
|---|---|---|---|---|---|
| | $\tau_1$ / ps | $\tau_2$ / ps | $\tau_3$ / ps | $\tau_4$ / ns | $\tau_5$ / ns |
| **TAPP-Cl** | 1.77 ± 0.01 | 13.4 ± 0.07 | n.a. | n.a. | n.a. |
| **TAPP-Br** | 1.12 ± 0.01 | 9.55 ± 0.10 ps | 531 ± 16 | 12.5 ± 0.4 | 165 ± 3 |

### 4.2.3 Vibrational Coherence in TAPP-Br

An additional feature observed for short (<9 ps) probe delays at selected probe wavelengths is the presence of periodic variations in signal intensity. These features correspond to a vibrational coherence, *i.e.*, the oscillation of a vibrational wavepacket generated by the pump pulse (*cf.* section 2.1.3). The oscillatory features can be clearly discerned in measurements with small steps of the probe delay (see appendix section C.2). However, their weak intensity in TAPP-Cl significantly hampers their interpretation. Thus, the ensuing discussion will be based on measurements of TAPP-Br. In order to extract the frequencies of the periodic oscillations, a fast Fourier transform (FFT) was carried out on the residuals of a global biexponential with an offset. Residuals for probe delays <200 fs were omitted to avoid artefacts from the coherent spike. The resulting 2D matrix, allows for an analysis of vibrational frequencies over the whole spectral range (Figure 4.8a). An immediate observation is that the oscillatory features exhibit their strongest intensity close to the excitation wavelength. Additionally, frequencies of five major vibrations are identified at 20, 50, 125, 150, and 205 $cm^{-1}$. In order to screen for a possible wavelength dependent shift of these modes, spectral cuts at selected probe wavelengths are analysed (Figure 4.8b). However, neither of the vibrational frequencies exhibit a shift. In a subsequent step, the temporal evolution of the amplitude of the individual contributions is to be analysed. This allows to link individual oscillations to population dynamics of electronic states.[47]

*Modelling of Oscillatory Features.*

A typical approach for that would be a sliding-window FFT. This is, however, not feasible in this case due to the long oscillation period of the 20 $cm^{-1}$ mode with regard to its dephasing time: Within the observed time window of 9 ps, the initially strong intensity of this mode decreases almost completely, suggesting a dephasing time of about 2 ps (Figure 4.8c). Thus, the amplitude decreases significantly even within one oscillation period (1.67 ps). This severely limits the meaningfulness of a sliding-window FFT. Thus, the experimental signal intensity with regard to the probe delay $t$ is modelled explicitly. Besides the contributions of the oscillatory components $\Delta A_{\mathrm{Osc},i}$, the model includes contributions of the exponential population decay $\Delta A_{\mathrm{Exp}}$, a non-decaying offset $\Delta A_{\mathrm{Off}}$ as well as a combination of cross-phase modulation $\Delta A_{\mathrm{CPM}}$ and stimulated Raman amplification $\Delta A_{\mathrm{SRA}}$ to describe the coherent artefact $\Delta A_{\mathrm{CA}}$ (*cf.* section 3.3.1). The fit was carried out for the probe wavelength of 495 nm, as it exhibits the most pronounced oscillatory features. The exponential population decay is modelled straightforward as a monoexponential decay with the time constant $\tau_{dec}$. The width of the pump pulse $\sigma$ is accounted for by the analytical solution for the convolution of an exponential decay and a Gaussian (*cf.* section 3.3.3). The offset is modelled as

$$\Delta A_{\mathrm{Off}}(t) = \mathrm{erfc}\left(-\frac{t}{\sigma}\right) \qquad \text{Eq. 21}$$

The coherent artefact is treated as a combination of CPM and SRA. Here, two more parameters are introduced, *i.e.*, the group velocity dispersion $\tau_{\mathrm{GVD}}$ and the SRA gain $\tau_{\mathrm{SRA}}$.

$$\begin{aligned}\Delta A_{\mathrm{CA}}(t) &= \Delta A_{\mathrm{CPM}}(t) + \Delta A_{\mathrm{SRA}}(t) \\ &= t e^{-2\left(\frac{t}{\sigma}\right)^2} \cdot (t - \tau_{\mathrm{GVD}})\, e^{-2\left(\frac{t-\tau_{\mathrm{GVD}}}{\sigma}\right)^2} + e^{-2\left(\frac{t-\tau_{\mathrm{SRA}}}{\sigma}\right)^2}\end{aligned} \qquad \text{Eq. 22}$$

For the oscillatory component, each of the five major contributions is modelled as a sinusoidal with an individual angular frequency $\omega_i$ and phase shift $\Phi_i$. In order to attribute for the dephasing of the vibrational coherences, the sinusoidal is multiplied with an exponential decay with the dephasing time constant $\tau_{\mathrm{dep},i}$. Finally, the instrument response is accounted for by an additional multiplication with the error function including the width of the excitation pulse, $\sigma$. Consequently, the oscillatory contributions $\Delta A_{\mathrm{Osc}}$ of the signal are described as

$$\Delta A_{\mathrm{Osc}}(t) = \sum_{i=1}^{5} \left[ \sin(\omega_i t + \phi_i) \times \mathrm{e}^{-\frac{t}{\tau_{\mathrm{dep},i}}} \times \mathrm{erfc}\left( \frac{\sigma}{2\tau_{\mathrm{dep,i}}} - \frac{t}{\sigma} \right) \right] \qquad \text{Eq. 23}$$

In total, the experimental signal is modelled as the sum of all individual contributions:

$$\Delta A(t) = \Delta A_{\mathrm{EXP}}(t) + \Delta A_{\mathrm{OFF}}(t) + \Delta A_{\mathrm{CA}}(t) + \Delta A_{\mathrm{Osc}}(t) \qquad \text{Eq. 24}$$

The fit accurately reproduces the experimental transient at a probe wavelength of 495 nm (Figure 4.8c). In addition, the residuals exhibit no periodic structure (Figure 4.8d), proving that no further vibrational mode is present for the given experimental resolution. While all results are collected in the appendix (section C.2), characteristic quantities will be discussed in detail. The time constant for the exponential population decay amounts to $\tau_{dec}$ = 1.88 ps, which is reasonably close to the time constant obtained by a global fit (1.12 ps, *vide supra*). The discrepancy is not unexpected, as the initial population decay coincides with the decreasing part of the first oscillation period of the 20 cm$^{-1}$ mode. Consequently, a fit purely based on population dynamics will assume a faster time constant. In addition, the fit allows for the extraction of the individual vibrational modes of the oscillatory component (Figure 4.8e). The obtained frequencies of 19.9, 52.5, 126, 143, and 206 cm$^{-1}$ perfectly coincide with the major contributions observed in the FFT spectra. The four vibrations with the lowest energies exhibit an expected decrease of dephasing times from 2.73 ± 0.15 ps to 1.30 ± 0.40 ps.[160] Contrarily, the vibrational mode at 206 cm$^{-1}$ contradicts the trend with a dephasing time of 2.73 ± 1.20 ps. However, given the low amplitude and consequently high error margin, no unambiguous statement can be made in this case.

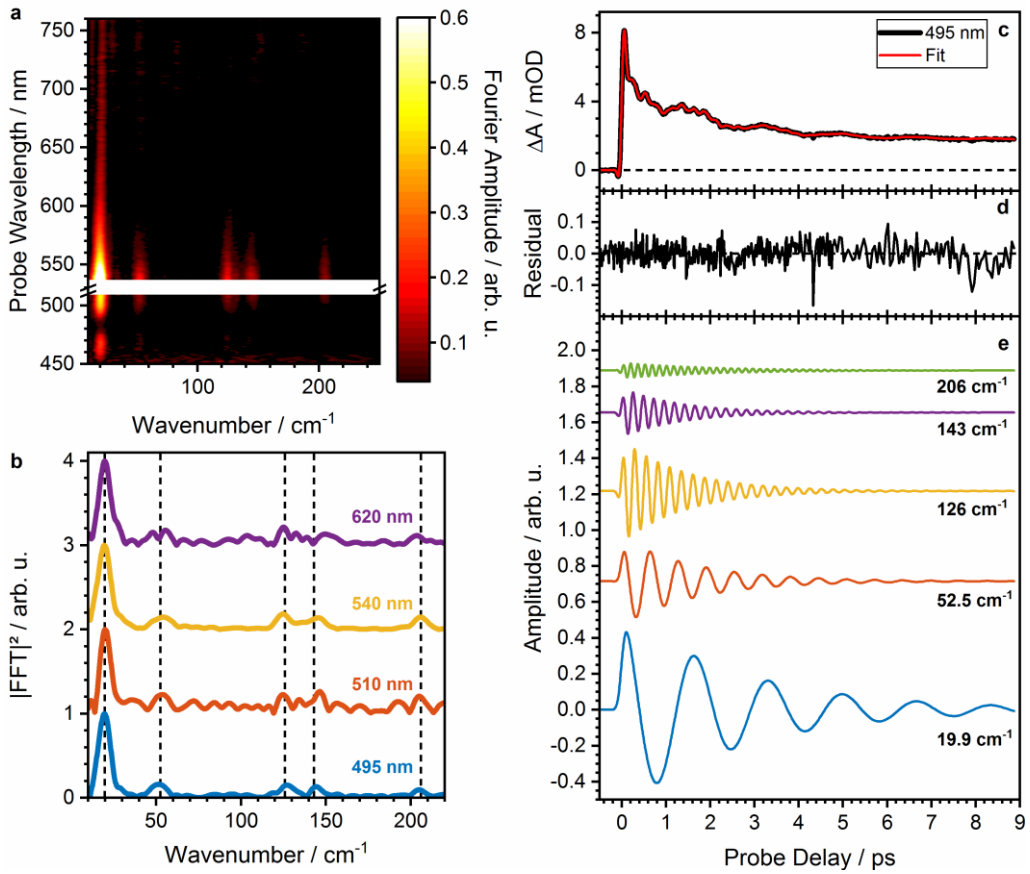


***Figure 4.8:*** *a) The spectrally resolved 2D-FFT of the residuals of a global fit of a TA measurement of a TAPP-Br thin film with a narrow time window (0-9 ps) and small steps of the probe delay (see appendix section C.2) exhibits five major contributions around 20, 50, 125, 150, and 205 $cm^{-1}$. They exhibit the strongest intensity close to the excitation wavelength (520 nm). b) Spectral cuts at selected probe wavelength show constant frequencies over the whole spectral range. c) The transient at 495 nm is fitted using a model containing a physical description of the coherent artefact, a monoexponential decay with offset, and five sinusoidals to account for oscillatory components. d) The residuals of the fit show no periodic structure, proving that no further vibrational mode is present for the given experimental resolution. e) The individual oscillatory components show an acceleration of their dephasing time for all but the 205 $cm^{-1}$ mode. The deviation for the latter originates from its low amplitude, thus making it prone to error. Reprinted with permission from ref. 155. Copyright © 2020, American Chemical Society.*

*Distinction Between Intra- and Intermolecular Modes.*

In the following, the distinction of inter- and intramolecular vibrational modes is addressed. In this context, a near-resonant IVS measurement of a dilute solution of TAPP-Br in acetonitrile was carried out. As demonstrated in section 4.1, no interactions with other chromophores are present under these experimental conditions. Thus, any observed vibrational modes can be assigned straightforward to an intramolecular mode.

For the experiment, an experimental setup differing from those described in section 3.2 was used, which is described in detail elsewhere.[161-162] In short, the setup consists of two home-built non-collinear optical parametric amplifiers (NOPA) with centre wavelengths of 521 and 625 nm, and pulse durations (FWHM) of 21.6 and 24 fs, respectively (see appendix section C.3). The blue-shifted NOPA was used to excite the sample near-resonant, while the latter acts as a probe pulse. Due to the spectral width of the latter, transients in the range of 590 to 660 nm can be extracted (Figure 4.9a). Here, a clearly visible vibrational coherence as well as a weak contribution of an exponential decay can be discerned. The latter was fitted with a monoexponential tail fit at probe delays >130 fs to avoid contributions of the intense coherent artefact. The fit trace was subtracted to obtain the pure oscillatory components in the residuals, which dephases within the observed timescale of 3 ps and is most pronounced in the blue and red wings of the probe spectrum (Figure 4.9b). The corresponding vibrational frequencies were obtained by applying an FFT on the residuals (Figure 4.9c-g). Regardless of probe wavelength, the most intense signal is observed at 380 $cm^{-1}$. This peak is assigned to the C-C≡N bending vibration of the solvent acetonitrile.[148] For probe wavelengths of 590, 650, and 660 nm, no further vibrational modes are observed. In turn, two additional signals are present for 600 and 610 nm, located at 185 and 260 $cm^{-1}$. Comparing the FFT spectrum of the dilute solution with the results obtained for solid state, a distinct lack of low-frequency modes becomes apparent. This is attributed here to a fast dephasing due to solute-solvent interactions. In general, the only common Raman mode for both solution and solid-state measurements is located around 200 $cm^{-1}$: For solutions, a frequency of 185 $cm^{-1}$ is observed, whereas a similar value of 205 $cm^{-1}$ is observed in thin films. This shift of vibrational modes to higher frequencies in solid state resembles the observations made for the stationary absorption spectra (*vide supra*). Thus, the observed frequencies in both dilute solution and thin film are assigned to originate from the same intramolecular mode.

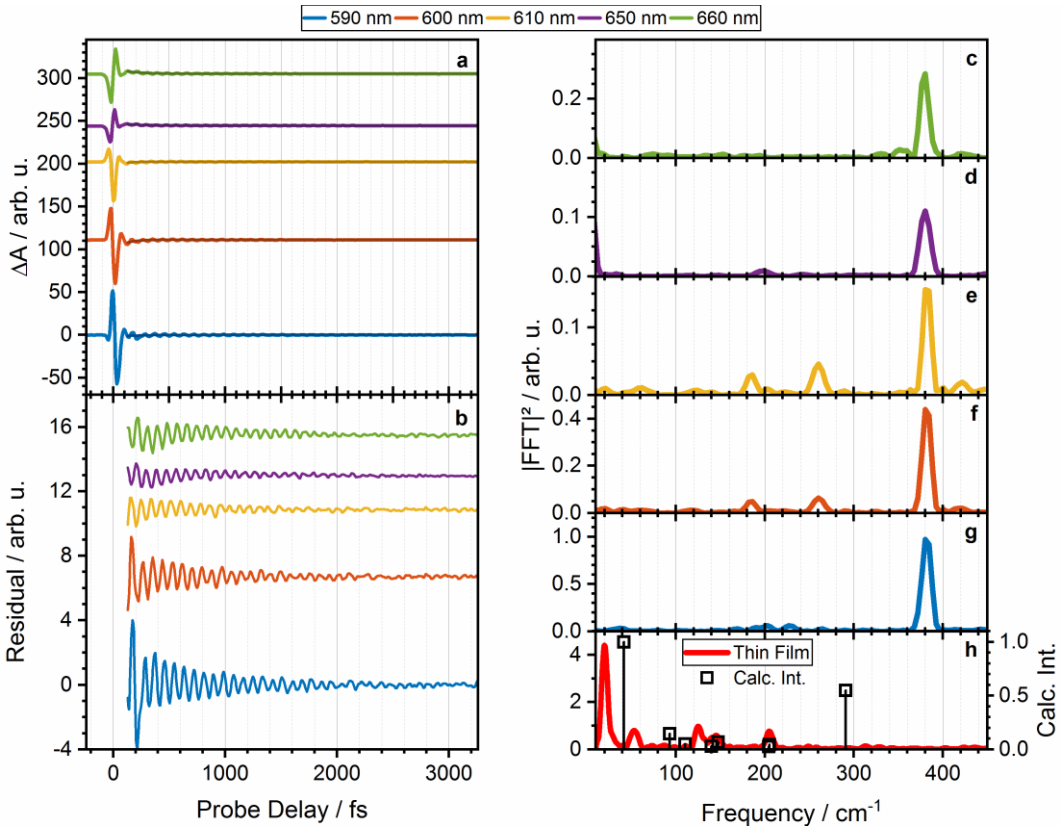


***Figure 4.9:*** *a) Transients at selected probe wavelengths for a near-resonant IVS measurement of a dilute solution of TAPP-Br in acetonitrile show an oscillatory feature, which is more pronounced at the wings of the probe spectrum. A monoexponential tail fit is applied for probe delays >130 fs, to avoid artefacts from the intense coherent artefact. b) Subtracting the exponential fit from the transients clearly depicts the periodic oscillations in the signal. c-g) An FFT is performed for the residuals of the individual transients to obtain the respective vibrational spectra. For all wavelength, a strong contribution of the 380 cm$^{-1}$ mode is observed, which is assigned to the C-C≡N bending vibration of acetonitrile. In addition, two additional signals at 185 and 260 cm$^{-1}$ are discerned at probe wavelengths of 600 and 610 nm. h) A comparison of the vibrational spectra obtained in solution and solid state allows for the assignment of the signal at 205 cm$^{-1}$ to an intramolecular mode. This is reinforced by a quantum chemical modelling of the TAPP-Br monomer.[155] The calculations further suggest the modes at 110 and 140 cm$^{-1}$ be of intramolecular origin, whereas the two remaining vibrational modes (20 and 126 cm$^{-1}$) are only active in the solid state and hence correspond to intermolecular modes. Reprinted with permission from ref. 155. Copyright © 2020, American Chemical Society.*

In order to further elucidate the origin of vibrational modes, a comparison with Raman frequencies for a TAPP-Br monomer obtained by quantum chemical calculations is made (Figure 4.9h).[155] Here, major contributions at 110, 140, and 205 cm$^{-1}$ are observed, which coincide with the experimental spectrum. Consequently, these modes are assigned to be of intramolecular origin. In contrast, the calculated frequencies of 40 and 90 cm$^{-1}$ do not directly match with an experimentally observed frequency.

However, as the former (40 $cm^{-1}$) is only located 12 $cm^{-1}$ below an intense signal in the experimental spectrum, they are assumed to represent the same vibrational mode. The 90 $cm^{-1}$ mode though is in a region with a distinct lack of experimental signal intensity. Consequently, the most probable explanation is that this mode is inhibited in solid state due to the rigid orientation of chromophores in the molecular crystal. Further differences between experimental and calculated spectra are found at 20 and 126 $cm^{-1}$, for which no counterpart is observed in the modelled spectrum. This indicates that the origin of both modes are inter-chromophore interactions. In total, of the five major contributions to the vibrational coherence observed in thin films of TAPP-Br, three are assigned to intramolecular modes (50, 140, and 205 $cm^{-1}$). The two remaining vibrational modes (20 and 126 $cm^{-1}$) are only active in the solid state and hence correspond to intermolecular modes.

### 4.2.4 Identification of Electronic Species and Kinetic Model

*Initial Superposition of Singlet and Triplet Spectral Features.*

In the following, the electronic species involved in the dynamics are unveiled. For this, the transient spectra obtained in thin film are compared to the results obtained in dilute solution (*vide supra*). For early probe delays, the latter exhibits a single broad ESA band assigned to $S_1$, which is located in the red part of the probe spectrum. The same observation is made in solid state. However, an additional blue-shifted ESA is observed simultaneously. Intriguingly, its spectral location coincides with the $T_1$ ESA identified in solution. This becomes even more apparent when comparing the transient spectra, corrected for the negative signal contributions of GSB and SE, with the corresponding corrected $S_1$ and $T_1$ SADS (Figure 4.10): Especially for TAPP-Br, the blue-shifted features are identical except for a slight blue-shift of 150 meV in solid state. Thus, the spectral features of the early transient spectra are attributed to a combination of singlet and triplet ESA. Analogous to solution measurements, the former is assigned to the first excited singlet state. As both spectral features are present at earliest probe delays, they have to be formed either coherently upon photoexcitation or faster than the temporal resolution of the setup, *i.e.*, with a time constant below

90 fs. For the singlet species, this is not unexpected as it represents the product spin-allowed photoexcitation of the ground state. In contrast, as shown by previous measurements, the formation of a triplet state *via* ISC occurs on the nanosecond timescale. This process is not expected to accelerate by several orders of magnitude in solid state and, consequently, the triplet ESA does not originate from $T_1$ generated by an intramolecular process. In turn, the observations point towards the ultrafast formation of a correlated triplet pair state, denoted as $^1(TT)$. This assignment is in agreement with previous reports for coherent $^1(TT)$ formation in hexacene,[44] rubrene,[45-46] and TIPS-Pn derivatives *via* SF.[41-42] Most notably, ultrafast SF on the sub-200 fs timescale has been observed for polycrystalline thin films of a perylene diimide derivative.[43] This molecule is structurally similar to TAPP-Br, as both aromatic systems share the perylene motif. In addition, perylene diimides typically exhibit the same slip-stacked crystal structure[116, 163] also observed for TAPPs.[117, 137-138] The possible presence of an ultrafast SF process is further evaluated using computed values for the energy levels of $S_1$ and $T_1$ of TAPP-Cl and TAPP-Br monomers.[155] A comparison of the vertical excitation energy of $S_1$ with two times the $T_1$ excitation energy formally results in an excess energy of 240 and 160 meV for TAPP-Cl and TAPP-Br, respectively.

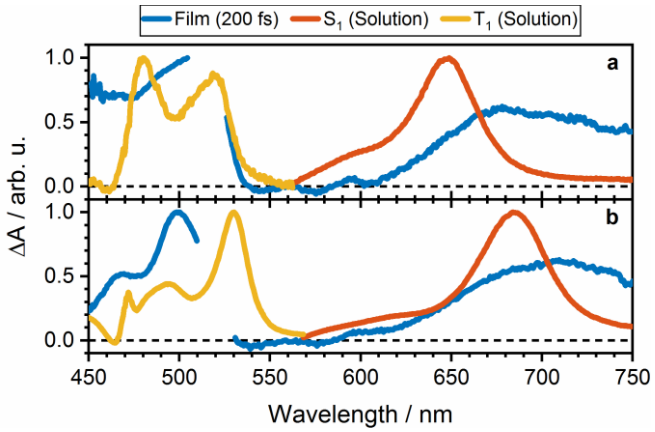


***Figure 4.10:*** *Transient spectra at earliest probe delays of a) TAPP-Cl and b) TAPP-Br exhibit a striking similarity with the respective corrected $S_1$ and $T_1$ SADS. This indicates the presence of a singlet and triplet species immediately upon photoexcitation. As ISC is unlikely to be accelerated by several orders of magnitude, the triplet species in thin films is assigned to a coherently formed $^1(TT)$, generated via an ultrafast SF process. Reprinted with permission from ref. 155. Copyright © 2020, American Chemical Society.*

However, this calculation does not consider the stabilisation due to π-π-stacking (Figure 4.5, page 68), which is typically stronger for the excited singlet.[164] The lowering of the $S_1$ energy level strongly influences SF and has in fact been identified as the main reason for the absence of efficient SF in peropyrene and its 2,9-disubstituted counterparts.[23-24] In order to account for the expected stabilisation, the shift between the absorption maximum in solution and thin film is considered. As this directly relates to the $S_0 - S_1$ excitation, the energy difference is subtracted from the calculated SF energy balance. Consequently, a slightly exothermic SF process (15 meV) is expected for TAPP-Cl. In contrast, TAPP-Br exhibits an endothermic energy balance of 74 meV. However, given that a possible stabilisation of $T_1$ is neglected, this result corresponds to a "worst case". In addition, a coherent formation of a triplet pair state has been observed in TIPS-Tn, which exhibits a negative energy balance for SF.[47, 86] Thus, a slight endothermicity does not contradict an ultrafast triplet formation in TAPP-Br. In conclusion, the transient spectrum at earlies probe delays is assigned to a combination of spectral features originating from $S_1$ and $^1(TT)$. Given that the latter depicts a triplet pair located on two neighbouring chromophores, the excited singlet state will be referred to as $S_1S_0$ to allow for a formally correct treatment and to account for the delocalisation of the excitation.

*Singlet-Singlet Annihilation.*

Both ESA bands exhibit a significant loss of signal intensity within the first 5 ps with the corresponding time constant $\tau_1$ (Table 4-4). In principle, this could be explained by an independent decay of the respective populations. However, as the TA data was analysed globally, this necessitates the unlikely assumption of both processes coincidentally having an identical time constant for both processes. Thus, $S_1S_0$ and $^1(TT)$ can be viewed as being interlinked. This connection can either be rationalised by a superposition of singlet and triplet wavefunctions or a rapid interconversion of both species, which cannot be discerned with the given experimental setup.[29] For either of both possibilities, the sharp and homogeneous drop in signal intensity implies a relaxation of a part of excited state population to the ground state, which directly

affects both spectral features. In accordance with previous reports as well as the observed acceleration of the signal decay with increasing excitation intensities (see appendix section C.4), the underlying process is assigned to singlet-singlet-annihilation (SSA).[23, 116] Intriguingly, the SE signal in the spectral region around 610 and 615 nm for TAPP-Cl and TAPP-Br, respectively, retains more of its intensity compared to lower wavelengths. This is corroborated by the emission decay, for which the red-shifted wavelengths exhibit a long-lived component, whereas a decay within the IRF is observed at the blue edge of the respective emission spectrum (Figure 4.6). In accordance with observations for the structurally similar peropyrene[23] and perylene diimides, [51, 165] this spectral feature is assigned to an excimer. Excimer states have been shown to originate from a recombination of the triplet pair, *i.e.*, triplet fusion.[166] Furthermore, they are discussed to be generated competitively to the triplet pair and act as a trap state, hindering efficient SF due to their energetic stabilisation.[51, 70, 165] The present results seem to agree with the latter, as the intensity of its emission correlates with the intensity of the triplet signal in TA. In addition, due to the almost isoenergetic energy balance, the expected energetic stabilisation accompanying the excimer formation results in an unfavourable shift of energy levels for SF. Thus, excimer formation can be viewed as a competing reaction channel to SF in TAPPs. While the presence of this excimer can be established confidently, open questions remain with regard to its formation pathway. On the one hand, it is conceivable that the excimer is generated competitively to SSA and involves an excited singlet and a neighbouring ground state chromophore. On the other hand, excimer states could be generated as a product of SSA. However, experimental observations favour the first mechanism given the sharp drop in intensity. Finally, it is also possible that a combination of both pathways is observed.

*Identification of Triplet Pair Intermediates via Derivative Spectroscopy.*

In contrast to the initial homogeneous evolution of the ESA features, $\tau_2$ characterises the almost complete decay of the $S_1S_0$ signal while the triplet ESA retains its intensity. This suggests that the rapid interconversion between excited singlet and triplet pair is suspended. Hence, this process is assigned to the electronic decorrelation of $^1(TT)$.

The loss of singlet intensity suggests that upon decorrelation, the triplet manifold is populated almost exclusively. Possible products of the electronic decorrelation are either the spin-entangled ($T \cdots T$) or a pair of independent triplet states ($2\,T_1$). Both typically exhibit the same spectral features.[34] Thus, in order to gain further information on the present species, subsequent dynamics of the triplet signal in TAPP-Br are considered. Here, the triplet signal evolves with one addition time constant ($\tau_3$) in short-time TA measurements as well as two additional time constants on the nanosecond timescale ($\tau_4$, $\tau_5$). These complex dynamics are not expected for free triplet states, for which a relaxation to the ground state via either triplet-triplet-annihilation (TTA) or ISC would be expected.[29] Thus, the product of electronic decorrelation is assigned to the spin-entangled ($T \cdots T$). The subsequent evolution of the triplet signal exhibits a slight but notable narrowing of the ESA as well as a red-shift. This visibility of this effect is amplified by using derivative spectroscopy, which has the added benefit of discriminating the overlapping negative signal of the GSB. In this approach, transient spectra at selected probe delays are numerically derived with respect to the probe wavelength. Consequently, the maximum of an ESA band corresponds to a zero-crossing in its first derivative. In addition, the extrema of the first derivative correspond to the steepest gradient of the peak. Thus, the difference between the maximum and minimum of the derivative is used as an estimate for the peak width. Due to the low signal intensity in TAPP-Cl, this approach is only carried out for TAPP-Br (Figure 4.11). In addition, the spectral data was smoothed using a Savitsky-Golay filter in order to decrease the noise level of the data. Here, the maximum shifts from 497 nm at 1 ps probe delay to 501 nm at 7800 ps probe delay. The red-shift of the triplet ESA means that less energy is required for the probed transition. For the given case, the red-shift corresponds to a decrease of transition energy of ≈20 meV. This slight energetic shift is assigned to the spin-dephasing of ($T \cdots T$) and the corresponding loss of stabilisation due to the spin-pairing. This is corroborated by the narrowing of the ESA band from 100 meV at 1 ps probe delay to 60 meV at 7800 ps probe delay, which is attributed to an increased localisation of the excitation. Thus, the process characterised by $\tau_3$ is assigned to the spin-dephasing of ($T \cdots T$). The ensuing free triplets subsequently undergo a biexponential decay to the

ground state on the microsecond timescale. This is supported by the long-time dynamics, for which neither a red-shift nor a narrowing of the triplet signal is observed, indicating the presence of only one electronic state.

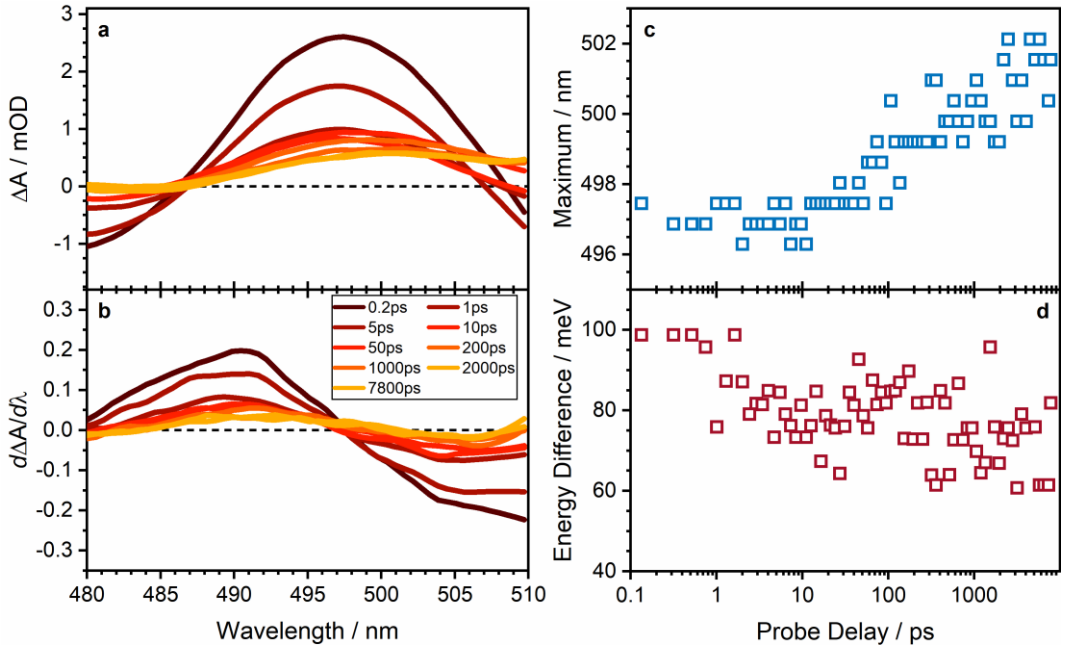


***Figure 4.11:*** *a) Smoothed transient spectra at selected probe delays and b) their derivative with regard to wavelength allow for an enhanced visibility of the observed red-shift and narrowing of the triplet ESA. c) The maximum intensity shifts from 497 nm at 1 ps probe delay to 501 nm at the end of the observed time window (7800 ps), corresponding to an energy of 20 meV. d) The spectral width of the signal is obtained as the difference in energy between the minimum and maximum of the derivative, which depict the steepest gradients of the peak. Here, a systematic narrowing from 100 meV at earliest probe delays to ≈60 meV at late probe delays can be discerned. Both observations point towards the spin dephasing of $(T \cdots T)$: The loss of stabilisation energy due to spin pairing results in the ESA requiring less energy, resulting in the red-shift. Simultaneously, the triplet excitation becomes more localised, resulting in less inter-chromophore interactions and hence the narrowing of the signal. Adapted with permission from ref. 155. Copyright © 2020, American Chemical Society.*

### 4.2.5 Discussion of the Kinetic Model

Based on the previous discussion, a kinetic model for the dynamics of TAPP-Br in thin films is put forward (Figure 4.12a). Upon photoexcitation, the mutually interlinked $S_1S_0$ and $^1(TT)$ are formed. They either exist in a rapidly equilibrium or as superimposed wavefunctions. An initial loss in signal intensity with the corresponding time constant $\tau_1$ is observed, which is assigned to SSA and excimer formation. The

excimer undergoes a radiative relaxation to the ground state, which is identified both in stationary emission and SE decay. Simultaneously, the electronic decorrelation of $^1(TT)$ is observed, characterised by $\tau_2$. After electronic decorrelation, the triplet pair remains as a spin-correlated $(T \cdots T)$. With the time constant $\tau_3$, the triplet pair separates into two individual triplets, which is accompanied by a red-shift and narrowing of the triplet ESA. The free triplets exhibit a biexponential relaxation on the microsecond timescale $(\tau_4, \tau_5)$.

*Population Dynamics.*

Despite the kinetic model being identified, it cannot be used straightforward to extract the SADS of the involved species. This is due to the competing formation of excimer and $(T \cdots T)$. While both species are generated with a specific time constant, only the sum of both is observed experimentally. Thus, without further information, an unambiguous identification of the respective SADS cannot be realised. However, applying a two- and three-step sequential to TAPP-Cl and TAPP-Br, respectively, results in SADS consisting of spectral features of both triplet pair and excimer (Figure 4.12b,c). For the first SADS, a significantly difference in relative amplitude of the $^1(TT)$ signal with regard to the red-shifted singlet transition is observed. For TAPP-Br, a value of 60% is obtained, in contrast to 30% for TAPP-Cl. While this could be a result of the oscillator strength of the corresponding ESA being weaker for TAPP-Cl, this effect is unlikely to account for the doubled intensity in TAPP-Br. Thus, it is concluded that a significantly higher population is in the triplet manifold for TAPP-Br. The implications of this result will be discussed at a later point. For both compounds, the second SADS corresponds to the same loss of triplet signal intensity of two thirds with no observed spectral changes. In turn, a strong contribution of the excimer signal at 610 and 615 nm is observed for TAPP-Cl and TAPP-Br, respectively. This further corroborates the generation of the excimer simultaneous to SSA.

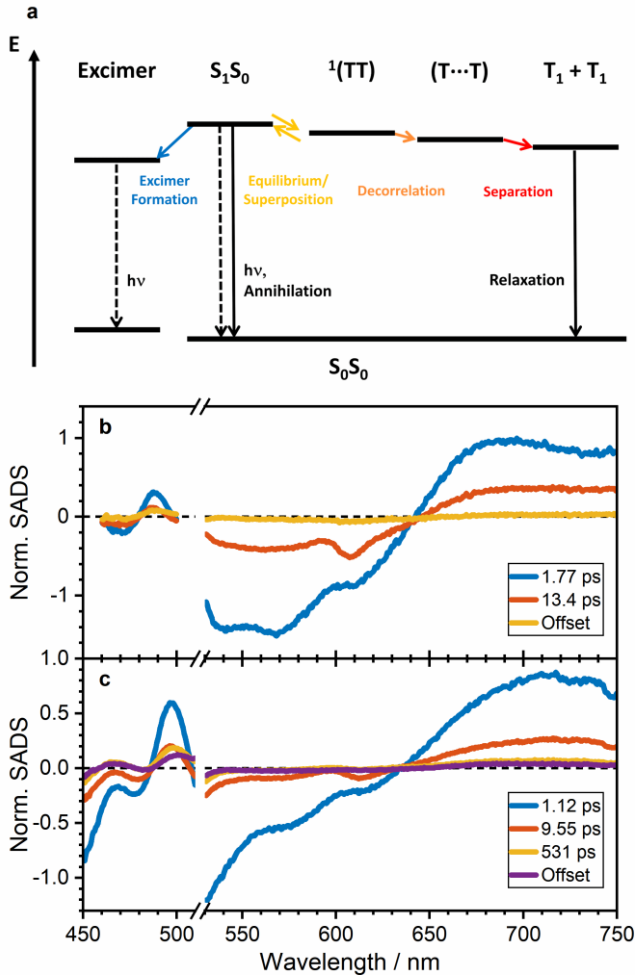


***Figure 4.12:*** *a) Kinetic model proposed for the dynamics of TAPP-Cl and TAPP-Br thin films. Upon photoexcitation, $S_1S_0$ and $^1(TT)$ are formed, interlinked either in a rapidly interconverting equilibrium or as a superposition of electronic states. Subsequently, competing SSA and excimer formation occur. The remaining $^1(TT)$ population exhibits electronic decorrelation to the spin-entangled $(T\cdots T)$. This is followed by spin-decorrelation and relaxation of the free triplets $T_1$ to the ground state. Due to the competing pathways, SADS of $^1(TT)$ and excimer cannot be disentangled without further knowledge about the individual time constants. Thus, a two and three-step sequential model is applied for b) TAPP-Cl and c) TAPP-Br, respectively, which allows for the discussion of characteristic spectral features. Most notably, the relative intensity of the triplet signal in the first SADS is twice as high for TAPP-Br (60%) than for TAPP-Cl (30%). This suggests a higher population of the triplet manifold for TAPP-Br. SSA and excimer formation reduces the intensity of $^1(TT)$ by two thirds for both compounds and the red-shifted excimer emission is clearly discerned in the SE. Subsequent SADS show the decay of the singlet signal and the decorrelation of the triplet pair. Reprinted with permission from ref. 155. Copyright © 2020, American Chemical Society.*

Additionally, the excimer signal is significantly stronger in TAPP-Cl compared to TAPP-Br, which is in accordance with the intensities observed in steady-state emission. The subsequent spectra, *i.e.*, the offset for TAPP-Cl and the third SADS for

TAPP-Br, exhibit the previously discussed slight redshift and narrowing of the triplet signal. In turn, the SE as well as the red-shifted ESA vanish almost completely. The only remaining negative contribution is observed for the excimer emission. This is in agreement with the decorrelation of the triplet pair, resulting in the population moving almost completely to the triplet manifold. For TAPP-Br, the effect of the spin-dephasing of $(T \cdots T)$ is represented in the offset. Here, the red-shift can be clearly discerned, which originates from the localisation of the triplet excitations.

The overlapping spectral features in the SADS hinder the determination of the overall triplet yield. Typically, this is achieved by comparing the amplitudes of the SADS of triplet pair states and free triplets.[21, 29] Here, assuming the same extinction coefficient for both species, the SADS of the latter is expected to be halved for quantitative SF. In the case of TAPP-Cl and TAPP-Br thin films, however, the spectral features of the triplet overlap with the GSB and as such are strongly influenced by the dynamics of singlet and excimer states. Consequently, a comparison of the triplet amplitudes would introduce an unknown error as the GSB exhibits an evolution on the same timescale as electronic decorrelation. Nonetheless, while the triplet yield cannot be determined quantitatively, the formation of free triplet states has been demonstrated. In addition, a qualitative comparison implies higher triplet yields for TAPP-Br compared to TAPP-Cl.

*Vibrational Dynamics.*

Having identified the kinetic model, the vibrational modes observed in TAPP-Br are to be assigned to the individual electronic states. Typical parameters to assign Raman modes to a ground or excited potential surface include the spectral dependence, dephasing times, frequencies and/or the phase of the oscillatory features.[167] As shown by the fit of the transients (*vide supra*), all oscillations have their highest activities at early probe delays. Thus, they have to originate from an electronic state present at earliest probe delays, *i.e.*, $S_1S_0$ or $^1(TT)$. In addition, IVS measurements in solution allows for the assignment of the modes at 50, 140 and 205 $cm^{-1}$ to intramolecular modes, whereas the modes at 20 and 126 $cm^{-1}$ correspond to intermolecular vibrations. The intramolecular modes show an experimentally observed dephasing time (<2 ps)

within the decorrelation time of $^1(TT)$ (9.55 ps). However, given their high activities in spectral regions which coincide with ground-state absorption as well as singlet and triplet ESA bands no unambiguous assignment can be made. This is supported by the variation in the phase of individual vibrational modes, which suggest that they do not originate from a single potential surface. However, the frequency range in which intramolecular modes are detected has been connected to the coherent formation of $^1(TT)$.[34, 44, 46-47, 65-66, 68-69] A notable example is tetracene, for which vibronic coupling including a low-frequency mode results in efficient SF despite an endothermic energy balance.[47] The intermolecular modes exhibit the same general behaviour as their intramolecular counterparts. Thus, they cannot be assigned to a single electronic state as well. In literature, intermolecular vibrations have been shown to be a key requirement for SF.[46] Here, the packing motif in a molecular crystal of rubrene leads to a vanishingly small coupling between $S_1S_0$ and $^1(TT)$. However, low-frequency lattice vibrations allow for a vibronic coupling of both states and accordingly SF. Given the examples from literature, it is assumed that intra- and intermolecular modes observed in TAPP-Cl and TAPP-Br play a similar crucial part in the coherent formation of $^1(TT)$. Nonetheless, in order to doubtlessly prove this assumption, more complex experiments are required which are sensitive exclusively to the excited state potential surface.[64]

### 4.2.6 Conclusion

In conclusion, TAPPs have been identified as suitable SF chromophores. The ultrafast triplet generation in thin films of TAPP-Cl and TAPP-Br contrasts reports on their formal parent compound, peropyrene,[23-24] suggesting a more favourable energetic landscape. This proves the merit of aza-substitution of aromatic backbone with regard to SF, as previously observed for aza-pentacenes as well as phenazinothiadiazoles.[15-16, 21, 29]

In both TAPP-Cl and TAPP-Br, a formation of superimposed $S_1S_0$ and $^1(TT)$ is observed within the experimental resolution. Subsequently, a reduction of the excited

state population due to SSA occurs. The remaining $^1(TT)$ population undergoes electronic dephasing to $(T \cdots T)$, followed by spin thermalization. Intriguingly, the triplet signal is more intense in TAPP-Br despite its higher $\Delta E_{SF}$ compared to TAPP-Cl. Based on the experimental findings, three explanations present themselves.

First, the dephasing of $^1(TT)$ competes with excimer formation, which is more pronounced in TAPP-Cl compared to TAPP-Br. While it has been shown that SF may occur *via* an excimer intermediate in terrylene-diimide,[53] it can be concluded that in the present case, the stabilisation of the excimer effectively inhibits SF. The enhanced excimer formation in TAPP-Cl may originate from increased CT contributions, as observed in other rylene-based chromophores.[166, 168]

Second, periodic oscillations in the transients of both compounds unveils the presence of intermolecular, low-frequency vibrational modes, which correlate with the triplet signal intensity. On the one hand, this relation can be explained by an enhanced coupling to the phonon bath, which has been shown to aid in the decorrelation of $^1(TT)$.[36] On the other hand, it may originate from morphological effects, *i.e.*, the higher long-range order observed for the TAPP-Br thin film.[155]

Finally, the halide substituent itself is considered. As demonstrated in section 4.1, a strong effect on triplet dynamics is expected due to the heavy-atom effect. In addition, spin-orbit coupling has previously been shown to aid in the decorrelation of $^1(TT)$,[131] implying a decrease of the energy of $^5(TT)$. In consequence, the binding energy of the correlated triplet pair would be reduced.

# 5 Diffusion-Controlled Singlet Fission in Solution

As demonstrated in the previous chapter, the close proximity of chromophores in solid state allows for the formation of triplet pairs on the sub-100 fs timescale. However, it has also become apparent that aggregation effects impair SF energetics. In addition, SSA and excimer formation constitute major loss channels. These issues are addressed in solution-based SF. Given a high solubility of the chromophore, aggregation is absent, and the decreased density of excited states effectively eliminates SSA. The role of an excimer as a SF intermediate is subject of ongoing discussion and will be addressed in the following chapter.[25-27, 70]

A further benefit of measurements in solution is the easy control of reactants and their concentrations in solutions allows for a flexible variation of the reaction system. This is demonstrated in the first section of this chapter, where the influence of oxygen on chromophore dynamics is investigated. The photophysical effects of molecular oxygen have first been described in the context of fluorescence quenching[169] with the underlying mechanism being the sensitization of the triplet ground state ($^3O_2$) to a singlet oxygen species ($^1O_2$) by the initially excited chromophore.[170-171] This interaction has since been specifically used to generate $^1O_2$.[13-14] Due to its high reactivity, $^1O_2$ undergoes a variety of photophysical and –chemical reactions,[13-14] with a notable example being its cycloaddition to acenes.[105, 172-173] Given that the concentration of oxygen in organic solvents usually amounts to 1 to 3 mM,[174-176] its effects are expected to be most pronounced at similar chromophore concentrations. TIPS-Pentacene (TIPS-Pn, Figure 5.1) is chosen as chromophore as the availability of studies involving it allows for experimental observations to be readily compared to reported observations. The experiments are repeated with TIPS-Tetracene (TIPS-Tn) and $TDCl_4$ (Figure 5.1) to establish general characteristics of observed interactions.

In the second part, effects of the variation of chromophore concentration are investigated. Given that a high concentration increases the probability of inter-chromophore interactions, this allows for direct SF to occur efficiently.[25-27] While in previous reports, an excimer intermediate has been identified, these observations were

exclusively made for hydrocarbon acene-based chromophores. Thus, $TDCl_4$ is investigated, for which SF has been established in solid state.[21] The inclusion of a chromophore with heteroatoms may yield insights on SF intermediates in solutions and the binding energy of ${}^1(TT)$.

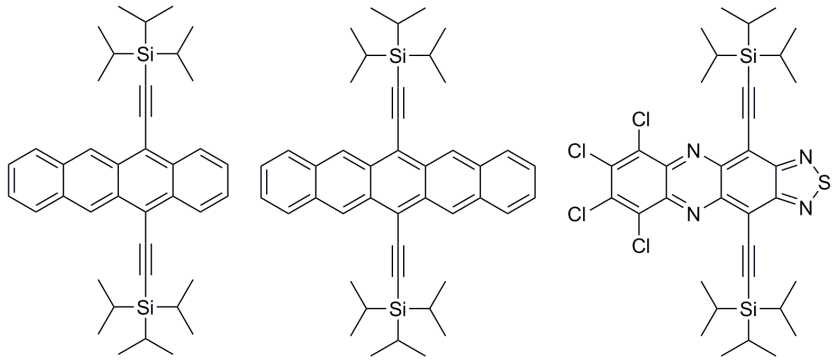


***Figure 5.1:*** *Molecular structures of acene-based chromophores investigated with regard to their SF dynamics in solution.*

## 5.1 Oxygen-Catalysed Triplet Formation in Acenes

### 5.1.1 Concentration Dependence of Stationary Spectra

The stationary absorption spectrum of TIPSPn in THF shows an absorption maximum at 640 nm (Figure 5.2a). Three additional vibronic peaks are identified at 590, 548 and 510 nm, corresponding to a separation of ≈165 meV. An additional, weak absorption band is detected at 439 nm, which also exhibits a vibronic peak at 415 nm, mirroring the separation of the main absorption band. Varying the concentration in a range of 0.01 to 100 mM shows a slight drop in relative intensity of the absorption maximum. This is attributed to the absorption exceeding the dynamic range of the spectrometer due to the high concentrations combined with a high extinction coefficient. The latter is determined to be $\epsilon_{570\mathrm{nm}}$ = (2.22 ± 0.03) $10^4$ l (mol cm)$^{-1}$ at the second vibronic peak of the absorption maximum (570 nm). In contrast to the consistent shape of the steady-state absorption, the emission band exhibits a spectral change with increasing concentration. In dilute solutions (0.01 mM), the emission spectrum mirrors the vibronic structure of the absorption spectrum with two peaks at 648 and 704 nm. Upon increasing the concentration two characteristics change significantly. First, an overall decrease in emission intensity is observed. This points towards the presence of a reaction pathway in concentrated solutions, which competes with the radiative decay. This effect will be explored in detail in section 5.2. Second, the relative intensity of the peak at 648 nm with regard to 704 nm decreases gradually from 2.5 (0.01 mM) to 0.1 (100 mM). This spectral change originates from the small Stokes-shift, which results in a re-absorption of emitted photons. This effect can be modelled quantitatively using the previously determined extinction coefficient of TIPS-Pn. According to Lambert-Beer's law, the transmitted intensity $I_1$ is obtained as

$$I_1 = \frac{10^{\epsilon_\lambda \cdot c \cdot d}}{I_0} \qquad \text{Eq. 25}$$

with the wavelength dependent, molar extinction coefficient $\epsilon_\lambda$ (*vide supra*), concentration $c$, path length $d$ and initial intensity $I_0$. Using the experimental

parameters for a concentration of 50 mM and the emission spectrum obtained for dilute solution (0.01 mM) as $I_0$, the corresponding experimental emission spectrum is accurately reproduced (Figure 5.2b).

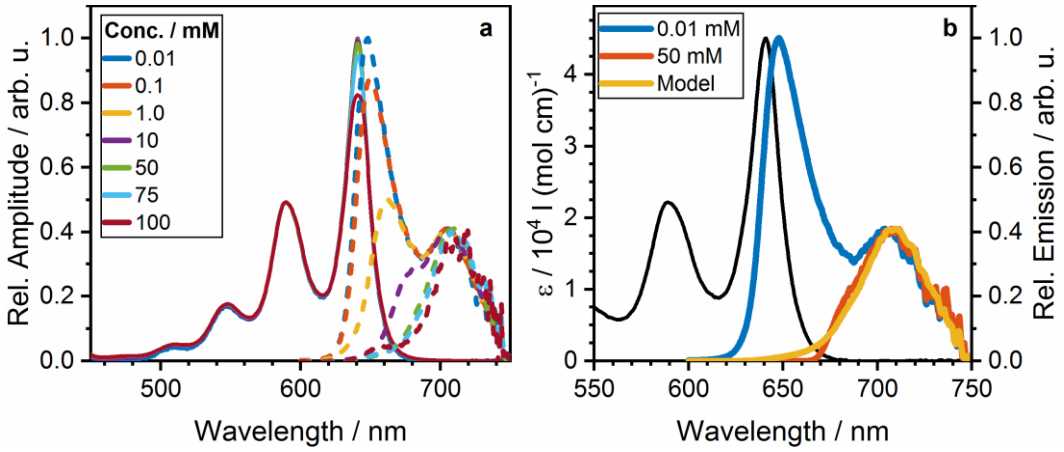


***Figure 5.2:*** *a) Concentration-dependent spectral changes of stationary absorption and emission spectra of TIPS-Pn, normalized at 590 and 720 nm, respectively. Stationary absorption spectra exhibit a relative decrease of the absorption maximum upon increasing the concentration. This is attributed to the absorption exceeding the dynamic range of the spectrometer. Otherwise, no spectral changes are observed. Stationary emission spectra in dilute solutions (0.01 mM) mirror the spectral shape of the corresponding absorption spectrum. In contrast, an overall decrease of emission intensity is observed (not shown) as well as a significant decrease of the relative intensity of the emission maximum. This observation originates from a re-absorption of emitted photons and can be modelled quantitatively as exemplified for a concentration of 50 mM in panel b. Reprinted with permission from ref. 104 under the terms of the Creative Commons CC BY license.*

### 5.1.2 Time-Resolved Spectroscopy Under Ambient and Oxygen-Free Conditions

In order to elucidate the dynamics of TIPS-Pn, long-time TA measurements were carried out, exemplified for a concentration of 0.5 mM under ambient conditions in Figure 5.3a. Directly upon photoexcitation, a structured ESA band is observed between 350 and 580 nm. Its most intense peak is located at 445 nm and weaker features are visible at 510, 530 and 570 nm. Furthermore, a negative signal is present between 350 and 680 nm, which is attributed to a combination of GSB and SE. At longer wavelengths, the red tail of the SE is overcompensated by a weak ESA. Within 50 ns, the signal decays while simultaneously undergoing a change in its spectral shape (Figure 5.3b). The emerging ESA possesses a maximum at 495 nm and a weaker signal

at 465 nm. The intensity of this spectrum increases until a probe delay of 400 µs before decaying homogeneously on the microsecond timescale.

Upon deaerating the solution, the observed dynamics change considerably, especially at later probe delays (Figure 5.3c and d). While the initial transient spectrum exhibits the same spectral features and amplitudes, the intensity of the emerging ESA band significantly lower. This is also apparent when analysing both datasets with a global multiexponential fit. In order to achieve a satisfactory fit, three exponential decays and an offset are necessary for ambient conditions, whereas one fewer exponential decay is used for the fit of the deaerated sample (appendix section D.1).

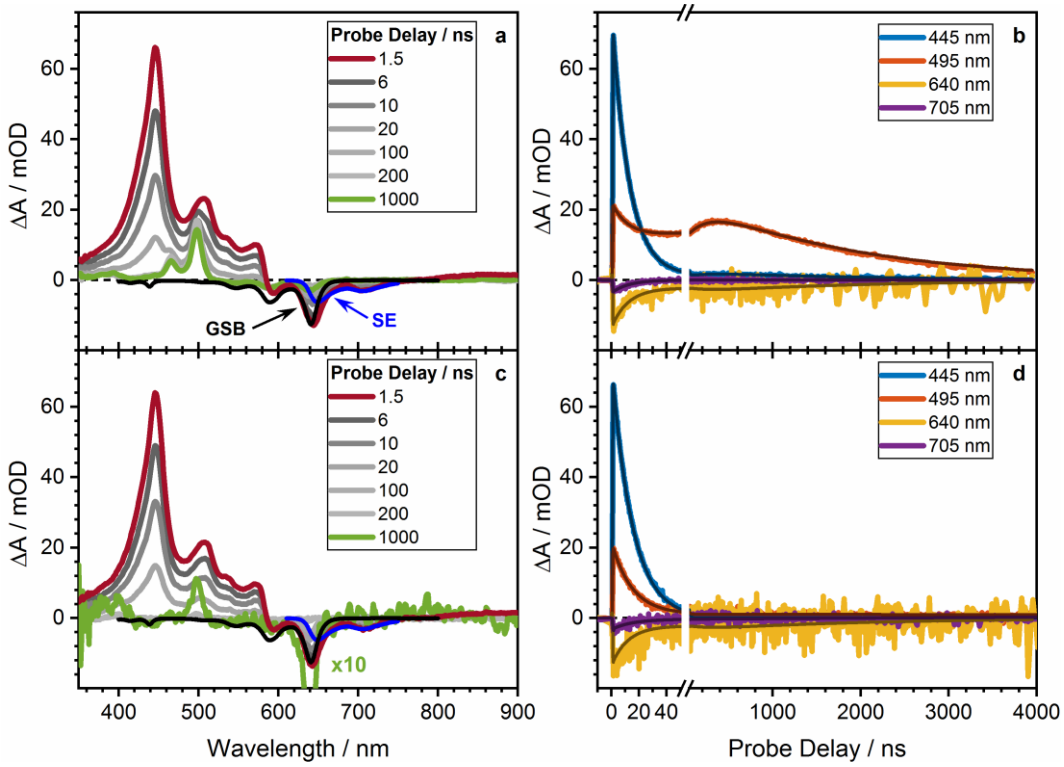


***Figure 5.3:*** *Comparison of TA results for 0.5 mM TIPS-Pn in THF under ambient conditions (a,b) and in a deaerated solution (c,d). The last transient spectrum in the deaerated solution is multiplied by 10 for enhanced visibility of its spectral features. Both measurements show an initial ESA band with its maximum at 445 nm as well as negative contributions of GSB and SE. Within 100 ns, ESA and SE decay while a second ESA band with its maximum at 495 nm emerges. The intensity of the emerging ESA is significantly stronger under ambient conditions. Furthermore, the transients unveil changes in the dynamics: Under ambient conditions, the second ESA increases until its maximum is reached at a probe delay of ≈400 ns. This feature is completely absent in deaerated solutions. Reprinted with permission from ref. 104 under the terms of the Creative Commons CC BY license.*

In both measurements, the first time constant $\tau_1$ relates to the decay of the initial spectrum. This time constant amounts to 12.3 ns under ambient conditions and a slightly higher 14.9 ns in the deaerated solution. The second time constant $\tau_2$ = 242 ns is only present in the former case and corresponds to an increase of the second ESA band. Finally, the last time constant $\tau_3$ is similar for ambient and deaerated conditions (1.88 and 2.83 µs, respectively). It is noted that although an additional time constant is required for the fit of the dataset obtained under ambient conditions, the transient spectra do not support the presence of an additional species compared to deaerated solution, as no additional spectral features are apparent.

### 5.1.3 Oxygen-Catalysed Singlet Fission

*Identification of Electronic Species.*

In order to accurately interpret the observed differences in the dynamics for ambient and deaerated conditions, the nature and amount of involved species have to be identified. As previously established, two identical sets of spectral features and consequently two different species are observed in both measurements. In accordance with previous reports,[26] the initial ESA which is present directly upon photoexcitation is assigned to $S_1$. Its decay is accompanied with the loss of SE, as corroborated by time-resolved emission measurements (see appendix section D.1). This suggest that $S_1$ is converted to a non-emissive species. Due to its lifetime on the microsecond timescale as well as striking similarities between the ESA and spectral features described in the literature,[26] the emerging species is assigned to $T_1$. While the same electronic species are present under ambient conditions and in deaerated solutions, more complex dynamics are observed in the former case. In order to account for these differences, possible reaction pathways of $S_1$ are considered. For the ensuing discussion, intra- and intermolecular mechanisms are discussed. Intramolecular reaction pathways include radiative (*i.e.* fluorescence) and non-radiative transitions to the ground state, as well as ISC to $T_1$. These channels follow unimolecular reaction kinetics and as such their respective rates are concentration independent. Hence, they can be assumed to be transferrable in between both measurements. Intermolecular

reactions require an additional molecule as reaction partner for the excited chromophore. Therefore, as solutes are dispersed homogeneously in the solvent, diffusion has to occur prior to any reaction.

In deaerated solutions, the only available reaction partner is another chromophore in the ground state. Consequently, an upper limit for the bimolecular diffusion rate can be estimated using the Einstein-Smoluchowski relation[177]

$$k_D = \frac{8RT}{3\eta} \qquad \text{Eq. 26}$$

with the ideal-gas constant $R$, temperature $T$ and solvent viscosity $\eta$. For the given experimental parameters,[178] this corresponds to $k_D = 1.36 \times 10^{10}$ M$^{-1}$ s$^{-1}$ or, considering the chromophore concentration of 0.5 mM, $\tau_D = (k_D \cdot c)^{-1} = 147$ ns. As the obtained value is an order of magnitude higher than the experimental time constant of 14.9 ns, inter-chromophore reactions represent a negligible fraction of singlet deactivation. Consequently, the observed triplets are predominantly formed *via* an intramolecular process, *i.e.* ISC. This is consistent with the low triplet signal intensity, given that ISC is a spin-forbidden process. Intriguingly, a faster singlet decay as well as a more intense triplet signal are observed under ambient conditions. Both results point towards an additional triplet formation process. In the following, the underlying mechanism will be drawn up and subsequently verified by experimental data.

*Oxygen-Mediated Triplet Formation in TIPS-Pn.*

As a starting point, the reactions of unsubstituted pentacene in aerated solutions are considered. As shown above, its UV/Vis spectrum readily degrades upon irradiation. This photodegradation has been reported to originate from the formation of an endoperoxide.[105] The reaction mechanism includes the sensitisation of molecular oxygen in its triplet ground state ($^3O_2$) by the photoexcited pentacene, resulting in the highly reactive singlet oxygen species ($^1O_2$). The latter subsequently reacts with pentacene to yield the aforementioned endoperoxide. In TIPS-Pn, however, the

formation of an endoperoxide is impeded by the stabilisation of the LUMO due to the alkynyl substitution.[106] Nonetheless, the sensitisation of $^3O_2$ cannot be ruled out *a priori*, as $S_1$ of TIPS-Pn is 1.94 eV above its ground state and as such is able to sensitise the $^3O_2 \rightarrow {}^1O_2$ transition (0.97 eV).[13, 104]

In addition, the low-lying $T_1$ of TIPS-Pn (0.85 eV)[104] allows for the excited chromophore to transfer only part of its energy to $^3O_2$:

$$S_1 + {}^3O_2 \rightarrow T_1 + {}^1O_2 \qquad \text{Eq. 27}$$

This reaction is exothermic by 0.19 eV and the overall spin multiplicity is conserved. As such, an efficient energy transfer is expected. This intermolecular triplet formation mechanism constitutes a competing deactivation pathway for $S_1$. Consequently, it accounts for the acceleration of the singlet decay under ambient conditions but does not explain the presence of the additional time constant corresponding to a delayed increase in triplet intensity. However, this can be rationalized by a subsequent reaction including $^1O_2$ and a ground state chromophore:

$$S_0 + {}^1O_2 \rightarrow T_1 + {}^3O_2 \qquad \text{Eq. 28}$$

Here, the reactive singlet oxygen sensitizes a ground state chromophore to $T_1$ with an excess energy of 0.13 eV. This reaction depicts the reaction of one excited and one ground state singlet yielding two triplet states, a key characteristic of SF. As the individual states are located on different moieties, this reaction is labelled heterogeneous SF. Both, the initial energy transfer as well as the subsequent heterogeneous SF, can be joined to obtain a two-step reaction model:

$$S_1 + S_0 + {}^3O_2 \xrightarrow{k_{ET}} T_1 + S_0 + {}^1O_2 \xrightarrow{k_{hSF}} T_1 + T_1 + {}^3O_2 \qquad \text{Eq. 29}$$

Hereof, two main results can be derived. First, oxygen is not consumed during the reaction but acts as a catalyst. Second, the initial reactants – one excited and one ground state chromophore – and the final products – two triplets – are equivalent to those of SF process. Consequently, both reaction steps combined represent a sequential SF process, with the rate constants $k_{ET}$ and $k_{hSF}$ for the individual steps (Figure 5.4).

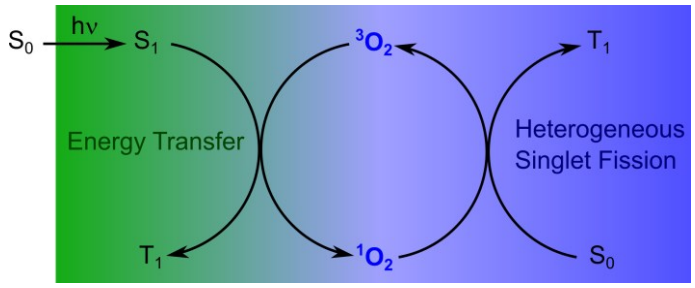


***Figure 5.4:*** *Postulated catalytic cycle for sequential SF. Upon photoexcitation, the excited chromophore ($S_1$) transfers part of its energy to molecular oxygen in its ground state ($^3O_2$), resulting in a triplet chromophore ($T_1$) and a reactive singlet oxygen species ($^1O_2$). In a second step, the latter undergoes heterogeneous SF with an additional ground state chromophore. This results in the catalyst, $^3O_2$, being reformed as well as a second triplet chromophore. Adapted with permission from ref. 104 under the terms of the Creative Commons CC BY license.*

*Effects of oxygen Concentration on Sequential Singlet Fission.*

In order to verify the mechanism, the bimolecular nature of both energy transfer as well as heterogeneous SF has to be considered. As such, they depend on the concentrations of the respective reactants. For the energy transfer, these are the excited chromophore and $^3O_2$. However, only a small fraction of the chromophores is photoexcited and consequently a pseudo-first order reaction with respect to $^3O_2$ is expected. Additionally, the energy transfer has to compete with other reaction pathways. Consequently, $k_{ET}$ will not be observable individually but manifest itself as changes in the experimentally obtained $k_1$, which is the sum of all singlet deactivation processes. For the subsequent reaction, heterogeneous SF, the concentration of $^1O_2$ will be significantly lower compared to its reaction partner, a ground state chromophore. Therefore, a pseudo-first order reaction rate is assumed as well, this time with respect to chromophore concentration. In conclusion, a linear dependence on concentration is expected for both steps, with the relevant dimension being $^3O_2$ concentration for energy transfer and the ground state chromophore concentration for

heterogeneous SF. In order to verify these assumptions, the effects of variations of oxygen and chromophore concentration on reaction kinetics are examined.

The most extreme case of variations of oxygen concentration is represented by the complete absence of it, *i.e.* a deaerated solution. Here, energy transfer is non-existent. Exemplified for a chromophore concentration of 0.5 mM, this results in the mean rate decreasing from $k_1 = (81.1 \pm 0.6) \times 10^6$ s$^{-1}$ to $k_1^{deaer.} = (67.1 \pm 0.5) \times 10^6$ s$^{-1}$. Considering the concentration of dissolved oxygen,[176] the difference between both rates corresponds to a bimolecular rate constant of $k_{ET} = (0.78 \pm 0.04) \times 10^{10}$ (Ms)$^{-1}$. While this rate is lower than the reported diffusion rate of oxygen of $3.12 \times 10^{10}$ (M s)$^{-1}$,[170] the latter represents an upper limit for a quantitative reaction. Therefore, the similarity of both rates leads to the conclusion that energy transfer and thus the formation of $^1O_2$ is the additional reaction pathway responsible for the faster singlet deactivation under ambient conditions. As this first step is a prerequisite for heterogeneous SF to occur, $k_{hSF}$ cannot be observed in deaerated solutions. In turn, the triplet decay ($k_3$) is monitored for both measurements. Upon deaerating the solution, it decreases from $0.53 \pm 0.03$ to $(0.35 \pm 0.06) \times 10^6$ s$^{-1}$, which will be discussed later.

In a corroborating measurement, a 1.5 mM solution was enriched with oxygen by bubbling through pure $O_2$ (Figure 5.5a,b). Compared to the same sample under ambient conditions, the maximum of the $T_1$ signal is reached at earlier probe delays (95 ns versus 144 ns, respectively) and is more intense by a factor of 1.59 (Figure 5.5c). In addition, an increase of $k_1$ from $(85.6 \pm 0.1) \times 10^6$ s$^{-1}$ to $(120 \pm 1) \times 10^6$ s$^{-1}$ is observed. As the remaining experimental parameters are kept constant, the higher rate has to be linked to an acceleration of the energy transfer due to increased oxygen concentration. Furthermore, the second rate constant $k_2$ remains constant at $19.5 \pm 0.5$ and $(20.3 \pm 0.4) \times 10^6$ s$^{-1}$ for ambient and oxygen-enriched conditions, respectively. This is in accordance with the proposed mechanism, which predicts a dependence of $k_2$ on chromophore concentration only. The last difference observed for oxygen-enriched solution is the significant increase of the decay rate of the triplet signal, $k_3$, from $0.74 \pm 0.01$ to $(1.92 \pm 0.04) \times 10^6$ s$^{-1}$.

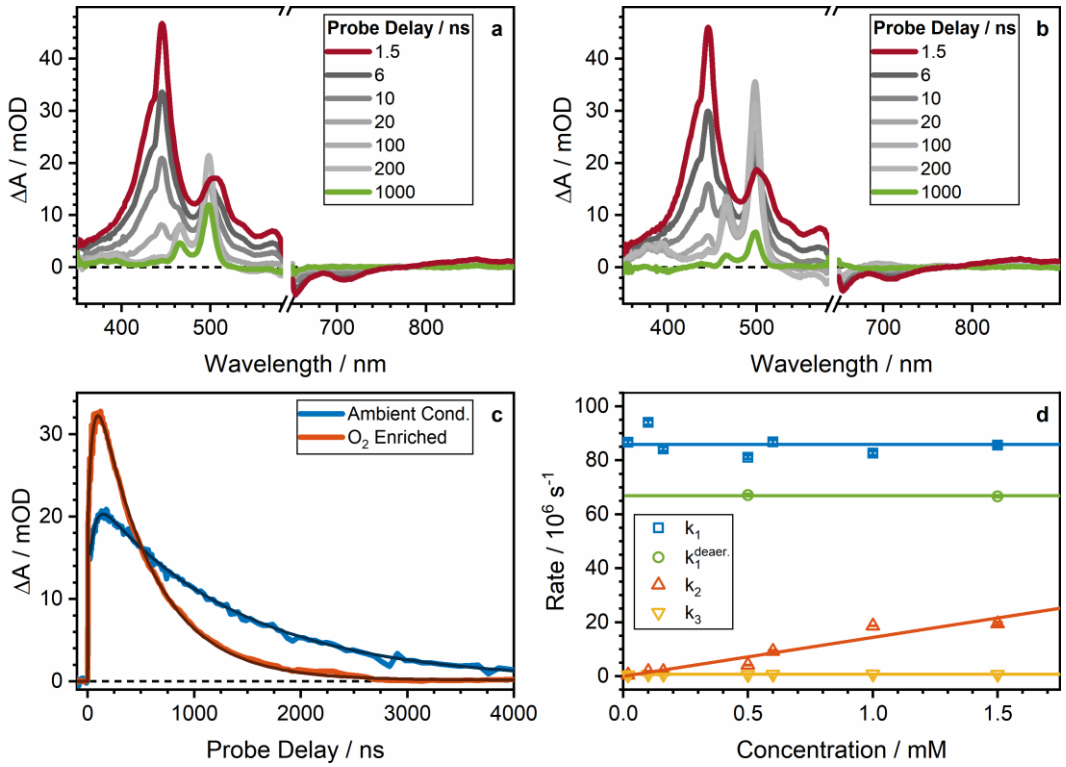


***Figure 5.5:*** *Transient spectra of 1.5 mM TIPS-Pn (a) under ambient conditions and (b) upon bubbling oxygen through the solution show a significantly higher amplitude for higher oxygen concentrations. c) The transients at a probe wavelength of 495 nm show that the maximum of the $T_1$ signal is reached at earlier probe delays and that it decays faster for the oxygen-enriched sample. The latter is attributed to the paramagnetic $^3O_2$ species facilitating relaxation via ISC. d) The variation of chromophore concentration between 20 µM and 1.5 mM has no effect on $k_1$, $k_1^{deaer.}$ and $k_3$ for which mean values of $k_1$=(85.7 ± 4.0)×10$^6$ s$^{-1}$, $k_1^{deaer.}$=(66.9 ± 0.3)×10$^6$ s$^{-1}$ and $k_3$=(0.64 ± 0.11)×10$^6$ s$^{-1}$ are obtained. In turn, $k_2$ increases linearly for higher concentrations. This behaviour is in agreement with the proposed pseudo-first reaction order of heterogeneous SF. Adapted with permission from ref. 104 under the terms of the Creative Commons CC BY license.*

This continues the trend observed between oxygen-free and ambient conditions (*vide supra*): A higher oxygen concentration results in a faster triplet decay. This effect can be rationalized by the paramagnetic nature of ground-state molecular oxygen ($^3O_2$), which facilitates the spin-forbidden relaxation of $T_1$ to the ground state *via* ISC.[14] In order to evaluate the influence of chromophore concentration on rate constants, a range of 20 µM to 1.5 mM was examined. According to Eq. 26, this concentration regime is devoid of a significant amount of inter-chromophore reactions. In accordance with the proposed mechanism, $k_1$ remains constant over the whole concentration range with a mean value of $k_1 = (85.7 \pm 4.0) \times 10^6$ s$^{-1}$ and $k_1^{deaer.} = (66.9 \pm 0.3) \times 10^6$ s$^{-1}$ (Figure 5.5d). In contrast, $k_2$ shows a linear increase with chromophore concentration with a

bimolecular rate of (1.44 ± 0.19) × $10^{10}$ $M^{-1}$ $s^{-1}$. This is in agreement with the expected pseudo-first reaction order of heterogeneous SF and the diffusion rate of oxygen (*vide supra*). In conclusion, the presence of a sequential SF process has been established and the corresponding rate constants for energy transfer, $k_{ET}$ and heterogeneous SF, $k_{hSF} = k_2$, have been successfully extracted. With this in mind, rate laws for the $S_1$ and $T_1$ species can be formulated and analytically integrated to obtain their time-dependent concentrations (see appendix section D.2). This allows to formulate the coefficient matrix with which the respective SADS can be obtained (Figure 5.6, *cf.* section 3.3.3). For both species, a perfect overlap of the SADS over the whole concentration range is observed. This further supports the proposed mechanism for sequential SF, as the SADS represent the absorption spectrum of the excited species, which does not change when varying the concentration. An incorrect kinetic model would lead to changes in the spectral shape or amplitude, as observed for a simple two-step sequential model (see appendix section D.2).

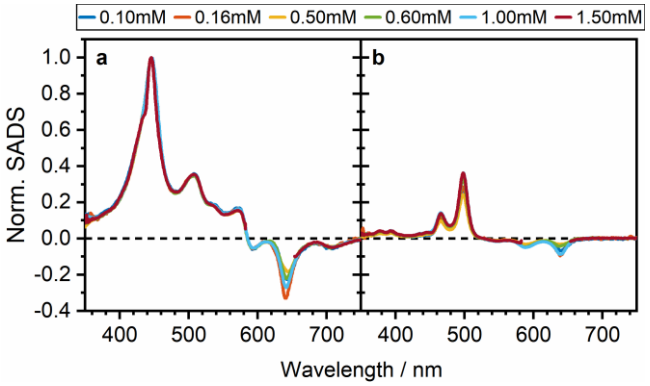


***Figure 5.6:*** *a) $S_1$ and b) $T_1$ SADS obtained by matrix algebra using the coefficient matrix obtained by integrating the rate laws for sequential SF, normalized for the maximum of the $S_1$ SADS. For both species, the spectra overlap perfectly within the investigated concentration range. This further supports the validity of the proposed mechanism.*

### *Oxygen-mediated triplet formation in TIPS-Tn*

In contrast to TIPS-Pn, the energy levels of its shorter acene homologue, TIPS-Tn, does not allow for a sequential SF process. While the $S_1 - T_1$ energy gap (1.03 eV)[21] is sufficient to sensitize $^3O_2$, the high $T_1$ energy (1.40 eV)[21] hinders heterogeneous SF. This effect can be seen by comparing TA measurements of 0.8 mM TIPS-Tn in deaerated solvent and under ambient conditions (Figure 5.7). In both cases, an initially

formed $S_1$ ESA with peaks at 415 and 470 nm is observed. Within 50 ns, this ESA decays and a weak $T_1$ ESA with its maximum centred at 510 nm is formed.[25, 104] Under ambient conditions, this signal decays completely within 4 µs whereas it remains as a constant offset in a deaerated solution. A global biexponential fit shows a slight acceleration of the singlet decay from 13.3 ± 0.1 ns (deaerated) to 10.8 ±0.1 ns (ambient, Figure 5.7c), corresponding an increase of the reaction rate by 1.72 $10^7$ $s^{-1}$. The acceleration of the singlet decay for ambient conditions is in accordance with the diffusion rate of molecular oxygen (*vide supra*). This indicates that the excited TIPS-Tn chromophore undergoes the same energy transfer process observed in TIPS-Pn.

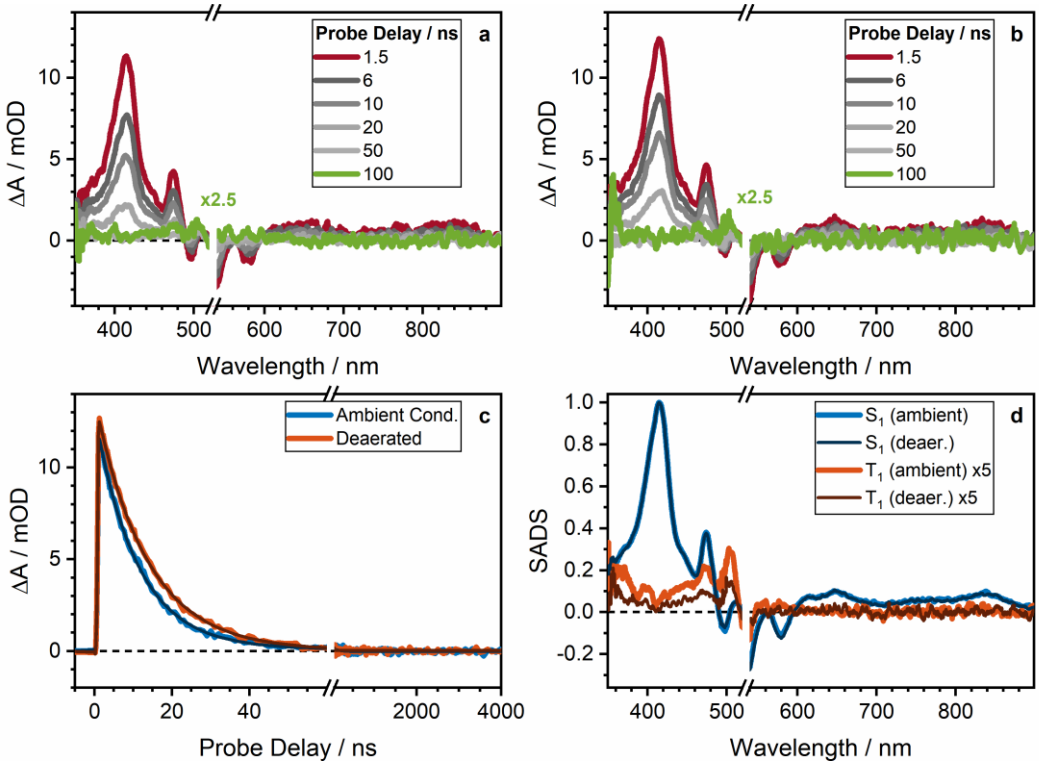


***Figure 5.7:*** *Transient spectra of 0.8 mM TIPS-Tn (a) under ambient conditions and (b) in a deaerated solution. In both cases, a transition of the initial $S_1$ to $T_1$ is observed within 50 ns. c) The transients at the maximum of the $S_1$ ESA (415 nm) show a faster decay rate under ambient conditions. The difference in rates is in agreement with the diffusion rate of oxygen, indicating an energy transfer from $S_1$ to $^3O_2$. d) $S_1$ and $T_1$ SADS for ambient and deaerated conditions, obtained by applying a sequential kinetic model. The spectra are normalized for the maximum of the $S_1$ SADS and $T_1$ SADS are multiplied by a factor of 5 to enhance visibility. While the spectral shape of both species remains identical for both measurements, the maximum of the $T_1$ SADS is twice as high under ambient conditions. This is attributed to the additional triplet formation by energy transfer to oxygen.*

In addition, the triplet signal decays with a time constant of 169 ± 6 ns under ambient conditions, while it remains as a non-decaying offset in deaerated solution. In contrast to TIPS-Pn, neither measurement shows a delayed increase of the triplet signal, which is characteristic for sequential SF. For both measurements, a sequential model was applied to obtain the SADS of the respective $S_1$ and $T_1$ (Figure 5.7d). Both species show an identical spectral shape, regardless of oxygen concentration. However, the relative intensity of the $T_1$ with regard to the $S_1$ SADS is twice as high under ambient conditions. This corresponds to the additional population of the triplet *via* the previously established energy transfer to $^3O_2$. Furthermore, the difference in $T_1$ decay shows that the oxygen concentration has an even stronger impact on triplet relaxation dynamics compared to TIPS-Pn. This is attributed to the energy of $T_1$, which – in contrast to TIPS-Pn – is able to sensitize the $^3O_2 \rightarrow {}^1O_2$ transition.

## 5.2 Competing Sequential and Direct Singlet Fission in $TDCl_4$

In the following, the validity of sequential SF is transferred from a pure hydrocarbon backbone to $TDCl_4$. This molecule has been shown to undergo SF in thin films.[21] In addition, quantum chemical calculations[21] predict both steps of sequential SF, *i.e.* energy transfer and heterogeneous SF, to be exothermic by 30 and 80 meV, respectively. Initially, concentration dependent changes in stationary absorption and emission spectra are discussed. This is followed by a thorough analysis of short and long-time TA measurements for a concentrated sample of $TDCl_4$ in toluene in order to identify spectral signatures of electronic species. Subsequently, concentration dependent changes in kinetics are investigated, whereby a broad concentration range from 0.1 to 115 mM is explored. In combination with previous results, this allows for a generalization of triplet formation processes in solution.

### 5.2.1 Proof of Sequential Singlet Fission in $TDCl_4$

*Concentration Effect on Stationary Spectra.*

The stationary absorption spectrum of $TDCl_4$ shows two strong absorption bands located at 425 and 670 nm, respectively (Figure 5.8a). The latter shows three pronounced vibronic peaks at 670, 620 and 580 nm, corresponding to a separation of ≈145 meV. In turn, the blue-shifted absorption feature possesses a maximum at 425 nm and a shoulder at 380 nm. A molar extinction coefficient of $\varepsilon_{670} = 16773\ M^{-1}\ cm^{-1}$ was determined at 670 nm. The spectra show no spectral changes in a concentration range from 0.11 to 115 mM (Figure 5.8a inset). Thus, aggregation or self-interaction effects can be excluded. In turn, the stationary emission spectra exhibit a concentration dependence. In dilute solution (0.74 and 1.47 mM), a single broad, unstructured emission band with its maximum located at 730 nm is observed (Figure 5.8b). Upon increasing the concentration, emission quenching is observed with a concomitant change of the spectral shape, i.e. a red-shift of the maximum and the appearance of a local minimum at 720 nm. Both effects will be discussed at a later point.

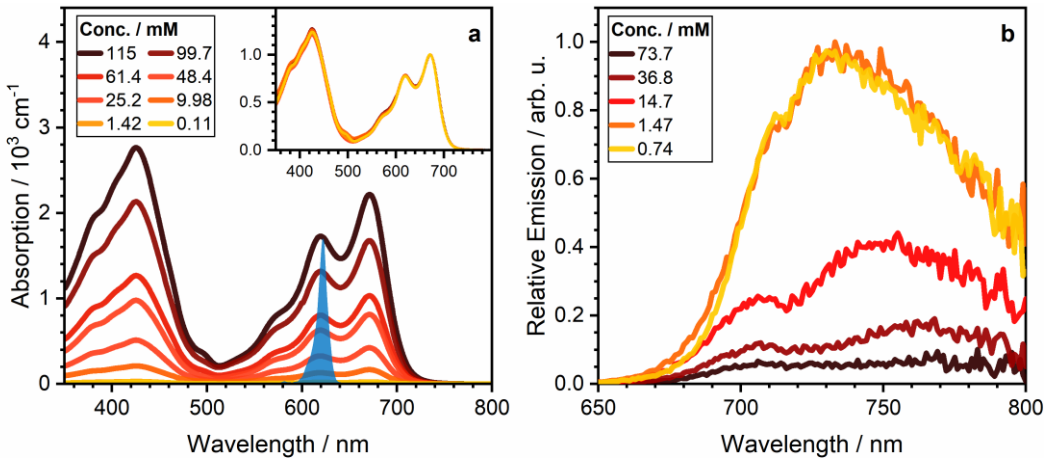


***Figure 5.8:*** *a) Stationary absorption spectra of $TDCl_4$ in toluene for concentrations ranging from 0.11 to 115 mM. Two strong absorption bands are observed at 425 and 670 nm. The normalized absorption spectra in the inset indicates the absence of any aggregation or other self-interaction effects. The blue area represents the excitation spectrum for subsequent TA measurements, centred at 620 nm. b) The Stationary emission spectra (normalized for the emission maximum at lowest concentration) exhibit concentration dependent fluorescence quenching as well as the appearance of a local minimum at 720 nm. Reprinted with permission from ref. 179. Copyright © 2020, American Chemical Society.*

*Transient Absorption Measurements of Concentrated Solutions.*

TA measurements of a 115 mM solution of $TDCl_4$ in toluene were carried out in both the short (fs to ps) as well as the long-time (ns to µs) setup (Figure 5.9). The excitation wavelength was set to the second vibronic peak (620 nm), corresponding to an excess vibrational energy of ≈145 eV. First, spectral feature and dynamics observed in the short-time measurement will be discussed, followed by the results of long-time measurements. Upon photoexcitation, an intense ESA band with its maximum at 540 nm is observed (Figure 5.9a). Additional, weaker features are visible at 640 and 720 nm. The intense negative signal at 680 nm mirrors the stationary absorption spectrum and hence is assigned to GSB. In contrast, no negative signal is observed at the maximum of the emission band (730 nm). This conflicts with ground state absorption and SE inherently having the same Einstein coefficients and consequently the same transition probability at early probe delays.[144] Therefore, the negative SE signal must be overcompensated by an overlapping ESA with stronger oscillator strength. Within 50 ps, the initial signal experiences a slight blue-shift of 2 nm while otherwise retaining its characteristic spectral features. A further evolution of the

transient spectra occurs on the nanosecond timescale (Figure 5.9c). Here, a strong decrease of signal intensity is observed. The remaining ESA strongly overlaps the initial ESA. However, two new and characteristic spectral features emerge at 570 and 610 nm. During this spectral evolution, a transient isosbestic point is identified at 610 nm, which is indicative of a direct state-to-state conversion. No further evolution is observed. The long-time measurement is not able to resolve the initial blue-shift due to its temporal resolution. However, the spectral features at early probe delays perfectly match the transient spectrum at 50 ps probe delay (Figure 5.9b). In addition, the broader spectral range of the long-time measurement allows for an identification of additional spectral features. These include two weak features around 410 and 900 nm. The transition to the second ESA is observed on the same timescale as well (Figure 5.9d), with an additional isosbestic point being present at 420 nm. Furthermore, the extended time window shows that the offset of the short-time measurement decays completely on the microsecond timescale. In total, the dynamics from the femto- to microsecond timescale can be explained by three exponential decays (see appendix section E.1). The short-time measurement can be fitted globally with two time constants ($\tau_1$ and $\tau_2$) and a non-decaying offset. The first time constant amounts to $\tau_1$ = 6.23 ±0.16 ps and a value of 1.15 ±0.01 ns is obtained for $\tau_2$. For the long-time measurement, a global biexponential decay is observed as well. Here, $\tau_1$ cannot be resolved due to the temporal resolution (≈300 ps). Thus, the first fitted time constant (1.18 ± 0.01 ns) corresponds to $\tau_2$ observed in the short-time measurement. The final time constant $\tau_3$ = 584 ± 9 ns is related to the complete decay of the signal. In addition, the time constant related to the loss of SE, $\tau_2$, is in agreement with the observed emission decay $\tau_{Em}$ = 1.46 ns, which remains constant over the whole emission band (*vide infra*).

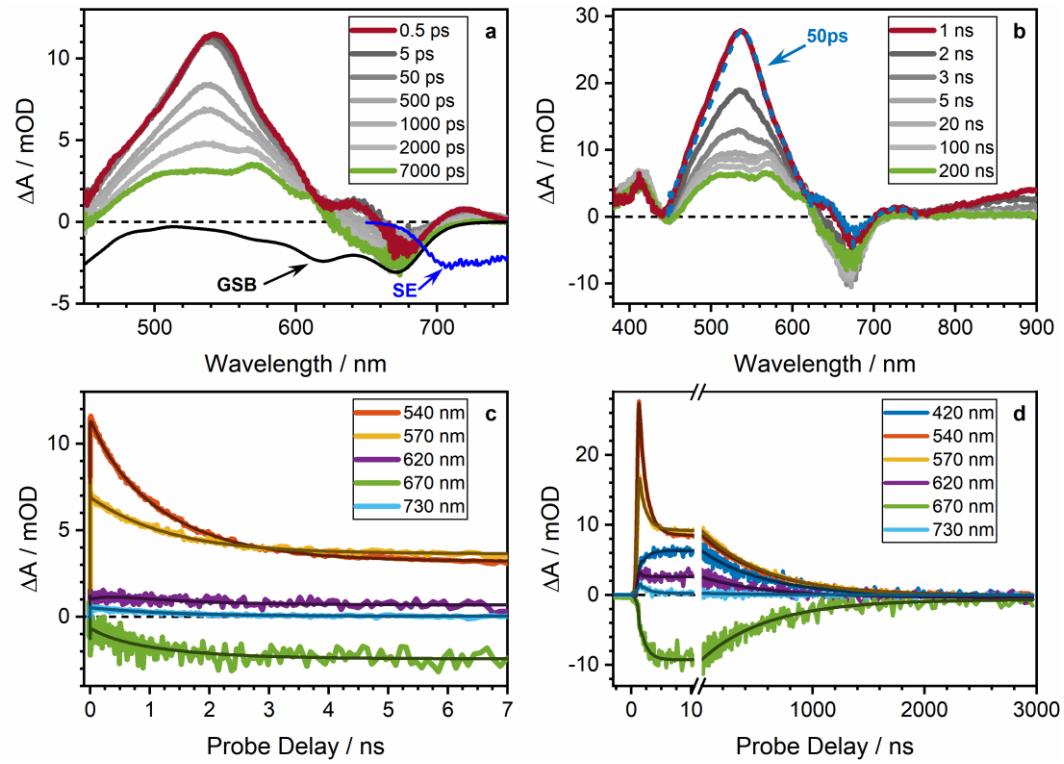


***Figure 5.9:*** *(a,b) Transient spectra and (c,d) kinetic traces with respective fits of a 115 mM solution of $TDCl_4$ obtained by (left) short and (right) long-time TA measurements. a,c) Upon photoexcitation, a broad ESA with its maximum at 540 nm with weaker features at 640 and 720 nm is observed. Initially, a fast (<50 ps) shift of its maximum by 2 nm is observed while retaining its overall spectral shape. Despite a clearly visible GSB at 670 nm, no SE is present. This is attributed to the red-shifted ESA feature having a stronger oscillator strength, overcompensating the negative signal expected for SE. Within nanoseconds, the initial signal decays and gives rise to a second set of spectral features possessing characteristic peaks at 570 and 610 nm. The isosbestic point at 610 nm indicates a direct state-to-state conversion. b,d) While the long-time TA measurement is not able to resolve the fast spectral shift of the initial ESA band, the broader spectral window allows for the identification of additional features at 410 and ≈900 nm. In addition, a second isosbestic point is identified at 420 nm. The extended time window further shows the decay of the second ESA band on the microsecond timescale. Reprinted with permission from ref. 179. Copyright © 2020, American Chemical Society.*

*Identification of Electronic Species.*

In order to assign the experimentally obtained time constants to physical processes, the characteristic spectral features of the transient spectra are to be assigned to electronic states. In general, as two significantly distinct sets of spectral features are observed, two electronic states are assumed. Based on selection rules, the initial ESA band is assigned to the first excited singlet state. In addition, the chromophores are expected to populate higher vibrational levels directly upon photoexcitation due to the

excitation at the second vibronic transition (*vide supra*). Thus, the initial transient spectrum is assigned to $S_1^*$. Due to collisions with surrounding solvent molecules, this species undergoes vibrational cooling with the corresponding time constant $\tau_1$.[179] The product of this reaction, the relaxed $S_1$, requires more energy for the $S_1 \rightarrow S_n$ transition, resulting in the observed blue-shift of the spectrum. The second time constant $\tau_2$ corresponds to significant spectral changes as well as loss of SE. Combined with the long lifetime of the emerging species, comparable to pentacene in benzene (300 ns),[180] this points towards a optically dark state with a spin-forbidden relaxation pathway. Thus, the third species is assigned to $T_1$. In conclusion, the dynamics of a highly concentrated solution of $TDCl_4$ can be described as a three-step sequential reaction. Initially, $S_1^*$ undergoes vibrational cooling to the relaxed $S_1$. This is followed by a direct conversion to $T_1$. This model is applied to obtain the respective SADS (Figure 5.10a). $S_1$ and $T_1$ SADS for both short and long-time measurements show a great agreement. This demonstrates the high quality and reproducibility of experimental data across both setups.

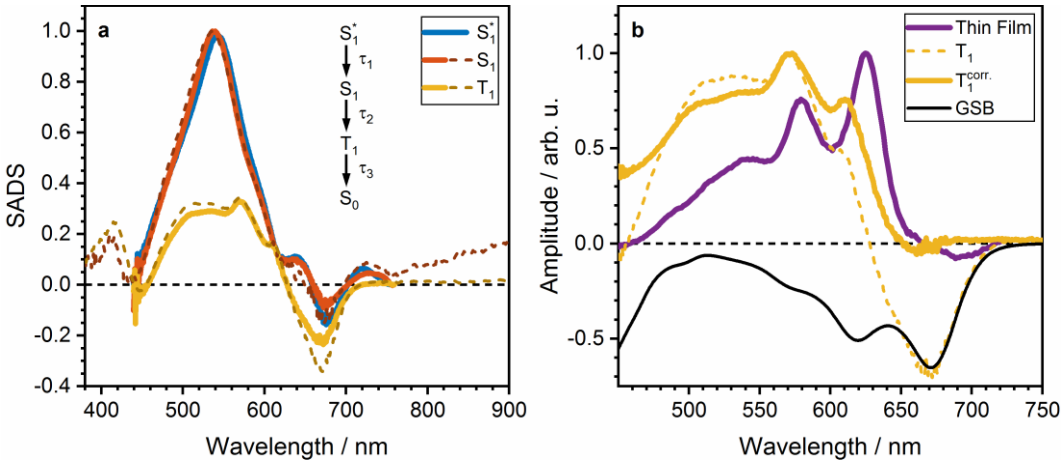


***Figure 5.10:*** *a) SADS obtained by applying a three-step sequential model to short (solid lines) and long-time measurements (dashed lines). The spectra are normalized for the maximum of the $S_1$ SADS. Aside from slight deviations for the GSB, both measurements show a perfect overlap for both $S_1$ and $T_1$ SADS. b) A comparison of the $T_1$ spectrum obtained in thin films of $TDCl_4$ and GSB corrected triplet SADS ($T_1^{corr.}$). All spectra are normalized to their respective maximum. The corrected spectrum shares the same vibronic structure with thin film measurements. The small bathochromic shift of ≈15 nm is attributed to the formation of J-aggregates in solid state. Adapted with permission from ref. 179. Copyright © 2020, American Chemical Society.*

The proposed model is further corroborated by a comparison of the GSB-corrected $T_1$ SADS to the triplet spectrum obtained in thin films of $TDCl_4$ (Figure 5.10b).[21] Both spectra exhibit three distinct vibronic transitions with a small bathochromic shift of ≈15 nm for the measurement in solution. This is attributed to the formation of J-aggregates in solid state, as observed in stationary absorption spectra.[21] This comparison reinforces the assignment of the long-living species to $T_1$.

### 5.2.2 Concentration Dependent Changes in Triplet Formation Dynamics

Having identified the formation of $T_1$, the underlying mechanism will be disclosed by variation of the chromophore concentration. To begin with, the possibility of sequential SF is considered. In section 5.1, it was established that energy transfer to $^3O_2$ is the first and thus crucial step. However, as this reaction hinges on diffusion, it naturally occurs relatively slow on the nanosecond timescale. Under ambient conditions, the diffusion time of oxygen in toluene amounts to $\tau_D = (k_D)^{-1} = 16.1$ ns.[170, 174] This is significantly slower than the experimental time constant of $\tau_2 = 1.15 \pm 0.01$ ns. Consequently, the characteristic delayed increase of the $T_1$ signal is absent and sequential SF can be excluded. Another observation made in the TA measurements is the formation of $T_1$ in a direct state-to-state conversion, as indicated by the isosbestic points in the transient spectra. A possible mechanism fulfilling this requirement would be ISC. Given that it is an intramolecular process, the corresponding rate constant should not depend on chromophore concentration. However, a clearly visible deceleration of the singlet decay is observed upon decreasing the concentration (Figure 5.11a,b). This suggests an intermolecular process being responsible for the triplet formation. In order to uncover the underlying mechanism, the long-time kinetics of $TDCl_4$ are globally analysed, with chromophore concentrations ranging from 0.11 to 115 mM. A satisfactory depiction of the experimental data is achieved by carrying out a biexponential fit with offset for the most dilute solution (0.11 mM) and for concentrations exceeding 10 mM. In turn, an additional exponential decay was used in the range of 0.45 to 9.98 mM.

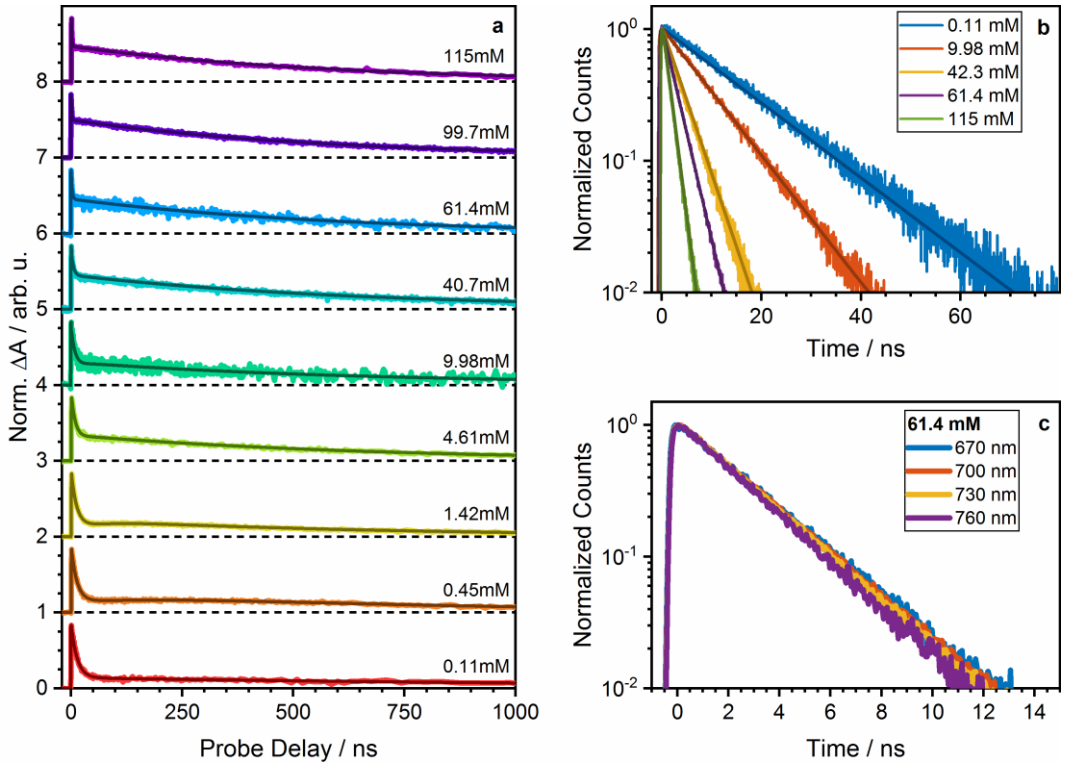


***Figure 5.11:*** *a) Transients of $TDCl_4$ at the maximum of the $T_1$ signal (570 nm) show a concentration dependent change in their kinetics. Upon increasing the concentration, the decay of the initial $S_1$ signal is accelerated (see also panel b). In addition, for concentrations <10 mM, a delayed increase of the signal intensity is observed, which is characteristic for sequential SF. b) Corroborating the TA measurements, the time-resolved emission decay depicts the acceleration of $S_1$ with the increasing concentration. c) The emission decay monitored over the whole emission band exhibits an identical behaviour. The absence of an additional long-lived component indicates the absence of an excimer state and that $S_1$ is the only emissive species. Adapted with permission from ref. 179. Copyright © 2020, American Chemical Society.*

In order to avoid confusion with the results of short-time measurements, the respective rate constants obtained for long-time measurements are labelled $k_A$, $k_B$ and $k_C$. For the ensuing discussion of concentration dependent changes in the rate constants first, $k_A$ and $k_B$ are discussed, followed by $k_C$. In addition, three concentration ranges are defined, i.e. low (≤2 mM), intermediate (2 mM < [$TDCl_4$] ≤ 10mM) and concentrated (>10 mM).

*Sequential Singlet Fission at Low- to Intermediate Concentrations.*

For dilute solutions, a global analysis shows the same behaviour of $TDCl_4$ compared to TIPS-Pn: The decay of the initial singlet, characterised by $k_A$, remains constant with

an average rate of (72.9 ± 2.1) × $10^6$ $s^{-1}$, while oxygen-mediated triplet formation ($k_B$) is accelerated (Figure 5.12a). One exception is the most dilute solution (0.11 mM), for which $k_B$ is not observed, which will be discussed later. In addition, deaerating the solution results in a deceleration of the singlet decay as well as no observable $T_1$ intensity (see appendix section E.2). These findings indicate two things. First, the lack of triplet signal shows that ISC is negligible and the singlet decay rate in oxygen-free measurements corresponds to the relaxation of the excited $S_1$ to its ground state *via* nonradiative transitions and fluorescence with the corresponding rate constant $k_R$. Second, the presence of sequential SF in $TDCl_4$ is confirmed. Thus, the second experimentally obtained rate constant is assigned to heterogeneous SF: $k_B = k_{hSF}$. In addition, the difference of the rates for ambient and oxygen-free conditions allows for the extraction of the rate constant for energy transfer (*vide supra*), which amounts to $k_{ET}$ = (19.6 ± 0.5) × $10^6$ $s^{-1}$ under ambient conditions.[181] This value is comparable to the TIPS-Pn as well as the literature value of 62.1 × $10^6$ $s^{-1}$.[170, 181]

*Direct Singlet Fission in Concentrated Solutions.*

In contrast, a global fit of concentrated solutions indicates a linear increase of $k_A$ with concentration (Figure 5.12a). This conflicts with the insensitivity of the singlet decay on chromophore concentrations previously established. In addition, $k_{hSF}$ vanishes completely. These observations can only be explained by a competing singlet decay channel being introduced in concentrated solutions. This additional pathway outcompetes the energy transfer of the excited chromophore to oxygen. Consequently, no $^1O_2$ species is formed and as such a key reactant of heterogeneous SF is missing, inhibiting the reaction. Due to the concentration dependence, an intermolecular process governed by diffusion dynamics appears obvious. As stated previously, the diffusion rate of two identical chromophores can be approximated according to Eq. 26 (page 95). For the given experimental parameters,[182] a bimolecular rate constant of $k_D^{lit}$ = 1.17 × $10^{10}$ $M^{-1}$ $s^{-1}$ is predicted. This is compared to a linear fit of $k_A$, obtained by short and long-time TA measurements as well as the emission decay (*vide supra*). Here, a value of $k_D$ = (0.72 ± 0.03) × $10^{10}$ $M^{-1}$ $s^{-1}$ is obtained, suggesting a good

reaction efficiency of (62 ± 2) %. Thus, a diffusion-controlled, intermolecular reaction is concluded as the additional reaction pathway at high concentrations. In order to identify the underlying mechanism, the relative intensities of the triplet signal at its maximum (570 nm, *cf.* Figure 5.11a) at a probe delay of 50 ns are investigated. For a concentration of 9.98 mM, the highest concentration for which heterogeneous SF is still observable, a value of 0.33 is observed. In contrast, a significant higher triplet intensity of 0.52 is obtained for the most concentrated solution (115 mM). Thus, the intermolecular reaction must have a triplet as its product. These conditions are fulfilled for a diffusion-controlled, direct SF process. For high concentrations, the diffusion rate can compete with other deactivation processes such as nonradiative relaxation or fluorescence. Thus, the fitted diffusion rate $k_{dSF} = k_D$ is assigned to bimolecular, direct SF. Previously, this has been only observed for TIPS-Tn and TIPS-Pn, which do not possess heteroatoms in their aromatic backbone.[25-26] In contrast to both of these acene derivatives, there is no hint of any intermediate triplet pair state. To extract the bimolecular rate constant for heterogeneous SF $k_{hSF}$, the intermediate concentration regime is considered. Here, the rate constants for energy transfer and direct SF are of the same magnitude. Consequently, both processes are observed simultaneously. However, $k_{ET}$ is not dependent on chromophore concentration and as such, $k_{hSF}$ does not interfere with direct SF. Thus, $k_{hSF}$ is obtained as a linear fit of $k_B$ and amounts to $(1.10 \pm 0.06) \times 10^{10}$ $M^{-1}$ $s^{-1}$.

### 5.2.3 Unified Kinetic Model

With all singlet decay mechanisms identified, a kinetic model is formulated (Figure 5.12c) which expands the one presented in section 5.1. Upon photoexcitation, $S_1^*$ is formed. This undergoes vibrational cooling on the ps timescale and results in the vibrationally relaxed excited singlet $S_1$. This singlet decays with the experimentally obtained rate constant $k_A$ *via* three competing pathways. First, the concentration independent relaxation to the ground state either *via* fluorescence or nonradiative transitions ($k_R$). Second, a collision of $S_1$ with a ground state chromophore yields two triplet states *via* direct SF ($k_{dSF}$). This reaction is diffusion-controlled and thus

depends on chromophore concentration. As only a small fraction of molecules is excited, a pseudo-first reaction order is observed. In the final reaction pathway, sequential SF takes place. Initially, the excited chromophore sensitizes molecular oxygen in its triplet ground state with the rate constant $k_{ET}$, resulting in a triplet chromophore and the reactive $^1O_2$ species. The latter interacts with a ground-state chromophore in a heterogeneous SF process ($k_{hSF}$), recovering $^3O_2$ and resulting in an additional triplet chromophore.

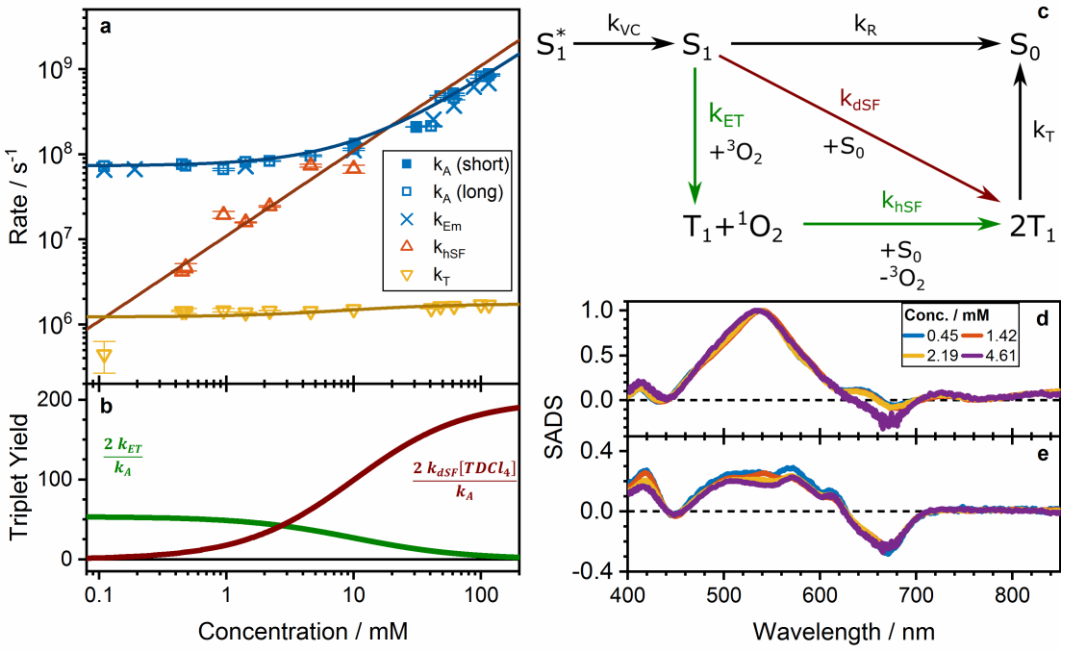


***Figure 5.12:*** *a) Rate constants obtained with short and long-time TA measurements as well as emission decay. In dilute solutions (≤2 mM), a constant singlet decay ($k_A$) and a linearly increasing $k_{hSF}$ is observed, in agreement with sequential SF. In contrast, $k_A$ increases linearly for concentrations >10 mM. This behaviour is attributed to a diffusion-controlled, direct SF process. At intermediate concentrations (2 mM<[TDCl$_4$]≤10 mM), both direct and sequential SF are observed simultaneously. Linear fits of $k_{hSF}$ and $k_A$ at high concentrations result in bimolecular rate constants $k_{hSF}=(1.10 \pm 0.06)\times10^{10}$ $M^{-1}$ $s^{-1}$ and $k_{dSF}=(0.72 \pm 0.03)\times10^{10}$ $M^{-1}$ $s^{-1}$. b) Triplet yield for sequential and direct SF. Assuming a quantitative heterogeneous SF process, the triplet yield for sequential SF is obtained as the ratio between $k_{ET}$ and the total singlet decay rate $k_A$, multiplied by a factor of two. Upon increasing the concentration, direct SF outcompetes energy transfer. Consequently, as the probability of this reaction increases, so does the triplet yield. At the highest measured concentration, a triplet yield of 189±5% is achieved. d,e) The SADS for d) $S_1$ and e) $T_1$ exhibit no systematic spectral changes upon varying the concentrations. This supports the proposed model including competing direct and heterogeneous SF. Adapted with permission from ref. 179. Copyright © 2020, American Chemical Society.*

In conclusion, the total singlet decay rate $k_A$ is formulated as

$$k_A = k_R + k_{ET} + k_{dSF}[\mathrm{TDCl_4}] \qquad \text{Eq. 30}$$

This allows to assess the probability of the individual singlet decay pathways, *i.e.* their quantum yields (Figure 5.12b). They are calculated as the ratio between the rate constant of the reaction in question and the total singlet decay rate. Consequently, the triplet yield can be estimated straightforward for direct SF: Due to two triplets being generated, the triplet yield equals to twice the quantum yield of this channel. In contrast, energy transfer does not immediately result in two triplet states. However, the long lifetime of $^1O_2$ (26.7 µs in benzene),[183] which significantly exceeds the triplet decay rate, suggests quantitative heterogeneous SF. Therefore, it is valid to assume that sequential SF results in two triplet states as well and consequently, its triplet yield can be assessed as twice the quantum yield of energy transfer. In addition, the time-dependent concentrations and corresponding coefficient matrix for the proposed kinetic model are formulated (see appendix section E.3) to obtain the SADS (Figure 5.12d,e). In general, a good agreement of both $S_1$ and $T_1$ spectra is observed. While slight deviations are observed, they do not exhibit a systematic change with regard to concentration. Thus, the spectral differences are attributed to the strong spectral overlap of both species, which hinders the disentanglement.

*Triplet Quantum Yield.*

The quantum yields are important to discuss the behaviour of $k_C$. Excluding the most dilute solution, the latter shows a slight yet systematic increase from 1.45 to $1.71 \times 10^6$ $s^{-1}$ upon increasing the concentration from 0.45 to 115 mM. A higher triplet decay rate at higher concentrations initially suggests diffusion-controlled TTA. However, this bimolecular reaction would result in a squared dependence on $T_1$ concentration and as such conflicts with the observed monoexponential decay for all concentrations. Another consideration targets the way the triplets are generated. In the case of sequential SF, both triplets are generated far apart from each other. As such,

the only relaxation pathway is spin-forbidden ISC. In contrast, direct SF generates the triplets close to each other. Thus, a plausible explanation for the faster decay is that a weakly bound triplet excimer is generated. A stronger interaction is excluded, as no changes in the triplet spectra are observed upon varying the concentration. In consequence, the acceleration suggests that the triplet excimer exhibits a faster triplet decay compared to the isolated triplets. According to this hypothesis, the triplet decay rate $k_T$ can be formulated as the sum of the rates for the unimolecular decay channel $k_{T,1}$ and the excimer decay rate $k_{T,2}$. These rates have to be weighted with the relative population of the generated triplet species, *i.e.* their quantum yield:

$$k_T = \frac{2k_{ET}}{k_A} \cdot k_{T,1} + \frac{2k_{dSF}[\mathrm{TDCl_4}]}{k_A} \cdot k_{T,2} \qquad \text{Eq. 31}$$

Applying this function to the experimentally obtained triplet decay rates accurately fits the observed concentration dependence and yields values of $k_{T,1}$ = (1.75 ± 0.14) × $10^6$ $s^{-1}$ and $k_{T,1}$ = (4.57 ± 0.42) × $10^6$ $s^{-1}$. A notable exception is the most dilute solution (0.11 mM), which will be explained in the following. Intriguingly, no heterogeneous SF is observed in this measurement, yet a notable $T_1$ signal is present. As stated previously, oxygen-free measurements show that ISC can be discarded as triplet formation mechanism. Thus, in combination with the expected negligible rate for direct SF at this low concentration, energy transfer is the only triplet formation mechanism. Consequently, $^1O_2$ is generated and heterogeneous SF would in principle be feasible. However, the low chromophore concentration does not only affect direct but also heterogeneous SF: The bimolecular rate for $k_{hSF}$ predicts a rate of (0.12 ± 0.01) × $10^6$ $s^{-1}$, whereas a triplet decay rate of 1.23 × $10^6$ $s^{-1}$ is expected according to Eq. 31. Thus, heterogeneous SF becomes the rate determining step within the reaction mechanism. Furthermore, it is noted that the triplets generated by energy transfer are not influenced by this and expected to decay with $k_{T,1}$. However, the combination of the overall low $T_1$ signal intensity and the superposition of heterogeneous SF and triplet decay means that this decay is not resolvable.

## 5.3 Conclusion

The variation of the oxygen concentration constitutes the first report on the influence of molecular oxygen on SF dynamics. It was demonstrated that the individually well-known processes[13-14] of $^3O_2$ sensitisation and excitation of a ground state chromophore by $^1O_2$ can be combined to a two-step, sequential SF mechanism with $O_2$ acting as catalyst. This allows for a moderate triplet yield of 40 % to be achieved, even at low to intermediate chromophore concentrations. The probability of this pathway can be selectively tuned by adjusting the $O_2$ concentration. Furthermore, the energy requirements for the individual steps of sequential SF have been established. In order for energy transfer to occur, the $S_1 - T_1$ gap has to exceed the excitation energy of $^3O_2$ (0.97 eV). In turn, heterogeneous SF requires the $T_1$ energy to be lower than 0.97 eV. Given that chromophores fulfilling both requirements also automatically fulfil $\Delta E_{SF} < 0$, sequential SF is an easy method to screen possible SF chromophores. Furthermore, the stepwise generation of triplets results in them being spatially separated from each other. This reduces TTA and extends triplet lifetime.

A variation of the concentration of $TDCl_4$ has been shown to strongly affect the branching between individual reaction channels of the photoexcited state. While at low concentrations, intramolecular deactivation and sequential SF are prevalent, direct SF dominates in concentrated solutions. This leads to almost quantitative triplet yield of 189±5 %. In addition, no excimer intermediate has been observed, in contrast to previous studies of hydrocarbon acene derivatives.[25-27] This has two possible explanations, based on the discussion whether or not the excimer constitutes a trap state.[70] If on the one hand, excimers do not fulfil the energy matching requirement, it is safe to say that they are not populated in $TDCl_4$ given the high triplet yields. On the other hand, if SF in solution generally proceeds through an excimer intermediate, it is either extremely short-lived or non-emissive in $TDCl_4$, hindering its detection. Regardless of which of both approaches is correct, the absence of an excimer state points towards a low binding energy of $^1(TT)$.

# 6 Summary and Outlook

## 6.1 Summary and Discussion

This work establishes how competitive reaction pathways influence SF dynamics in consideration of the physical state of the reaction system. While the main goal in both solution and solid state is to increase the triplet yield by reducing possible deactivation channels, the approach is fundamentally different. In solid state, it has been shown that the main task is to effectively manage inter-chromophore interactions to allow for an efficient formation and subsequent separation of $^1(TT)$. In solution, SF depends on the concentration of the chromophore as well as molecular oxygen. The importance of the latter and how it can be used to increase the overall triplet yield has been demonstrated for the first time. High chromophore concentrations result in diffusion-controlled SF, which efficiently outcompetes other reaction channels, thus leading to triplet yields close to 200%. This process has been shown to occur intermediate-free, refuting the general notion of excimer states as intermediates in solution-based SF.

### 6.1.1 First Observation of Singlet Fission in Tetraazaperopyrenes

The formation of $^1(TT)$ on the sub-100 fs timescale for TAPP-Cl and TAPP-Br and its subsequent decorrelation proves the viability of SF in a new class of molecules. In consequence, aza-substitution is emphasised as a tool to achieve suitable molecular properties for SF.

Dilute solutions of halogenated TAPPs and their unsubstituted counterpart allowed for the identification of spectral features of $S_1$ and $T_1$. Additionally, intramolecular reaction channels have been identified and evaluated, and the influence of $S_1 - T_2$ energy detuning on the ISC rate has been unveiled. These findings have proven to be invaluable assets for the identification of SF in TAPP-Cl and TAPP-Br thin films. Here, aggregation effects in indicate a stabilisation of $S_1$, in turn increasing $\Delta E_{\mathrm{SF}}$. Nonetheless, SF remains energetically feasible with it being more efficient in TAPP-Br. This contrasts expectations, given the more favourable energetics for

TAPP-Cl. However, three effects are unveiled which explain this behaviour. First, an increased excimer formation competing with SF is observed in TAPP-Cl. Second, the more pronounced vibrational dynamics in TAPP-Br may play a crucial role to overcome activation barriers and/or the decorrelation of $^1(TT)$. Third, enhanced spin-orbit coupling in TAPP-Br potentially lowers $^5(TT)$, thus reducing the binding energy of $^1(TT)$.

### 6.1.2 Competing Oxygen-Catalysed and Direct Singlet Fission in Solution

The until now neglected influence of oxygen on SF chromophores has great implications for overall SF dynamics. At a first glance, the inclusion of atmospheric oxygen only seems to open up a new deactivation pathway, as the excited chromophore sensitises the transition of $^3O_2$ to $^1O_2$. However, it has been demonstrated that the reactive singlet oxygen further interacts with a ground state chromophore in a heterogeneous SF process. Both steps combine to a two-step sequential SF process with oxygen acting as a catalyst. The feasibility of this novel mechanism has been shown for TIPS-Pn and for $TDCl_4$, underlining its transferability. Under ambient conditions, a triplet yield of 40% is achieved even for low (<10 mM) chromophore concentrations, which can be tuned by a variation of the oxygen concentration. The main benefit of sequential SF is the spatial separation of the generated triplets. Thus, the reversibility of SF is circumvented and recombination processes like triplet-triplet-annihilation are diminished.

In contrast, a reaction system consisting purely of the chromophore and the solvent exhibits mainly intramolecular deactivation at low concentrations. However, increasing the chromophore concentration leads to more frequent interactions between excited and ground state chromophores. For concentrations >100 mM, this results in an almost quantitative SF process with triplet yields close to 200%. The excimer intermediate discussed in the literature[25-27, 70] is not observed for $TDCl_4$, speaking against its role as an intermediate in solution-based SF.

## 6.2 Outlook

While excimer formation, vibronic coupling and heavy atom effect are all viable explanations for the more efficient SF in TAPP-Br compared to TAPP-Cl, it is improbable that a single contribution on its own is responsible for the observed dynamics. Instead, it is most likely that a combination of all three lead to the experimental findings. In consequence, further research focusing on a single aspect at a time may yield new insights on the SF mechanism. However, in order to disentangle the individual effects, further investigation is required. In a first step, singlet-singlet annihilation should be reduced to eliminate it as an interfering component in the dynamics. In principle, this can be achieved by lowering excitation densities.[132] This approach was not feasible in the present work given the low optical density of the investigated thin films. As the preparation of the films is limited by the solubility of the chromophores, other preparation techniques such as chemical vapour deposition could be tested. A further advantage, especially when combined with thermal annealing, would be a higher crystallinity of the sample, which reduces pump scattering and increases long-range order.

A method to hinder the excimer formation thus improving triplet yields is π-plane twisting.[22, 78] This structural motif has already been realised for bay-substituted TAPP derivatives, allowing for an easy access to suitable chromophores.[85] In addition, increased solubility of these compounds eases the preparation of thin films with high optical densities.

From the presented experimental results, it is ambiguous whether the activity of low-frequency vibrational modes contributes to SF. This could be clarified *e.g.* by spatially resolved TA spectroscopy, which is able to selectively probe subdomains by reducing the spot size of pump and probe beams.[184] Thus, possible effects of the increased long-range order in TAPP-Br thin films would be mitigated. In addition, a differentiation between ground- and excited state vibrational modes would help to unveil the role of low-frequency, intermolecular vibrations in SF. Suitable experimental techniques for this are pump-IVS[65] or 2D-electronic spectroscopy.[67]

Finally, in order to pinpoint the effects of spin-orbit coupling, it would be beneficial to additionally investigate TAPP-H and TAPP-I thin films. As exemplified by the analysis of intramolecular dynamics, this could help to establish clear trends, elucidating the possibly underestimated role of heavy-atom effect in SF.[131]

Direct SF in solution has been shown to circumvent some of the issues encountered in solid state. For example, collisions between chromophore and solvent molecules provide enough energy to separate the correlated triplet pair, diminishing the probability of re-formation of the $S_1$ state. However, the timescale of SF becomes highly dependent on diffusion rates. Thus, it would be beneficial to transfer advantages of solution-based, direct SF to the solid state. To a certain degree, this is achieved by intramolecular SF. Here, chemical modifications and linker design allow for an increased control of inter-chromophore geometry and electronic coupling. This concept can be envisioned to be transferred to sequential SF as an intramolecular catalytic cycle. Here, instead of a direct interaction of the individual chromophores, the linker takes on a more active part in the SF mechanism. Initially, a part of the excitation energy is transferred to it in a process akin to oxygen sensitisation. Subsequently, this energy is transferred to the second, spatially and electronically separated chromophore. While simple in theory, the demands for the electronic structure of the linker would be high. Given that it needs a triplet ground state, it requires two unpaired electrons. In addition, a suitable transition energy to an excited singlet state is needed. Designing such a linker would be a big obstacle to overcome, given that open-shell organic molecules are typically highly reactive. However, there are already promising reports on stable radical species enhancing SF.[71] Thus, further investigations for sequential intramolecular SF could start at this point, *e.g.* by creating a dimer with two radical moieties.

# References


1. DWD, *Jahre mit der höchsten Durchschnittstemperatur in Deutschland von 1881 bis 2019* (in Grad Celsius).* Statista GmbH, https://de.statista.com/statistik/daten/studie/164050/umfrage/waermste-jahre-in-deutschland-nach-durchschnittstemperatur/ (accessed 13.10.2020).
2. Vereinte Nationen, *Sammlung völkerrechtlicher Verträge.* https://treaties.un.org/Pages/ViewDetails.aspx?src=IND&mtdsg_no=XXVII-7-d&chapter=27&clang=_en (accessed 13.10.2020).
3. Fraunhofer ISE, *Aktuelle Fakten zur Photovoltaik in Deutschland.* https://www.ise.fraunhofer.de/de/veroeffentlichungen/studien/aktuelle-fakten-zur-photovoltaik-in-deutschland.html (accessed 14.04.2020).
4. Fraunhofer ISE, *Photovoltaics Report.* https://www.ise.fraunhofer.de/de/veroeffentlichungen/studien/photovoltaics-report.html (accessed 13.10.2020).
5. Shockley, W.; Queisser, H. J. Detailed Balance Limit of Efficiency of p-n Junction Solar Cells. *J. Appl. Phys.* **1961,** *32*, 510-519.
6. Smith, M. B.; Michl, J. Singlet fission. *Chem. Rev.* **2010,** *110*, 6891-936.
7. Smith, M. B.; Michl, J. Recent advances in singlet fission. *Annu. Rev. Phys. Chem.* **2013,** *64*, 361-86.
8. Hanna, M. C.; Nozik, A. J. Solar conversion efficiency of photovoltaic and photoelectrolysis cells with carrier multiplication absorbers. *J. Appl. Phys.* **2006,** *100*, 074510.
9. Congreve, D. N.; Lee, J.; Thompson, N. J.; Hontz, E.; Yost, S. R.; Reusswig, P. D.; Bahlke, M. E.; Reineke, S.; Van Voorhis, T.; Baldo, M. A. External Quantum Efficiency Above 100% in a Singlet-Exciton-Fission Based Organic Photovoltaic Cell. *Science* **2013,** *340*, 334-337.
10. Einzinger, M.; Wu, T.; Kompalla, J. F.; Smith, H. L.; Perkinson, C. F.; Nienhaus, L.; Wieghold, S.; Congreve, D. N.; Kahn, A.; Bawendi, M. G., et al. Sensitization of silicon by singlet exciton fission in tetracene. *Nature* **2019,** *571*, 90-94.
11. Rao, A.; Friend, R. H. Harnessing singlet exciton fission to break the Shockley–Queisser limit. *Nat. Rev. Mat.* **2017,** *2*, 17063.
12. Roy, P. P.; Kato, Y.; Abe-Yoshizumi, R.; Pieri, E.; Ferre, N.; Kandori, H.; Buckup, T. Mapping the ultrafast vibrational dynamics of all-trans and 13-cis retinal isomerization in Anabaena Sensory Rhodopsin. *Phys. Chem. Chem. Phys.* **2018,** *20*, 30159-30173.
13. Kearns, D. R. Physical and chemical properties of singlet molecular oxygen. *Chem. Rev.* **1971,** *71*, 395-427.
14. Schweitzer, C.; Schmidt, R. Physical Mechanisms of Generation and Deactivation of Singlet Oxygen. *Chem. Rev.* **2003,** *103*, 1685-1758.
15. Herz, J.; Buckup, T.; Paulus, F.; Engelhart, J.; Bunz, U. H.; Motzkus, M. Acceleration of Singlet Fission in an Aza-Derivative of TIPS-Pentacene. *J. Phys. Chem. Lett.* **2014,** *5*, 2425-30.
16. Herz, J.; Buckup, T.; Paulus, F.; Engelhart, J. U.; Bunz, U. H.; Motzkus, M. Unveiling Singlet Fission Mediating States in TIPS-pentacene and its Aza Derivatives. *J. Phys. Chem. A* **2015,** *119*, 6602-10.

17. Marciniak, H.; Pugliesi, I.; Nickel, B.; Lochbrunner, S. Ultrafast singlet and triplet dynamics in microcrystalline pentacene films. *Phys. Rev. B* **2009,** *79*, 235318.
18. Wilson, M. W. B.; Rao, A.; Clark, J.; Kumar, R. S. S.; Brida, D.; Cerullo, G.; Friend, R. H. Ultrafast Dynamics of Exciton Fission in Polycrystalline Pentacene. *J. Am. Chem. Soc.* **2011,** *133*, 11830-11833.
19. Albrecht, W. G.; Michel-Beyerle, M. E.; Yakhot, V. Exciton fission in excimer forming crystal. Dynamics of an excimer build-up in α-perylene. *Chem. Phys.* **1978,** *35*, 193-200.
20. Le, A. K.; Bender, J. A.; Arias, D. H.; Cotton, D. E.; Johnson, J. C.; Roberts, S. T. Singlet Fission Involves an Interplay between Energetic Driving Force and Electronic Coupling in Perylenediimide Films. *J. Am. Chem. Soc.* **2018,** *140*, 814-826.
21. Alagna, N.; Han, J.; Wollscheid, N.; Lustres, J. L. P.; Herz, J.; Hahn, S.; Koser, S.; Paulus, F.; Bunz, U. H. F.; Dreuw, A., et al. Tailoring Ultrafast Singlet Fission by the Chemical Modification of Phenazinothiadiazoles. *J. Am. Chem. Soc.* **2019,** *141*, 8834-8845.
22. Felter, K. M.; Dubey, R. K.; Grozema, F. C. Relation between molecular packing and singlet fission in thin films of brominated perylenediimides. *J. Chem. Phys.* **2019,** *151*, 094301.
23. Nichols, V. M.; Rodriguez, M. T.; Piland, G. B.; Tham, F.; Nesterov, V. N.; Youngblood, W. J.; Bardeen, C. J. Assessing the Potential of Peropyrene as a Singlet Fission Material: Photophysical Properties in Solution and the Solid State. *J. Phys. Chem. Lett.* **2013,** *117*, 16802-16810.
24. Uchida, K.; Kubo, T.; Yamanaka, D.; Furube, A.; Matsuzaki, H.; Nishii, R.; Sakagami, Y.; Abulikemu, A.; Kamada, K. Synthesis, crystal structure, and photophysical properties of 2,9-disubstituted peropyrene derivatives. *Can. J. Chem.* **2017,** *95*, 432-444.
25. Stern, H. L.; Musser, A. J.; Gelinas, S.; Parkinson, P.; Herz, L. M.; Bruzek, M. J.; Anthony, J.; Friend, R. H.; Walker, B. J. Identification of a triplet pair intermediate in singlet exciton fission in solution. *Proc. Natl. Acad. Sci. U.S.A.* **2015,** *112*, 7656—7661.
26. Walker, B. J.; Musser, A. J.; Beljonne, D.; Friend, R. H. Singlet exciton fission in solution. *Nat. Chem.* **2013,** *5*, 1019-24.
27. Casillas, R.; Adam, M.; Coto, P. B.; Waterloo, A. R.; Zirzlmeier, J.; Reddy, S. R.; Hampel, F.; McDonald, R.; Tykwinski, R. R.; Thoss, M., et al. Intermolecular Singlet Fission in Unsymmetrical Derivatives of Pentacene in Solution. *Adv. Energy Mater.* **2019,** *9*.
28. Alagna, N.; Lustres, J. L. P.; Roozbeh, A.; Han, J.; Hahn, S.; Berger, F. J.; Zaumseil, J.; Dreuw, A.; Bunz, U. H. F.; Buckup, T. Ultrafast Singlet Fission in Rigid Azaarene Dimers with Negligible Orbital Overlap. *J. Phys. Chem. B* **2020**.
29. Alagna, N.; Perez Lustres, J. L.; Wollscheid, N.; Luo, Q.; Han, J.; Dreuw, A.; Geyer, F. L.; Brosius, V.; Bunz, U. H. F.; Buckup, T., et al. Singlet Fission in Tetraaza-TIPS-Pentacene Oligomers: From fs Excitation to µs Triplet Decay via the Biexcitonic State. *J. Phys. Chem. B* **2019,** *123*, 10780-10793.
30. Singh, S.; Jones, W. J.; Siebrand, W.; Stoicheff, B. P.; Schneider, W. G. Laser Generation of Excitons and Fluorescence in Anthracene Crystals. *J. Chem. Phys.* **1965,** *42*, 330-342.
31. Swenberg, C. E.; Stacy, W. T. Bimolecular radiationless transitions in crystalline tetracene. *Chem. Phys. Lett.* **1968,** *2*, 327-328.
32. Austin, R. H.; Baker, G. L.; Etemad, S.; Thompson, R. Magnetic field effects on triplet exciton fission and fusion in a polydiacetylene. *J. Chem. Phys.* **1989,** *90*, 6642-6646.

33. Casanova, D. Theoretical Modeling of Singlet Fission. *Chem. Rev.* **2018,** *118*, 7164-7207.
34. Miyata, K.; Conrad-Burton, F. S.; Geyer, F. L.; Zhu, X. Y. Triplet Pair States in Singlet Fission. *Chem. Rev.* **2019,** *119*, 4261-4292.
35. Musser, A. J.; Clark, J. Triplet-Pair States in Organic Semiconductors. *Annu. Rev. Phys. Chem.* **2019,** *70*, 323-351.
36. Monahan, N.; Zhu, X. Y. Charge transfer-mediated singlet fission. *Annu. Rev. Phys. Chem.* **2015,** *66*, 601-18.
37. Casillas, R.; Papadopoulos, I.; Ullrich, T.; Thiel, D.; Kunzmann, A.; Guldi, D. M. Molecular insights and concepts to engineer singlet fission energy conversion devices. *Energy Environ. Sci.* **2020,** *13*, 2741-2804.
38. Ito, S.; Nagami, T.; Nakano, M. Molecular design for efficient singlet fission. *J. Photochem. Photobiol., C* **2018,** *34*, 85-120.
39. Merrifield, R. E. Magnetic Effects on Triplet Exciton Interactions. *Pure Appl. Chem.* **1971,** *27*, 481-498.
40. Scholes, G. D. Correlated Pair States Formed by Singlet Fission and Exciton-Exciton Annihilation. *J. Phys. Chem. A* **2015,** *119*, 12699-705.
41. Pensack, R. D.; Ostroumov, E. E.; Tilley, A. J.; Mazza, S.; Grieco, C.; Thorley, K. J.; Asbury, J. B.; Seferos, D. S.; Anthony, J. E.; Scholes, G. D. Observation of Two Triplet-Pair Intermediates in Singlet Exciton Fission. *J. Phys. Chem. Lett.* **2016,** *7*, 2370-5.
42. Lee, T. S.; Lin, Y. L.; Kim, H.; Pensack, R. D.; Rand, B. P.; Scholes, G. D. Triplet Energy Transfer Governs the Dissociation of the Correlated Triplet Pair in Exothermic Singlet Fission. *J. Phys. Chem. Lett.* **2018,** *9*, 4087-4095.
43. Aulin, Y. V.; Felter, K. M.; Günbas, D. D.; Dubey, R. K.; Jager, W. F.; Grozema, F. C. Morphology-Independent Efficient Singlet Exciton Fission in Perylene Diimide Thin Films. *ChemPlusChem* **2018,** *83*, 230-238.
44. Monahan, N. R.; Sun, D.; Tamura, H.; Williams, K. W.; Xu, B.; Zhong, Y.; Kumar, B.; Nuckolls, C.; Harutyunyan, A. R.; Chen, G., et al. Dynamics of the triplet-pair state reveals the likely coexistence of coherent and incoherent singlet fission in crystalline hexacene. *Nat. Chem.* **2017,** *9*, 341-346.
45. Breen, I.; Tempelaar, R.; Bizimana, L. A.; Kloss, B.; Reichman, D. R.; Turner, D. B. Triplet Separation Drives Singlet Fission after Femtosecond Correlated Triplet Pair Production in Rubrene. *J. Am. Chem. Soc.* **2017,** *139*, 11745-11751.
46. Miyata, K.; Kurashige, Y.; Watanabe, K.; Sugimoto, T.; Takahashi, S.; Tanaka, S.; Takeya, J.; Yanai, T.; Matsumoto, Y. Coherent singlet fission activated by symmetry breaking. *Nat. Chem.* **2017,** *9*, 983-989.
47. Stern, H. L.; Cheminal, A.; Yost, S. R.; Broch, K.; Bayliss, S. L.; Chen, K.; Tabachnyk, M.; Thorley, K.; Greenham, N.; Hodgkiss, J. M., et al. Vibronically coherent ultrafast triplet-pair formation and subsequent thermally activated dissociation control efficient endothermic singlet fission. *Nat. Chem.* **2017,** *9*, 1205-1212.
48. Burdett, J. J.; Bardeen, C. J. Quantum Beats in Crystalline Tetracene Delayed Fluorescence Due to Triplet Pair Coherences Produced by Direct Singlet Fission. *J. Am. Chem. Soc.* **2012,** *134*, 8597-8607.
49. Dirac, P. A. M.; Bohr, N. H. D. The quantum theory of the emission and absorption of radiation. *Proc. R. Soc. London, Ser. A* **1927,** *114*, 243-265.

50. Berkelbach, T. C.; Hybertsen, M. S.; Reichman, D. R. Microscopic Theory of Singlet Exciton Fission. II. Application to Pentacene Dimers and the Role of Superexchange. *J. Chem. Phys.* **2013,** *138*, 114103.
51. Miller, C. E.; Wasielewski, M. R.; Schatz, G. C. Modeling Singlet Fission in Rylene and Diketopyrrolopyrrole Derivatives: The Role of the Charge Transfer State in Superexchange and Excimer Formation. *J. Phys. Chem. Lett.* **2017,** *121*, 10345-10350.
52. Le, A. K.; Bender, J. A.; Roberts, S. T. Slow Singlet Fission Observed in a Polycrystalline Perylenediimide Thin Film. *J. Phys. Chem. Lett.* **2016,** *7*, 4922-4928.
53. Margulies, E. A.; Logsdon, J. L.; Miller, C. E.; Ma, L.; Simonoff, E.; Young, R. M.; Schatz, G. C.; Wasielewski, M. R. Direct Observation of a Charge-Transfer State Preceding High-Yield Singlet Fission in Terrylenediimide Thin Films. *J. Am. Chem. Soc.* **2017,** *139*, 663-671.
54. Hart, S. M.; Silva, W. R.; Frontiera, R. R. Femtosecond stimulated Raman evidence for charge-transfer character in pentacene singlet fission. *Chem. Sci.* **2018,** *9*, 1242-1250.
55. Lukman, S.; Chen, K.; Hodgkiss, J. M.; Turban, D. H. P.; Hine, N. D. M.; Dong, S.; Wu, J.; Greenham, N. C.; Musser, A. J. Tuning the Role of Charge-Transfer States in Intramolecular Singlet Exciton Fission Through Side-Group Engineering. *Nat. Commun.* **2016,** *7*, 13622.
56. Yago, T.; Ishikawa, K.; Katoh, R.; Wakasa, M. Magnetic Field Effects on Triplet Pair Generated by Singlet Fission in an Organic Crystal: Application of Radical Pair Model to Triplet Pair. *J. Phys. Chem. C* **2016,** *120*, 27858-27870.
57. Bayliss, S. L.; Weiss, L. R.; Mitioglu, A.; Galkowski, K.; Yang, Z.; Yunusova, K.; Surrente, A.; Thorley, K. J.; Behrends, J.; Bittl, R., et al. Site-selective measurement of coupled spin pairs in an organic semiconductor. *Proc. Natl. Acad. Sci. U.S.A.* **2018,** *115*, 5077-5082.
58. Yong, C. K.; Musser, A. J.; Bayliss, S. L.; Lukman, S.; Tamura, H.; Bubnova, O.; Hallani, R. K.; Meneau, A.; Resel, R.; Maruyama, M., et al. The entangled triplet pair state in acene and heteroacene materials. *Nat. Commun.* **2017,** *8*, 15953.
59. Weiss, L. R.; Bayliss, S. L.; Kraffert, F.; Thorley, K. J.; Anthony, J. E.; Bittl, R.; Friend, R. H.; Rao, A.; Greenham, N. C.; Behrends, J. Strongly exchange-coupled triplet pairs in an organic semiconductor. *Nat. Phys.* **2016,** *13*, 176-181.
60. Tayebjee, M. J. Y.; Sanders, S. N.; Kumarasamy, E.; Campos, L. M.; Sfeir, M. Y.; McCamey, D. R. Quintet multiexciton dynamics in singlet fission. *Nat. Phys.* **2016,** *13*, 182-189.
61. Lubert-Perquel, D.; Salvadori, E.; Dyson, M.; Stavrinou, P. N.; Montis, R.; Nagashima, H.; Kobori, Y.; Heutz, S.; Kay, C. W. M. Identifying triplet pathways in dilute pentacene films. *Nat. Commun.* **2018,** *9*, 4222.
62. Basel, B. S.; Zirzlmeier, J.; Hetzer, C.; Phelan, B. T.; Krzyaniak, M. D.; Reddy, S. R.; Coto, P. B.; Horwitz, N. E.; Young, R. M.; White, F. J., et al. Unified Model for Singlet Fission Within a Non-Conjugated Covalent Pentacene Dimer. *Nat. Commun.* **2017,** *8*, 15171.
63. Kobori, Y.; Fuki, M.; Nakamura, S.; Hasobe, T. Geometries and Terahertz Motions Driving Quintet Multiexcitons and Ultimate Triplet-Triplet Dissociations via the Intramolecular Singlet Fissions. *J. Phys. Chem. B* **2020,** *124*, 9411-9419.
64. Buckup, T.; Léonard, J. Multidimensional Vibrational Coherence Spectroscopy. *Top. Curr. Chem.* **2018,** *376*, 35.

65. Musser, A. J.; Liebel, M.; Schnedermann, C.; Wende, T.; Kehoe, T. B.; Rao, A.; Kukura, P. Evidence for Conical Intersection Dynamics Mediating Ultrafast Singlet Exciton Fission. *Nat. Phys.* **2015,** *11*, 352-357.
66. Schnedermann, C.; Alvertis, A. M.; Wende, T.; Lukman, S.; Feng, J.; Schröder, F.; Turban, D. H. P.; Wu, J.; Hine, N. D. M.; Greenham, N. C., et al. A molecular movie of ultrafast singlet fission. *Nat. Commun.* **2019,** *10*, 4207.
67. Duan, H. G.; Jha, A.; Li, X.; Tiwari, V.; Ye, H.; Nayak, P. K.; Zhu, X. L.; Li, Z.; Martinez, T. J.; Thorwart, M., et al. Intermolecular vibrations mediate ultrafast singlet fission. *Sci. Adv.* **2020,** *6*.
68. Fuemmeler, E. G.; Sanders, S. N.; Pun, A. B.; Kumarasamy, E.; Zeng, T.; Miyata, K.; Steigerwald, M. L.; Zhu, X. Y.; Sfeir, M. Y.; Campos, L. M., et al. A Direct Mechanism of Ultrafast Intramolecular Singlet Fission in Pentacene Dimers. *ACS Cent. Sci.* **2016,** *2*, 316-24.
69. Bakulin, A. A.; Morgan, S. E.; Kehoe, T. B.; Wilson, M. W. B.; Chin, A. W.; Zigmantas, D.; Egorova, D.; Rao, A. Real-time observation of multiexcitonic states in ultrafast singlet fission using coherent 2D electronic spectroscopy. *Nat. Chem.* **2015,** *8*, 16.
70. Dover, C. B.; Gallaher, J. K.; Frazer, L.; Tapping, P. C.; Petty Ii, A. J.; Crossley, M. J.; Anthony, J. E.; Kee, T. W.; Schmidt, T. W. Endothermic singlet fission is hindered by excimer formation. *Nat. Chem.* **2018,** *10*, 305.
71. Ito, A.; Shimizu, A.; Kishida, N.; Kawanaka, Y.; Kosumi, D.; Hashimoto, H.; Teki, Y. Excited-State Dynamics of Pentacene Derivatives with Stable Radical Substituents. *Angew. Chem.* **2014,** *126*, 6833-6837.
72. Minami, T.; Nakano, M. Diradical Character View of Singlet Fission. *J. Phys. Chem. Lett.* **2011,** *3*, 145-150.
73. Ito, S.; Minami, T.; Nakano, M. Diradical Character Based Design for Singlet Fission of Condensed-Ring Systems with 4nπ Electrons. *J. Phys. Chem. C* **2012,** *116*, 19729-19736.
74. Minami, T.; Ito, S.; Nakano, M. Theoretical Study of Singlet Fission in Oligorylenes. *J. Phys. Chem. Lett.* **2012,** *3*, 2719-23.
75. Minami, T.; Ito, S.; Nakano, M. Fundamental of Diradical-Character-Based Molecular Design for Singlet Fission. *J. Phys. Chem. Lett.* **2013,** *4*, 2133-2137.
76. Ito, S.; Nakano, M. Theoretical Molecular Design of Heteroacenes for Singlet Fission: Tuning the Diradical Character by Modifying π-Conjugation Length and Aromaticity. *J. Phys. Chem. Lett.* **2014,** *119*, 148-157.
77. Ito, S.; Nagami, T.; Nakano, M. Design Principles of Electronic Couplings for Intramolecular Singlet Fission in Covalently-Linked Systems. *J. Phys. Chem. A* **2016,** *120*, 6236-6241.
78. Ito, S.; Nagami, T.; Nakano, M. Diradical Character-Based Design for Singlet Fission of Bisanthene Derivatives: Aromatic-Ring Attachment and pi-Plane Twisting. *J. Phys. Chem. Lett.* **2016,** *7*, 3925-3930.
79. Nagami, T.; Miyamoto, H.; Yoshida, W.; Okada, K.; Tonami, T.; Nakano, M. Theoretical Molecular Design of Phenanthrenes for Singlet Fission by Diazadibora-Substitution. *J. Phys. Chem. A* **2020,** *124*, 6778-6789.
80. Zeng, T.; Ananth, N.; Hoffmann, R. Seeking Small Molecules for Singlet Fission: A Heteroatom Substitution Strategy. *J. Am. Chem. Soc.* **2014,** *136*, 12638-12647.

81. Lopez-Carballeira, D.; Casanova, D.; Ruiperez, F. Theoretical design of conjugated diradicaloids as singlet fission sensitizers: quinones and methylene derivatives. *Phys. Chem. Chem. Phys.* **2017,** *19*, 30227-30238.
82. Messelberger, J.; Grunwald, A.; Pinter, P.; Hansmann, M. M.; Munz, D. Carbene derived diradicaloids - building blocks for singlet fission? *Chem. Sci.* **2018,** *9*, 6107-6117.
83. Eaton, S. W.; Miller, S. A.; Margulies, E. A.; Shoer, L. E.; Schaller, R. D.; Wasielewski, M. R. Singlet exciton fission in thin films of tert-butyl-substituted terrylenes. *J. Phys. Chem. A* **2015,** *119*, 4151-61.
84. Chen, Y.; Shen, L.; Li, X. Effects of heteroatoms of tetracene and pentacene derivatives on their stability and singlet fission. *J. Phys. Chem. A* **2014,** *118*, 5700-8.
85. Günther, B. A. R.; Höfener, S.; Zschieschang, U.; Wadepohl, H.; Klauk, H.; Gade, L. H. Twisting the TAPPs: Bay-Substituted Non-planar Tetraazapero-pyrenes and their Reduced Anions. *Chem. Eur. J.* **2019,** *25*, 14669-14678.
86. Geacintov, N.; Pope, M.; Vogel, F. Effect of Magnetic Field on the Fluorescence of Tetracene Crystals: Exciton Fission. *Phys. Rev. Lett.* **1969,** *22*, 593-596.
87. Clark, P. A.; Brogli, F.; Heilbronner, E. The $\pi$-Orbital Energies of the Acenes. *Helv. Chim. Acta* **1972,** *55*, 1415-1428.
88. Burdett, J. J.; Bardeen, C. J. The dynamics of singlet fission in crystalline tetracene and covalent analogs. *Acc. Chem. Res.* **2013,** *46*, 1312-20.
89. Burdett, J. J.; Gosztola, D.; Bardeen, C. J. The dependence of singlet exciton relaxation on excitation density and temperature in polycrystalline tetracene thin films: kinetic evidence for a dark intermediate state and implications for singlet fission. *J. Chem. Phys.* **2011,** *135*, 214508.
90. Tayebjee, M. J. Y.; Clady, R. G. C. R.; Schmidt, T. W. The exciton dynamics in tetracene thin films. *Phys. Chem. Chem. Phys.* **2013,** *15*, 14797-14805.
91. Wilson, M. W. B.; Rao, A.; Johnson, K.; Gélinas, S.; di Pietro, R.; Clark, J.; Friend, R. H. Temperature-Independent Singlet Exciton Fission in Tetracene. *J. Am. Chem. Soc.* **2013,** *135*, 16680-16688.
92. Jundt, C.; Klein, G.; Sipp, B.; Moigne, J. L.; Joucla, M.; Villaeys, A. A. Exciton Dynamics in Pentacene Thin Films Studied by Pump-Probe Spectroscopy. *Chem. Phys. Lett.* **1995,** *241*, 84-88.
93. Marciniak, H.; Fiebig, M.; Huth, M.; Schiefer, S.; Nickel, B.; Selmaier, F.; Lochbrunner, S. Ultrafast exciton relaxation in microcrystalline pentacene films. *Phys. Rev. Lett.* **2007,** *99*, 176402.
94. Zimmerman, P. M.; Zhang, Z. Y.; Musgrave, C. B. Singlet Fission in Pentacene Through Multi-Exciton Quantum States. *Nat. Chem.* **2010,** *2*, 648-652.
95. Chan, W.-L.; Ligges, M.; Jailaubekov, A.; Kaake, L.; Miaja-Avila, L.; Zhu, X. Y. Observing the Multiexciton State in Singlet Fission and Ensuing Ultrafast Multielectron Transfer. *Science* **2011,** *334*, 1541.
96. Chan, W. L.; Berkelbach, T. C.; Provorse, M. R.; Monahan, N. R.; Tritsch, J. R.; Hybertsen, M. S.; Reichman, D. R.; Gao, J. L.; Zhu, X. Y. The Quantum Coherent Mechanism for Singlet Fission: Experiment and Theory. *Acc. Chem. Res.* **2013,** *46*, 1321-1329.
97. Zimmerman, P. M.; Musgrave, C. B.; Head-Gordon, M. A Correlated Electron View of Singlet Fission. *Acc. Chem. Res.* **2013,** *46*, 1339-1347.

98. Wang, L.; Olivier, Y.; Prezhdo, O. V.; Beljonne, D. Maximizing Singlet Fission by Molecular Packing. *J. Phys. Chem. Lett.* **2014,** *5*, 3345-3353.
99. Sanders, S. N.; Kumarasamy, E.; Pun, A. B.; Trinh, M. T.; Choi, B.; Xia, J.; Taffet, E. J.; Low, J. Z.; Miller, J. R.; Roy, X., et al. Quantitative Intramolecular Singlet Fission in Bipentacenes. *J. Am. Chem. Soc.* **2015,** *137*, 8965-8972.
100. Zirzlmeier, J.; Lehnherr, D.; Coto, P. B.; Chernick, E. T.; Casillas, R.; Basel, B. S.; Thoss, M.; Tykwinski, R. R.; Guldi, D. M. Singlet fission in pentacene dimers. *Proc. Natl. Acad. Sci. U.S.A.* **2015,** *112*, 5325-30.
101. Zirzlmeier, J.; Casillas, R.; Reddy, R.; Coto, P. B.; Lehnherr, D.; Chernick, E. T.; Papadopoulos, I.; Thoss, M.; Tykwinski, R. R.; Guldi, D. M. Solution-Based Intramolecular Singlet Fission in Cross-Conjugated Pentacene Dimers. *Nanoscale* **2016,** *8*, 10113-10123.
102. Garoni, E.; Zirzlmeier, J.; Basel, B. S.; Hetzer, C.; Kamada, K.; Guldi, D. M.; Tykwinski, R. R. Two-Photon Absorption in Pentacene Dimers: The Importance of the Spacer Using Upconversion as an Indirect Route to Singlet Fission. *J. Am. Chem. Soc.* **2017,** *139*, 14017-14020.
103. Trinh, M. T.; Pinkard, A.; Pun, A. B.; Sanders, S. N.; Kumarasamy, E.; Sfeir, M. Y.; Campos, L. M.; Roy, X.; Zhu, X. Y. Distinct properties of the triplet pair state from singlet fission. *Sci. Adv.* **2017,** *3*, e1700241.
104. Wollscheid, N.; Perez Lustres, J. L.; Kefer, O.; Hahn, S.; Brosius, V.; Bunz, U. H. F.; Motzkus, M.; Buckup, T. Oxygen-catalysed sequential singlet fission. *Nat. Commun.* **2019,** *10*, 5202.
105. Stevens, B.; Perez, S. R.; Ors, J. A. Photoperoxidation of unsaturated organic molecules. $O_2$ $^1\Delta_g$ acceptor properties and reactivity. *J. Am. Chem. Soc.* **1974,** *96*, 6846-6850.
106. Maliakal, A.; Raghavachari, K.; Katz, H.; Chandross, E.; Siegrist, T. Photochemical Stability of Pentacene and a Substituted Pentacene in Solution and in Thin Films. *Chem. Mater.* **2004,** *16*, 4980-4986.
107. Wang, X.; Liu, X.; Tom, R.; Cook, C.; Schatschneider, B.; Marom, N. Phenylated Acene Derivatives as Candidates for Intermolecular Singlet Fission. *J. Phys. Chem. C* **2019,** *123*, 5890-5899.
108. Nagami, T.; Tonami, T.; Okada, K.; Yoshida, W.; Miyamoto, H.; Nakano, M. Vibronic coupling density analysis and quantum dynamics simulation for singlet fission in pentacene and its halogenated derivatives. *J. Chem. Phys.* **2020,** *153*, 134302.
109. Hansmann, A. K.; Berger, R. Variation of the Fine-Structure Constant in Model Systems for Singlet Fission. *J. Phys. Chem. A* **2020,** *124*, 6682-6687.
110. Pensack, R. D.; Tilley, A. J.; Parkin, S. R.; Lee, T. S.; Payne, M. M.; Gao, D.; Jahnke, A. A.; Oblinsky, D. G.; Li, P. F.; Anthony, J. E., et al. Exciton delocalization drives rapid singlet fission in nanoparticles of acene derivatives. *J. Am. Chem. Soc.* **2015,** *137*, 6790-803.
111. Han, J.; Rehn, D. R.; Buckup, T.; Dreuw, A. Evaluation of Single-Reference DFT-Based Approaches for the Calculation of Spectroscopic Signatures of Excited States Involved in Singlet Fission. *J. Phys. Chem. A* **2020,** *124*, 8446-8460.
112. Greene, M., Perylene Pigments. In *High Performance Pigments*, 2009; pp 261-274.
113. Huang, C.; Barlow, S.; Marder, S. R. Perylene-3,4,9,10-tetracarboxylic acid diimides: synthesis, physical properties, and use in organic electronics. *J. Org. Chem.* **2011,** *76*, 2386-407.

114. Weil, T.; Vosch, T.; Hofkens, J.; Peneva, K.; Müllen, K. The rylene colorant family--tailored nanoemitters for photonics research and applications. *Angew. Chem. Int. Ed.* **2010,** *49*, 9068-93.
115. Usta, H.; Facchetti, A.; Marks, T. J. n-Channel semiconductor materials design for organic complementary circuits. *Acc. Chem. Res.* **2011,** *44*, 501-10.
116. Eaton, S. W.; Shoer, L. E.; Karlen, S. D.; Dyar, S. M.; Margulies, E. A.; Veldkamp, B. S.; Ramanan, C.; Hartzler, D. A.; Savikhin, S.; Marks, T. J., et al. Singlet exciton fission in polycrystalline thin films of a slip-stacked perylenediimide. *J. Am. Chem. Soc.* **2013,** *135*, 14701-12.
117. Hahn, L.; Maaß, F.; Bleith, T.; Zschieschang, U.; Wadepohl, H.; Klauk, H.; Tegeder, P.; Gade, L. H. Core Halogenation as a Construction Principle in Tuning the Material Properties of Tetraazaperopyrenes. *Chem. Eur. J.* **2015,** *21*, 17691-700.
118. Müller, A. M.; Avlasevich, Y. S.; Müllen, K.; Bardeen, C. J. Evidence for exciton fission and fusion in a covalently linked tetracene dimer. *Chem. Phys. Lett.* **2006,** *421*, 518 - 522.
119. Müller, A. M.; Avlasevich, Y. S.; Schoeller, W. W.; Müllen, K.; Bardeen, C. J. Exciton fission and fusion in bis(tetracene) molecules with different covalent linker structures. *J. Am. Chem. Soc.* **2007,** *129*, 14240-50.
120. Hetzer, C.; Guldi, D. M.; Tykwinski, R. R. Pentacene Dimers as a Critical Tool for the Investigation of Intramolecular Singlet Fission. *Chem. Eur. J.* **2018,** *24*, 8245-8257.
121. Busby, E.; Xia, J.; Wu, Q.; Low, J. Z.; Song, R.; Miller, J. R.; Zhu, X.-Y.; Campos, Luis M.; Sfeir, M. Y. A Design Strategy for Intramolecular Singlet Fission Mediated by Charge-Transfer States in Donor-Acceptor Organic Materials. *Nat. Mater.* **2015,** *14*, 426-433.
122. Lukman, S.; Musser, A. J.; Chen, K.; Athanasopoulos, S.; Yong, C. K.; Zeng, Z.; Ye, Q.; Chi, C.; Hodgkiss, J. M.; Wu, J., et al. Tuneable Singlet Exciton Fission and Triplet–Triplet Annihilation in an Orthogonal Pentacene Dimer. *Adv. Funct. Mater.* **2015,** *25*, 5452-5461.
123. Basel, B. S.; Zirzlmeier, J.; Hetzer, C.; Reddy, S. R.; Phelan, B. T.; Krzyaniak, M. D.; Volland, M. K.; Coto, P. B.; Young, R. M.; Clark, T., et al. Evidence for Charge-Transfer Mediation in the Primary Events of Singlet Fission in a Weakly Coupled Pentacene Dimer. *Chem* **2018,** *4*, 1092-1111.
124. Korovina, N. V.; Das, S.; Nett, Z.; Feng, X.; Joy, J.; Haiges, R.; Krylov, A. I.; Bradforth, S. E.; Thompson, M. E. Singlet Fission in a Covalently Linked Cofacial Alkynyltetracene Dimer. *J. Am. Chem. Soc.* **2016,** *138*, 617-627.
125. Wang, L.; Bai, S.; Wu, Y.; Liu, Y.; Yao, J.; Fu, H. Revealing the Nature of Singlet Fission under the Veil of Internal Conversion. *Angew. Chem. Int. Ed.* **2020,** *59*, 2003-2007.
126. Wu, Y.; Wang, Y.; Chen, J.; Zhang, G.; Yao, J.; Zhang, D.; Fu, H. Intramolecular Singlet Fission in an Antiaromatic Polycyclic Hydrocarbon. *Angew. Chem. Int. Ed.* **2017,** *56*, 9400-9404.
127. Korovina, N. V.; Chang, C. H.; Johnson, J. C. Spatial separation of triplet excitons drives endothermic singlet fission. *Nat. Chem.* **2020,** *12*, 391-398.
128. Yamakado, T.; Takahashi, S.; Watanabe, K.; Matsumoto, Y.; Osuka, A.; Saito, S. Conformational Planarization versus Singlet Fission: Distinct Excited-State Dynamics of Cyclooctatetraene-Fused Acene Dimers. *Angew. Chem. Int. Ed.* **2018,** *57*, 5438-5443.

129. Pun, A. B.; Sanders, S. N.; Kumarasamy, E.; Sfeir, M. Y.; Congreve, D. N.; Campos, L. M. Triplet Harvesting from Intramolecular Singlet Fission in Polytetracene. *Adv. Mater.* **2017,** *29*.
130. Hu, J.; Xu, K.; Shen, L.; Wu, Q.; He, G.; Wang, J. Y.; Pei, J.; Xia, J.; Sfeir, M. Y. New insights into the design of conjugated polymers for intramolecular singlet fission. *Nat. Commun.* **2018,** *9*, 2999.
131. Musser, A. J.; Al-Hashimi, M.; Heeney, M.; Clark, J. Heavy-atom effects on intramolecular singlet fission in a conjugated polymer. *J. Chem. Phys.* **2019,** *151*, 044902.
132. Pace, N. A.; Zhang, W.; Arias, D. H.; McCulloch, I.; Rumbles, G.; Johnson, J. C. Controlling Long-Lived Triplet Generation from Intramolecular Singlet Fission in the Solid State. *J. Phys. Chem. Lett.* **2017,** *8*, 6086-6091.
133. Wang, L.; Liu, X.; Shi, X.; Anderson, C. L.; Klivansky, L. M.; Liu, Y.; Wu, Y.; Chen, J.; Yao, J.; Fu, H. Singlet Fission in a para-Azaquinodimethane-Based Quinoidal Conjugated Polymer. *J. Am. Chem. Soc.* **2020,** *142*, 17892-17896.
134. Wohlgenannt, M.; Graupner, W.; Österbacka, R.; Leising, G.; Comoretto, D.; Vardeny, Z. V. Singlet Fission in Luminescent and Nonluminescent $\pi$-conjugated Polymers. *Synth. Met.* **1999,** *101*, 267-268.
135. Valentine, D. J.; Manawadu, D.; Barford, W. Higher-energy triplet-pair states in polyenes and their role in intramolecular singlet fission. *Phys. Rev. B* **2020,** *102*.
136. Kasai, Y.; Tamai, Y.; Ohkita, H.; Benten, H.; Ito, S. Ultrafast Singlet Fission in a Push-Pull Low-Bandgap Polymer Film. *J. Am. Chem. Soc.* **2015,** *137*, 15980-3.
137. Geib, S.; Zschieschang, U.; Gsänger, M.; Stolte, M.; Würthner, F.; Wadepohl, H.; Klauk, H.; Gade, L. H. Core-Brominated Tetraazaperopyrenes as n-Channel Semiconductors for Organic Complementary Circuits on Flexible Substrates. *Adv. Funct. Mater.* **2013,** *23*, 3866-3874.
138. Martens, S. C.; Zschieschang, U.; Wadepohl, H.; Klauk, H.; Gade, L. H. Tetrachlorinated tetraazaperopyrenes (TAPPs): highly fluorescent dyes and semiconductors for air-stable organic n-channel transistors and complementary circuits. *Chem. Eur. J.* **2012,** *18*, 3498-509.
139. Hahn, L.; Wadepohl, H.; Gade, L. H. Tetralithiated tetraazaperopyrene as a key intermediate for the synthesis of functionalized derivatives. *Org. Lett.* **2015,** *17*, 2266-9.
140. Lindner, B. D.; Paulus, F.; Appleton, A. L.; Schaffroth, M.; Engelhart, J. U.; Schelkle, K. M.; Tverskoy, O.; Rominger, F.; Hamburger, M.; Bunz, U. H. F. Electron-transporting phenazinothiadiazoles with engineered microstructure. *J. Mater. Chem. C* **2014,** *2*, 9609-9612.
141. Pisula, W.; Menon, A.; Stepputat, M.; Lieberwirth, I.; Kolb, U.; Tracz, A.; Sirringhaus, H.; Pakula, T.; Müllen, K. A Zone-Casting Technique for Device Fabrication of Field-Effect Transistors Based on Discotic Hexa-peri-hexabenzocoronene. *Adv. Mater.* **2005,** *17*, 684-689.
142. Birks, J. B., *Photophysics of aromatic molecules*. Wiley-Interscience: London, 1970.
143. Lessing, H. E.; Von Jena, A. Separation of rotational diffusion and level kinetics in transient absorption spectroscopy. *Chem. Phys. Lett.* **1976,** *42*, 213-217.
144. Einstein, A. Zur Quantentheorie der Strahlung. *Phys. Z.* **1917,** *18*, 121.

145. Lorenc, M.; Ziolek, M.; Naskrecki, R.; Karolczak, J.; Kubicki, J.; Maciejewski, A. Artifacts in femtosecond transient absorption spectroscopy. *Appl. Phys. B* **2002,** *74*, 19-27.
146. Buckup, T.; Weigel, A.; Hauer, J.; Motzkus, M. Ultrafast multiphoton transient absorption of beta-carotene. *Chem. Phys.* **2010,** *373*, 38-44.
147. Rasmusson, M.; Tarnovsky, A. N.; Åkesson, E.; Sundström, V. On the use of two-photon absorption for determination of femtosecond pump–probe cross-correlation functions. *Chem. Phys. Lett.* **2001,** *335*, 201-208.
148. Deàk, J. C.; Iwaki, L. K.; Dlott, D. D. Vibrational Energy Redistribution in Polyatomic Liquids: Ultrafast IR−Raman Spectroscopy of Acetonitrile. *J. Phys. Chem. A* **1998,** *102*, 8193-8201.
149. Bonneau, R.; Wirz, J.; Zuberbühler, A. D. Methods for the analysis of transient absorbance data (Technical Report). *Pure Appl. Chem.* **1997,** *69*, 979-992.
150. Ruckebusch, C.; Sliwa, M.; Pernot, P.; de Juan, A.; Tauler, R. Comprehensive data analysis of femtosecond transient absorption spectra: A review. *J. Photochem. Photobiol., C* **2012,** *13*, 1-27.
151. Hahn, L.; Hermannsdorfer, A.; Günther, B.; Wesp, T.; Bühler, B.; Zschieschang, U.; Wadepohl, H.; Klauk, H.; Gade, L. H. (Oligo-)Thiophene Functionalized Tetraazaperopyrenes: Donor-Acceptor Dyes and Ambipolar Organic Semiconductors. *J. Org. Chem.* **2017,** *82*, 12492-12502.
152. Hahn, L.; Öz, S.; Wadepohl, H.; Gade, L. H. Highly emissive water-soluble tetraazaperopyrenes as fluorescent markers. *Chem. Commun.* **2014,** *50*, 4941-3.
153. Geib, S.; Martens, S. C.; Marken, M.; Rybina, A.; Wadepohl, H.; Gade, L. H. Tuning redox chemistry and photophysics in core-substituted tetraazaperopyrenes (TAPPs). *Chem. Eur. J.* **2013,** *19*, 13811-22.
154. Höfener, S.; Günther, B. A. R.; Harding, M. E.; Gade, L. H. Understanding UV-Vis Spectra of Halogenated Tetraazaperopyrenes (TAPPs): A Computational Study. *J. Phys. Chem. A* **2019,** *123*, 3160-3169.
155. Wollscheid, N.; Günther, B.; Rao, V. J.; Berger, F. J.; Lustres, J. L. P.; Motzkus, M.; Zaumseil, J.; Gade, L. H.; Hofener, S.; Buckup, T. Ultrafast Singlet Fission and Intersystem Crossing in Halogenated Tetraazaperopyrenes. *J. Phys. Chem. A* **2020**.
156. Wenzel, U.; Löhmannsröben, H. G. Photophysical and fluorescence quenching properties of peropyrene in solution. *J. Photochem. Photobiol., A* **1996,** *96*, 13-18.
157. Kasha, M. Characterization of electronic transitions in complex molecules. *Discuss. Faraday Soc.* **1950,** *9*.
158. Foggi, P.; Pettini, L.; Santa, I.; Righini, R.; Califano, S. Transient absorption and vibrational relaxation dynamics of the lowest excited singlet state of pyrene in solution. *J. Phys. Chem.* **1995,** *99*, 7439-7445.
159. Würthner, F.; Kaiser, T. E.; Saha-Möller, C. R. J-Aggregates: From Serendipitous Discovery to Supramolecular Engineering of Functional Dye Materials. *Angew. Chem. Int. Ed.* **2011,** *50*, 3376-410.
160. Zewail, A. H. Optical molecular dephasing: principles of and probings by coherent laser spectroscopy. *Acc. Chem. Res.* **1980,** *13*, 360-368.
161. Kraack, J. P.; Wand, A.; Buckup, T.; Motzkus, M.; Ruhman, S. Mapping multidimensional excited state dynamics using pump-impulsive-vibrational-spectroscopy and pump-degenerate-four-wave-mixing. *Phys. Chem. Chem. Phys.* **2013,** *15*, 14487-14501.

162. Kraack, J. P. *Multi-Dimensional Ultrafast Spectroscopy of Vibrational Coherence Dynamics in Excited Electronic States of Polyenes.* Dissertation, Universität Heidelberg, Heidelberg, 2013.
163. Vura-Weis, J.; Ratner, M. A.; Wasielewski, M. R. Geometry and electronic coupling in perylenediimide stacks: mapping structure-charge transport relationships. *J. Am. Chem. Soc.* **2010,** *132*, 1738-9.
164. Quarti, C.; Fazzi, D.; Del Zoppo, M. A computational investigation on singlet and triplet exciton couplings in acene molecular crystals. *Phys. Chem. Chem. Phys.* **2011,** *13*, 18615-25.
165. Schubert, A.; Settels, V.; Liu, W.; Würthner, F.; Meier, C.; Fink, R. F.; Schindlbeck, S.; Lochbrunner, S.; Engels, B.; Engel, V. Ultrafast Exciton Self-Trapping upon Geometry Deformation in Perylene-Based Molecular Aggregates. *J. Phys. Chem. Lett.* **2013,** *4*, 792-6.
166. Ye, C.; Gray, V.; Martensson, J.; Börjesson, K. Annihilation Versus Excimer Formation by the Triplet Pair in Triplet-Triplet Annihilation Photon Upconversion. *J. Am. Chem. Soc.* **2019,** *141*, 9578-9584.
167. Braun, M.; Sobotta, C.; Dürr, R.; Pulvermacher, H.; Malkmus, S. Analysis of wave packet motion in frequency and time domain: oxazine 1. *J. Phys. Chem. A* **2006,** *110*, 9793-800.
168. Furube, A.; Murai, M.; Tamaki, Y.; Watanabe, S.; Katoh, R. Effect of aggregation on the excited-state electronic structure of perylene studied by transient absorption spectroscopy. *J. Phys. Chem. A* **2006,** *110*, 6465-71.
169. Kautsky, H. Quenching of luminescence by oxygen. *Trans. Faraday Soc.* **1939,** *35*.
170. Ware, W. R. Oxygen Quenching of Fluorescence in Solution: An Experimental Study of the Diffusion Process. *J. Phys. Chem.* **1962,** *66*, 455-458.
171. Lakowicz, J. R.; Weber, G. Quenching of fluorescence by oxygen. A probe for structural fluctuations in macromolecules. *Biochemistry* **1973,** *12*, 4161-70.
172. Reddy, A. R.; Bendikov, M. Diels-Alder reaction of acenes with singlet and triplet oxygen -- theoretical study of two-state reactivity. *Chem. Commun.* **2006**, 1179-81.
173. Chien, S. H.; Cheng, M. F.; Lau, K. C.; Li, W. K. Theoretical study of the Diels-Alder reactions between singlet ($^1\Delta_g$) oxygen and acenes. *J. Phys. Chem. A* **2005,** *109*, 7509-18.
174. Li, A.; Tang, S.; Tan, P.; Liu, C.; Liang, B. Measurement and Prediction of Oxygen Solubility in Toluene at Temperatures from 298.45 K to 393.15 K and Pressures up to 1.0 MPa. *J. Chem. Eng. Data* **2007,** *52*, 2339-2344.
175. Luehring, P.; Schumpe, A. Gas solubilities (hydrogen, helium, nitrogen, carbon monoxide, oxygen, argon, carbon dioxide) in organic liquids at 293.2 K. *J. Chem. Eng. Data* **1989,** *34*, 250-252.
176. Quaranta, M.; Murkovic, M.; Klimant, I. A new method to measure oxygen solubility in organic solvents through optical oxygen sensing. *Analyst* **2013,** *138*, 6243-5.
177. Smoluchowski, M. v., Versuch einer mathematischen Theorie der Koagulationskinetik kolloider Lösungen. In *Z. Phys. Chem.*, 1918; Vol. 92U, p 129.
178. Aminabhavi, T. M.; Gopalakrishna, B. Density, Viscosity, Refractive Index, and Speed of Sound in Aqueous Mixtures of N,N-Dimethylformamide, Dimethyl Sulfoxide, N,N-Dimethylacetamide, Acetonitrile, Ethylene Glycol, Diethylene Glycol, 1,4-Dioxane, Tetrahydrofuran, 2-Methoxyethanol, and 2-Ethoxyethanol at 298.15 K. *J. Chem. Eng. Data* **1995,** *40*, 856-861.

179. Wollscheid, N.; Lustres, J. L. P.; Brosius, V.; Motzkus, M.; Bunz, U. H. F.; Buckup, T. Diffusion-Controlled Singlet Fission in a Chlorinated Phenazinothiadiazole by Broadband Femtosecond Transient Absorption. *J. Phys. Chem. B* **2020**.
180. Gijzeman, O. L. J.; Kaufman, F.; Porter, G. Oxygen quenching of aromatic triplet states in solution. Part 1. *J. Chem. Soc., Faraday Trans. 2* **1973,** *69*, 708-720.
181. Field, L. R.; Wilhelm, E.; Battino, R. The solubility of gases in liquids 6. Solubility of $N_2$, $O_2$, CO, $CO_2$, $CH_4$, and $CF_4$ in methylcyclohexane and toluene at 283 to 313 K. *J. Chem. Thermodyn.* **1974,** *6*, 237-243.
182. Krall, A. H.; Sengers, J. V.; Kestin, J. Viscosity of liquid toluene at temperatures from 25 to 150.degree.C and at pressures up to 30 MPa. *J. Chem. Eng. Data* **1992,** *37*, 349-355.
183. Ogilby, P. R.; Foote, C. S. Chemistry of singlet oxygen. Effect of solvent, solvent isotopic substitution, and temperature on the lifetime of singlet molecular oxygen ($^1\Delta_g$ ). *J. Am. Chem. Soc.* **1983,** *105*, 3423-3430.
184. Grancini, G.; Polli, D.; Fazzi, D.; Cabanillas-Gonzalez, J.; Cerullo, G.; Lanzani, G. Transient Absorption Imaging of P3HT:PCBM Photovoltaic Blend: Evidence For Interfacial Charge Transfer State. *J. Phys. Chem. Lett.* **2011,** *2*, 1099-1105.

# Appendix

## A. Global Multiexponential Fit Including the Coherent Artefact

As shown in Eq. 8, the physical description of coherent contributions to the TA signal requires three fitting parameters, *i.e.*, time-zero $t_0$, instrument response $\sigma$ and group velocity dispersion $\tau_{\mathrm{GVD}}$. Of those three, only $\tau_{\mathrm{GVD}}$ exhibits a wavelength dependence, meaning that one parameter is required per wavelength. This would significantly increase the computational requirements and the risk of overfitting emerges. In order to address this problem, the CA is modelled mathematically as the sum of a Gaussian and its first five derivatives:

$$g = e^{-\left(\frac{t-t_0}{2\sigma}\right)^2} \qquad \text{Eq. A1}$$

$$g' = -\frac{1}{\sigma^2}\,(t-t_0)\,g_0 \qquad \text{Eq. A2}$$

$$g'' = -\frac{t}{\sigma^2}\,(g_0 + (t-t_0)g_1) \qquad \text{Eq. A3}$$

$$g''' = -\frac{t}{\sigma^2}\,(2g_1 + (t-t_0)g_2) \qquad \text{Eq. A4}$$

$$g^{IV} = -\frac{t}{\sigma^2}\,(3g_2 + (t-t_0)g_3) \qquad \text{Eq. A5}$$

$$g^{V} = -\frac{t}{\sigma^2}\,(4g_3 + (t-t_0)g_4) \qquad \text{Eq. A6}$$

$$\Delta A_{\mathrm{coh}} = b_0 g + b_1 g' + b_2 g'' + b_3 g''' + b_4 g^{IV} + b_5 g^{V} \qquad \text{Eq. A7}$$

Thus, coherent contributions can be modelled using only $t_0$ and $\sigma$ as fitting parameters, which are shared with the fit of the sequential contribution. Using this approach, the TA signal of a single wavelength with $n$ exponential decays is given as

$$\Delta A(t) = \sum_{i=1}^{n} a_i \cdot e_i = (b_0 \cdots b_5 \;\; a_1 \;\; a_2 \;\; \cdots \;\; a_n) \begin{pmatrix} g \\ \vdots \\ g^V \\ e_1 \\ e_2 \\ \vdots \\ e_n \end{pmatrix} = \vec{a} \cdot \vec{e} \qquad \text{Eq. A8}$$

Consequently, the 2D TA data spanning $w$ wavelengths, $n$ decays, and $T$ probe delays is described as (*cf.* section 3.3.3)

$$\mathbf{TA} = \sum_{i=1}^{n} \sum_{j=1}^{w} \sum_{l=1}^{T} a_{j,i} \cdot e_{i,l}$$

$$= \begin{pmatrix} b_{1,0} & \cdots & b_{5,1} & a_{1,1} & \cdots & a_{1,n} \\ \vdots & \ddots & \vdots & \vdots & \ddots & \vdots \\ b_{w,0} & \cdots & b_{w,5} & a_{w,1} & \cdots & a_{w,n} \end{pmatrix} \begin{pmatrix} g_{0,1} & \cdots & g_{0,T} \\ \vdots & \ddots & \vdots \\ g_{5,1} & \cdots & g_{5,T} \\ e_{1,1} & \cdots & e_{1,T} \\ \vdots & \ddots & \vdots \\ e_{n,1} & \cdots & e_{n,T} \end{pmatrix} \qquad \text{Eq. A9}$$

DADS and time-dependent concentrations required for the interpretation of the kinetic model can be obtained as the columns and rows of the respective matrices.

# B. Intersystem Crossing in Dilute Solutions of TAPP-X

## B.1 Solvent Effects on Absorption and Emission Spectra of TAPP-X

Polar solvents allow for a stabilisation CT states. Thus, investigating the location of absorption and emission maxima for solvents with varying polarities allow for an estimation of CT character in the excited and/or ground state to be made. In the case of TAPP-X, no systematic trends are observed over a broad range of solvent polarity (Figure A1). In combination with the high symmetry of TAPP-X, it can be concluded that CT contributions are equally weak in both ground and excited state.

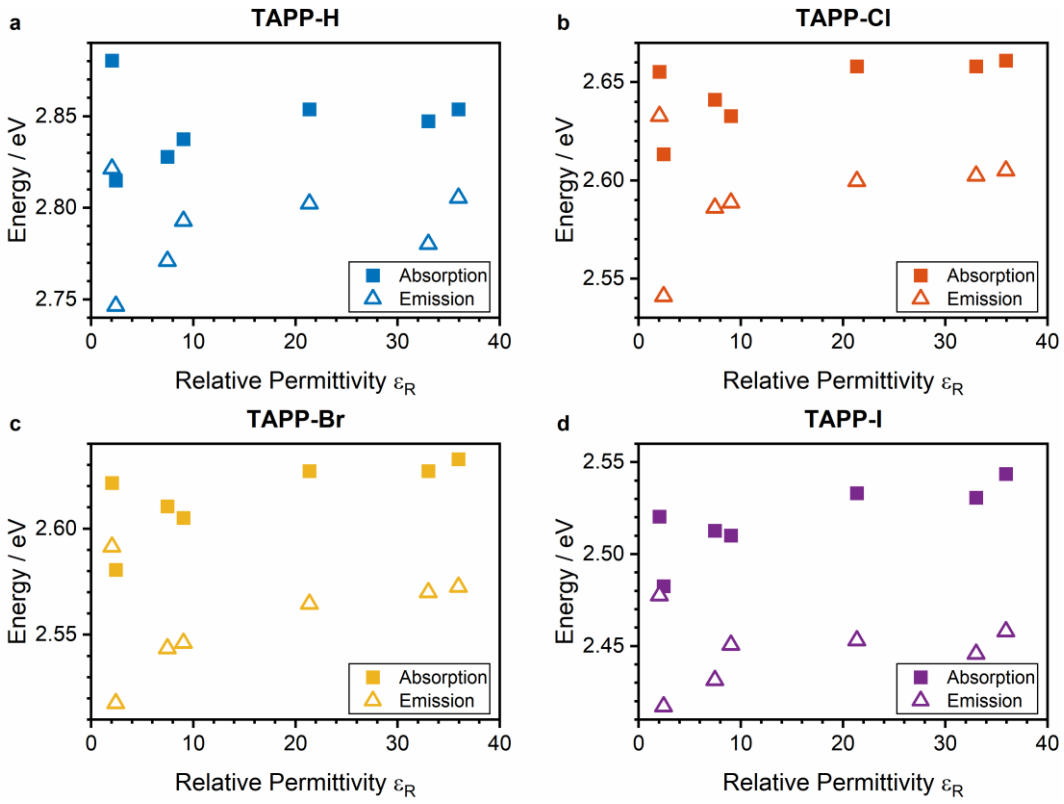


***Figure A1**: The absorption and emission maxima for a) TAPP-H, b) TAPP-Cl, c) TAPP-Br and d) TAPP-I show no systematic change with regard to solvent polarity. Thus, it is concluded that both $S_0$ and $S_1$ are od an equally nonpolar nature.*

## B.2 Time-Resolved Emission of TAPP-X

The time-resolved emission of TAPP-X shows a monoexponential decay for all four compounds (Figure A2). Fitting the emission decay yields similar time constants $\tau_{Em}$ for TAPP-H and TAPP-Cl (Table A1). In turn, upon increasing the substituent size, a significant decrease of the time constant from 2.32 ns (TAPP-Cl) to 48 ps (TAPP-I) is observed. For further analysis, the reported values for the fluorescence quantum yield[117] are used to extract a radiative ($\tau_{rad}$) and non-radiative component ($\tau_{nonrad}$). A comparison with the literature shows a good agreement for TAPP-Cl and TAPP-Br and deviations for TAPP-H and TAPP-I. For the latter, this is attributed to the low quantum yield, as small errors in its detection propagate to large deviations of lifetimes due to the reciprocal relation between both quantities. In addition, the emission decay is close to the resolution limit of the experimental setup, making it prone to error. The deviation observed for TAPP-H most likely originates from the difference in the properties of solvent used. Intriguingly, while the solvent does not affect the stationary spectra, the emission decay for TAPP-H is accelerated by about one third from 3.1 ns to 2.1 ns in THF[117] and acetonitrile, respectively. This suggests that radiative and non-radiative decay channels are affected by the solvent to a varying extent. In contrast, the different solvent has almost no effect on the time constants for TAPP-Cl and TAPP-Br.

***Table A1:*** *Emission lifetimes of TAPP-X in acetonitrile and reported with derived radiative and non-radiative time constants.*

| Chromophore | $\tau_{Em}$ / ps | $\Phi_{Em}$[117] | $\tau_{rad}$ / ns | $\tau_{nonrad}$ / ns |
|---|---|---|---|---|
| **TAPP-H** | 2142 ± 3 | 0.51 | 4.20 | 4.37 |
| **TAPP-Cl** | 2326 ± 3 | 0.78 | 2.98 | 10.6 |
| **TAPP-Br** | 362 ± 6 | 0.12 | 3.02 | 0.41 |
| **TAPP-I** | 48 ± 1 | 0.02 | 2.40 | 0.05 |

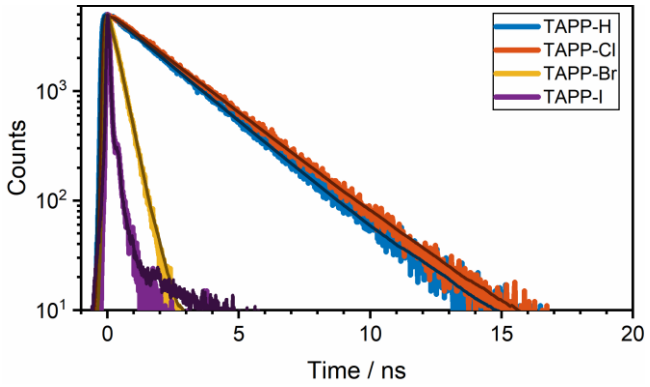


***Figure A2:*** *Time-resolved emission traces of TAPP-X at their respective emission maxima with monoexponential fit traces. While TAPP-H and TAPP-Cl exhibit almost the same decay time, a systematic increase of the decay is observed upon increasing the size of the halide substituent. All samples were excited at 375 nm.*

## B.3 Long-Time Dynamics of Dilute TAPP-X Solutions

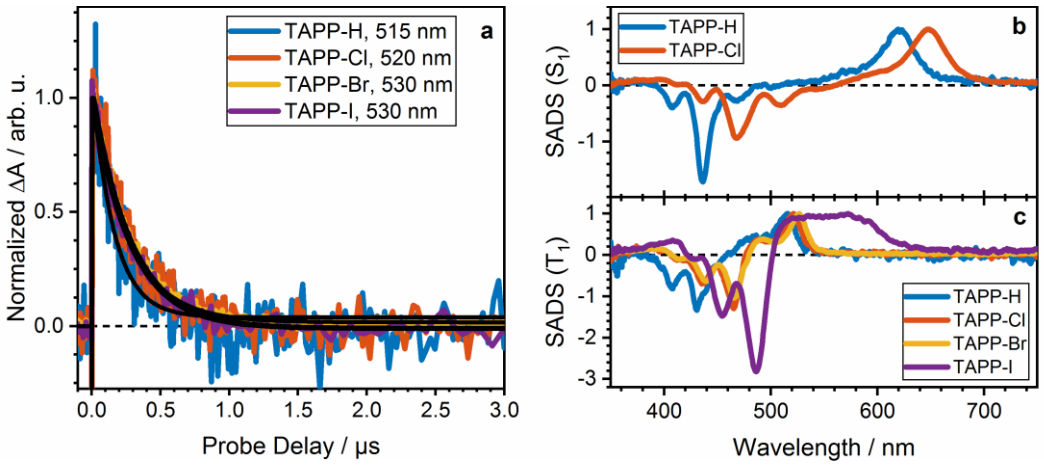


***Figure A3:*** *a) Normalized long-time transients at indicated wavelengths with biexponential (TAPP-H and TAPP-Cl) and monoexponential (TAPP-Br, TAPP-I) fit traces for TAPP-X in acetonitrile. b) Normalised $S_1$ SADS for TAPP-H and TAPP-Cl obtained by applying a sequential model. c) Normalised $T_1$ SADS obtained by applying a sequential model.*

# C. Coherent Triplet Formation in Halogenated Tetraazaperopyrenes

## C.1 Long-Time Dynamics of TAPP-Br Thin Films

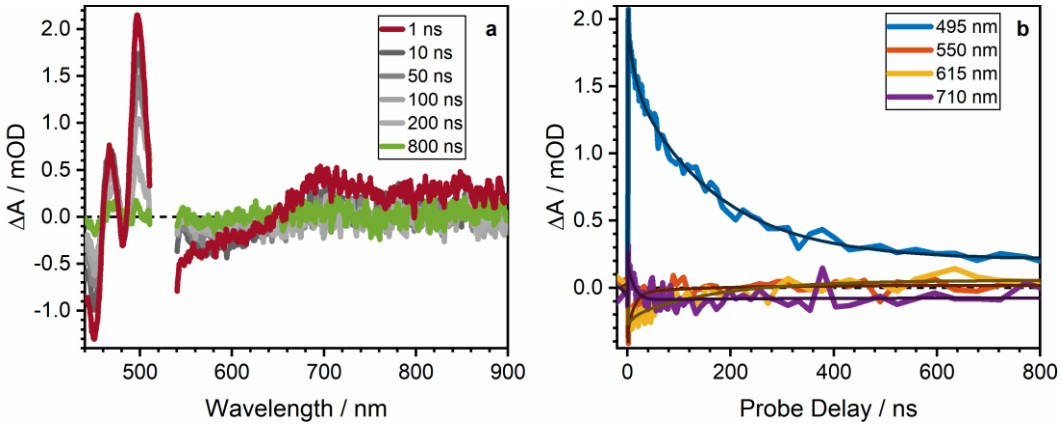


***Figure A4:*** *The a) transient spectra and b) transients at selected probe wavelengths for the long-time TA measurements of TAPP-Br show a homogeneous, biexponential decay of the narrow ESA band.*

## C.2 Periodic Oscillations in Selected Transients

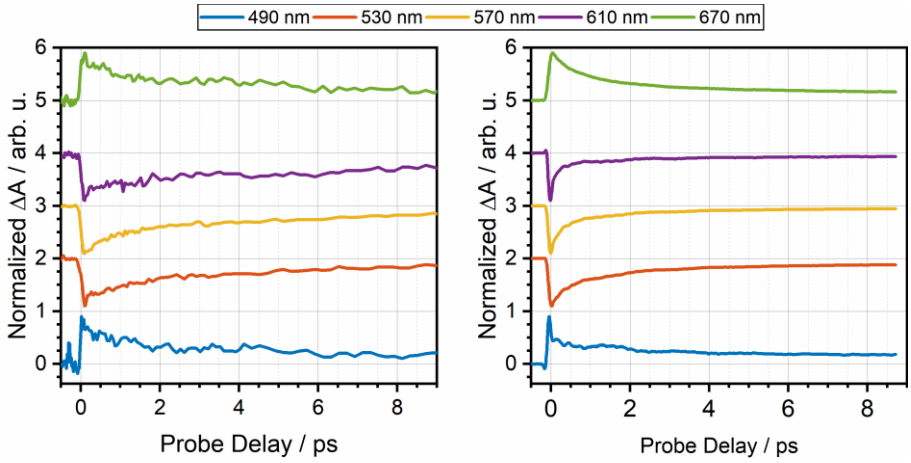


***Figure A5:*** *Periodic oscillations observed in selected transients of a) TAPP-Cl and b) TAPP-Br thin films. Transients are normalized to enhance the visibility of oscillatory features. In both molecules, oscillations are most pronounced around the excitation wavelength (515 and 520 nm for TAPP-Cl and TAPP-Br, respectively). In general, a more intense signal is observed for TAPP-Br compared to TAPP-Cl.*

***Table A2:*** *Results of the exponential decay fit of the TAPP-Br transient at a probe wavelength of 495 nm.*

| **σ / fs** | **$\tau_{dec}$ / ps** | **Amplitude (Decay)** | **Amplitude (Offset)** |
|---|---|---|---|
| 104 | 1.88 | 1.73 | 0.89 |

***Table A3:*** *Results of the coherent artefact parameters of the of the TAPP-Br transient at a probe wavelength of 495 nm.*

| **$\tau_{GVD}$ / fs** | **$\tau_{SRA}$ / fs** | **Amplitude (CPM)** | **Amplitude (SRA)** |
|---|---|---|---|
| 77 | **120** | **47.8** | **1.93** |

***Table A4:*** *Results of the oscillatory components of the TAPP-Br transient at a probe wavelength of 495 nm.*

| **$\tilde{\nu}$ / cm$^{-1}$** | **19.9 ± 0.1** | **52.5 ± 0.4** | **126 ± 1** | **143 ± 1** | **206 ± 2** |
|---|---|---|---|---|---|
| **$k_{dep}$ / $10^{10}$ s$^{-1}$** | 36.6 ± 2.0 | 60.2 ± 7.3 | 71.4 ± 9.7 | 76.9 ± 23.7 | 49.8 ± 29.7 |
| **$\Phi$ / π** | 0.52 ± 0.01 | 0.46 ± 0.03 | 0.29 ± 0.06 | 0.29 ± 0.11 | 0.00 ± 0.14 |
| **Amplitude** | 0.27 | 0.12 | 0.14 | 0.07 | 0.02 |
| **Rel. Amplitude** | 1.00 | 0.44 | 0.53 | 0.25 | 0.08 |

## C.3 Excitation Intensity Dependence

If two excited singlets, $S_1$ are generated in close vicinity, a mutual annihilation resulting in $S_n$ and $S_0$ may occur. This process known as singlet-singlet-annihilation (SSA) can significantly reduce the number of excited chromophores in the sample. SSA can be identified by variations of the excitation intensity. As it directly correlates with the density of excited states, a high excitation intensity should result in a faster decay of the initially photoexcited state if SSA is present. As shown in Figure A6, this effect is observed in TAPP-Br thin film, demonstrating the presence of SSA.

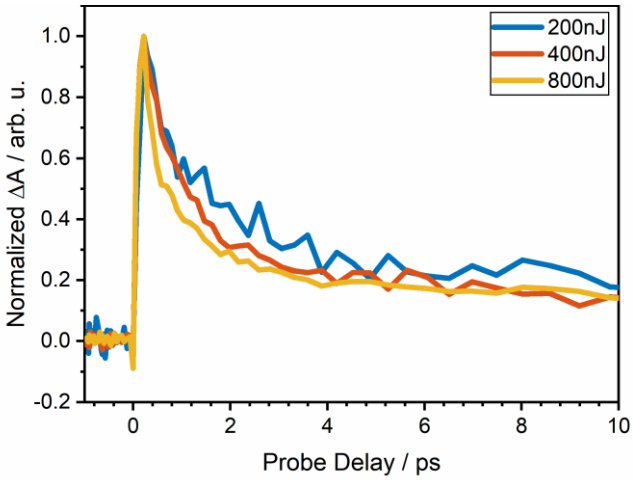


***Figure A6:*** *Normalized transients of a TAPP-Br thin film at 660 nm probe wavelength for varying pump pulse energies. The transients show an acceleration of the initial decay with increasing pump pulse energy.*

## C.4 Pulse Characterisation of the IVS-Experiment

The IVS experiment carried out for dilute solutions of TAPP-Br in acetonitrile uses a different setup as described in section 3.2.2. It contains two home-built non-collinear optical parametric amplifiers (NOPA), which generate pump- and probe pulses, respectively. Spectra and autocorrelations of both NOPA outputs with respective FWHM are depicted in Figure A7.

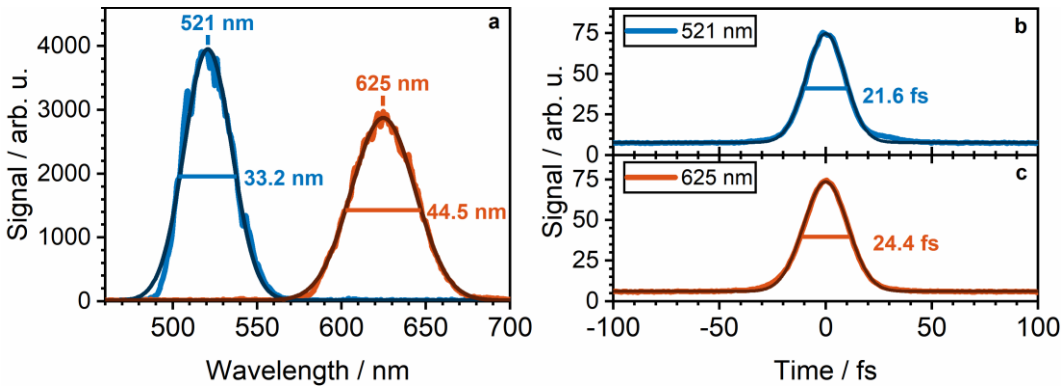


***Figure A7**: Pulse characterisation of the two home-built NOPAs used for the IVS experiment.*

# D. Oxygen-Catalysed Triplet Formation in Acenes

## D.1 Tabulated Time Constants

***Table A5:*** *Tabulated time constants for TIPS-Pn in THF at varying concentrations. Obtained by global multiexponential fits of TA data.*

| Concentration /mM | $\tau_1$ / ns | $\tau_2$ / ns | $\tau_3$ / µs |
|---|---|---|---|
| 0.02 | 11.5 ± 0.1 | n.a. | 2.02 ± 0.09 |
| 0.10 | 10.6 ± 0.1 | 559 ± 45 | 1.53 ± 0.06 |
| 0.16 | 11.9 ± 0.1 | 550 ± 39 | 1.51 ± 0.05 |
| 0.50 | 12.3 ± 0.1 | 242 ± 4 | 1.88 ± 0.01 |
| 0.50[a] | 14.9 ± 0.1 | n.a. | 2.83 ± 0.05 |
| 0.60 | 11.5 ± 0.1 | 108 ± 4 | 1.39 ± 0.01 |
| 1.00 | 12.1 ± 0.1 | 53.7 ± 0.1 | 1.30 ± 0.01 |
| 1.00[a] | 15.0 ± 0.1 | n.a. | n.a. |
| 1.50 | 11.7 ± 0.1 | 51.3 ± 1.3 | 1.35 ± 0.01 |
| 1.50[b] | 8.34 ± 0.1 | 49.2 ± 1.0 | 0.52 ± 0.01 |
| 6.00 | 10.7 ± 0.3 | 20.9 ± 1.5 | 1.46 ± 0.01 |
| 10.0 | 7.54 ± 0.06 | n.a. | 1.29 ± 0.01 |
| 13.0 | 8.61 ± 0.07 | n.a. | 1.53 ± 0.01 |
| 15.0 | 6.70 ± 0.06 | n.a. | 1.35 ± 0.01 |
| 23.0 | 7.40 ± 0.05 | n.a. | 2.39 ± 0.01 |
| 53.0 | 2.14 ± 0.05 | n.a. | 1.46 ± 0.01 |
| 146 | 0.76 ± 0.14 | n.a. | 1.48 ± 0.01 |

[a] Deaerated solution [b] Oxygen-enriched solution

***Table A6:*** *Tabulated emission decay time constants for TIPS-Pn in THF at varying concentrations.*

| Concentration /mM | $\tau_{Em}$ / ns |
|---|---|
| 0.50 | 12.0 |
| 1.00 | 12.3 |
| 2.00 | 11.7 |
| 5.00 | 10.2 |
| 10.0 | 8.30 |
| 20.0 | 5.72 |
| 60.0 | 2.22 |

## D.2 Time-Dependent Concentrations for Sequential SF in TIPS-Pn

In order to derive the analytical expressions for the time-dependent concentration of the individual species in sequential SF in TIPS-Pn, first the respective rate laws are devised, according to the model described in section 5.1.3. For the sake of conciseness and readability, the following definitions are applied: $k_{ET} \equiv k'_{ET}\left[{}^3O_2\right]$, $k_1 \equiv k_R + k_{ET}$, $k_2 \equiv k_{hSF}[S_0]$. This leads to the rate laws:

$$\frac{d[S_1]}{dt} = -k_1 t$$

$$\frac{d\left[{}^1O_2\right]}{dt} = \; k_{ET}[S_1] - k_2\left[{}^1O_2\right]$$

$$\frac{d[T_1]_{total}}{dt} = k_{ET}[S_1] + k_2\left[{}^1O_2\right] - k_3[T_1]_{total}$$

In order to integrate these differential equations, following boundary conditions are applied:

$$[S_1](0) = [S_1]_0$$

$$\left[{}^1O_2\right](0) = 0$$

$$[T_1]_{total}(0) = 0$$

Thus, the following time-dependent concentrations are obtained:

$$[S_1](t) = [S_1]_0 e^{-k_1 t}$$

$$\left[{}^1O_2\right](t) = [S_1]_0 \; \frac{k_{ET}}{k_1 - k_2}\{e^{-k_2 t} - e^{-k_1 t}\}$$

$$[T_1]_{total}(t) = [S_1]_0 \left\{ -\frac{k_{ET}(k_1 - 2k_2)}{(k_1 - k_2)(k_1 - k_3)} e^{-k_1 t} - \frac{k_{ET} k_2}{(k_1 - k_2)(k_2 - k_3)} e^{-k_2 t} + \frac{k_{ET}(2k_2 - k_3)}{(k_2 - k_3)(k_1 - k_3)} e^{-k_3 t} \right\}$$

The $T_1$ SADS obtained using this model show a constant amplitude over the whole concentration range. In contrast, using a simple sequential model exhibits significant changes in the intensities of the final SADS upon variation of the concentration (Figure A8). This contrast the notion, that the SADS are attributed to a single electronic species with the same, invariant absorption spectrum. In consequence, a sequential kinetic model does not accurately describe the experimental results.

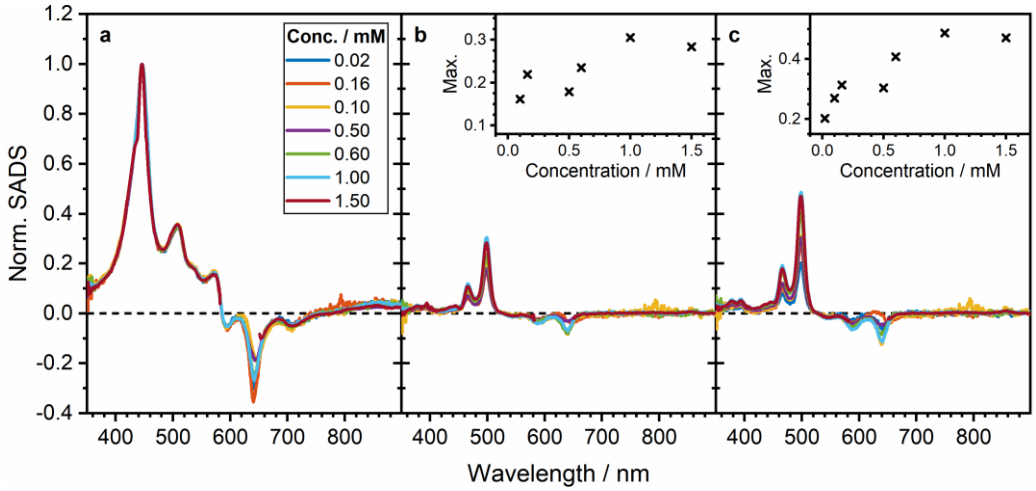


***Figure A8:*** *The SADS obtained for a simple sequential model exhibit significant variation in the amplitude of the final species.*

# E. Competing Sequential and Direct Singlet Fission in TDCl4

## E.1 Tabulated Time Constants

***Table A7:*** *Tabulated time constants for $TDCl_4$ in toluene at varying concentrations. Obtained by global multiexponential fits of short-time TA data.*

| Concentration /mM | $\tau_1$ / ps | $\tau_2$ / ns |
|---|---|---|
| 10.2 | 5.36 ± 0.08 | 7.54 ± 0.08 |
| 31.1 | 6.64 ± 0.05 | 4.80 ± 0.02 |
| 60.6 | 6.53 ± 0.07 | 1.93 ± 0.01 |
| 115 | 6.23 ± 0.16 | 1.15 ± 0.01 |

***Table A8:*** *Tabulated time constants for $TDCl_4$ in toluene at varying concentrations. Obtained by global multiexponential fits of long-time TA data.*

| Concentration /mM | $\tau_1$ / ns | $\tau_2$ / ns | $\tau_3$ / µs |
|---|---|---|---|
| 0.11 | 13.8 ± 0.2 | n.a. | 2226 ± 909 |
| 0.45 | 13.1 ± 0.1 | 240 ± 8 | 691 ± 15 |
| 0.48 | 13.7 ± 0.1 | 211 ± 21 | 693 ± 47 |
| 0.48[a] | 18.7 ± 0.1 | n.a. | n.a. |
| 0.95 | 15.1 ± 0.5 | 51.5 ± 4.8 | 680 ± 33 |
| 0.95[a] | 18.8 ± 0.1 | n.a. | n.a. |
| 1.42 | 12.4 ± 0.1 | 63.1 ± 0.8 | 719 ± 4 |
| 2.19 | 12.1 ± 0.1 | 40.9 ± 1.0 | 685 ± 5 |
| 4.61 | 10.4 ± 0.2 | 13.6 ± 0.5 | 691 ± 4 |
| 9.98 | 8.77 ± 0.24 | 14.9 ± 1.6 | 656 ± 8 |
| 40.7 | 4.69 ± 0.06 | n.a. | 644 ± 7 |
| 48.1 | 2.09 ± 0.06 | n.a. | 611 ± 8 |
| 61.4 | 2.18 ± 0.12 | n.a. | 603 ± 26 |
| 99.7 | 1.23 ± 0.06 | n.a. | 580 ± 5 |
| 115 | 1.18 ± 0.03 | n.a. | 584 ± 9 |

[a] Deaerated solution

***Table A9:*** *Tabulated emission decay time constants for $TDCl_4$ in toluene at varying concentrations.*

| Concentration /mM | $\tau_{Em}$ / ns |
|---|---|
| 0.11 | 15.3 |
| 0.19 | 14.9 |
| 1.42 | 13.9 |
| 9.98 | 8.97 |
| 42.3 | 3.89 |
| 61.4 | 2.69 |
| 87.9 | 1.62 |
| 114.75 | 1.46 |

## E.2 Oxygen-Dependent Triplet Formation

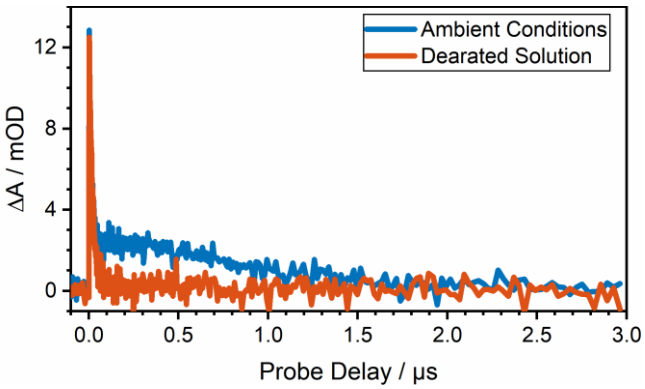


***Figure A9:*** *Transient of $TDCl_4$ in toluene at a probe wavelength of 570 ± 2 nm under ambient conditions (blue) and in a deaerated solution (orange). In an oxygen-free environment, no triplet formation is observable.*

## E.3 Time-Dependent Concentrations for Sequential and Direct Singlet Fission in $TDCl_4$

In the following, the analytical expressions for the time-dependent concentration of the individual species taking part in competing sequential and direct SF are derived (*cf.* Figure 5.12e). For the sake of conciseness and readability, the following definitions are applied: $k_{ET} \equiv k'_{ET}[\,^3O_2]$, $k_{dSF} = k'_{dSF}[S_0]$, $k_1 \equiv k_R + k_{ET} + k_{dSF}$, $k_2 \equiv k_{hSF}[S_0]$.

$$\frac{d[S_1]}{dt} = -k_1 t$$

$$\frac{d[\,^1O_2]}{dt} = k_{ET}[S_1] - k_2[\,^1O_2]$$

$$\frac{d[T_1]_{total}}{dt} = \left(k_{ET} + {}^1\!/_2\, k_{dSF}\right)[S_1] + k_2[\,^1O_2] - k_3[T_1]_{total}$$

In order to integrate these differential equations, following boundary conditions are applied:

$$[S_1](0) = [S_1]_0$$

$$[\,^1O_2](0) = 0$$

$$[T_1]_{total}(0) = 0$$

Thus, the following time-dependent concentrations are obtained:

$$[S_1](t) = [S_1]_0 e^{-k_1 t}$$

$$[\,^1O_2](t) = [S_1]_0 \frac{k_{ET}}{k_1 - k_2}\{e^{-k_2 t} - e^{-k_1 t}\}$$

$$[T_1]_{total}(t) = [S_1]_0 \left\{ \left( -\frac{(k_{ET} + 2k_{dSF})}{k_1 - k_T} + \frac{k_{ET} k_2}{(k_1 - k_2)(k_1 - k_3)} \right) e^{-k_1 t} - \frac{k_{ET} k_2}{(k_1 - k_2)(k_2 - k_3)} e^{-k_2 t} + \left( \frac{(k_{ET} + 2k_{dSF})}{k_1 - k_3} + \frac{k_{ET} k_2}{(k_2 - k_3)(k_1 - k_3)} \right) e^{-k_3 t} \right\}$$

## Danksagung

Dr. Tiago Buckup hat diese Dissertation ab 2018 betreut, nachdem Prof. Dr. Marcus Motzkus bereits ein Jahr nach Beginn meiner Promotion krankheitsbedingt nicht mehr anwesend sein konnte und leider viel zu früh verstarb. Sein Tod hat uns alle sehr getroffen und ich werde ihn in guter Erinnerung behalten.

Ich danke Dr. Tiago Buckup für die sehr gute Betreuung meiner Arbeit. Du hast mich während der vergangenen drei Jahre immer unterstützt. Die gründlichen, lehrreichen und engagierten Besprechungen mit Dir sowohl für meine Veröffentlichungen als auch für diese Dissertation waren mitentscheidend, dass ich diese wissenschaftliche Arbeit jetzt so vorlegen kann. Dafür danke ich Dir sehr herzlich. Nicht nur fachlich, sondern auch menschlich hast du mir immer mit Rat und Tat zur Seite gestanden.

Prof. Dr. Andreas Dreuw danke ich für seine Bereitschaft, das Zweitgutachten zu übernehmen. Sie haben meinem Semester zu unserem Bachelorabschluss in Ihrer Funktion als Studiendekan geraten, über den Tellerrand zu blicken. Auch deshalb habe ich die richtige Entscheidung getroffen, zum Masterstudium nach Marburg zu wechseln.

Bei Prof. Dr. Hans-Robert Volpp bedanke ich mich für die Koordination des PC-Praktikums und die vielen interessanten Gespräche.

Dr. Luis Lustres, zusammen standen wir im März 2017 in einem leeren Raum im CAM. Ohne dich wäre es nicht möglich gewesen, daraus ein funktionierendes Laserlabor zu gestalten. Auch konnte ich immer auf dich zählen, wenn ich Fragen zu wie auch immer gearteten Problemen hatte.

Nicolò Alagna, we share so much more than just the office: our humour, passion for good (Italian) food, video games…I am looking forward to visiting your Trattoria!

Auch bei Dr. Niklas Müller, Florian Nicolai, Dr. Zhuoran Kuang, Felix Hainer, Dr. Partha Roy, Martin Maier, Oskar Kefer, Dr. Yang Li und Dr. Nicholas Paul möchte ich mich dafür bedanken, dass ihr die letzten knapp vier Jahre zu einer unvergesslichen Zeit gemacht habt. Ich werde es vermissen, mit euch zu arbeiten.

Bei Victor Brosius, Sebastian Hahn, Benjamin Günther, Felix Berger und Vaishnavi Rao möchte ich mich für die erfolgreiche Zusammenarbeit danken.

Ein weiterer Dank gilt Marina Sommer und Angelika Neuner. Eure fröhliche Art hat den Umgang mit der universitären Bürokratie erträglich gemacht.

Auch möchte ich mich bei Dr. Olaf Skibbe und Martina Anselmann bedanken. Ihr habt dafür gesorgt, dass die Arbeit am CAM ins Rollen kam und ich ungestört forschen konnte.

Zudem bedanke ich mich bei meinen Kommilitonen aus Heidelberg und Marburg. Trotz anstrengenden Laborpraktika und stressigen Klausurphasen und Promotion in verschiedensten Städten haben wir uns nicht aus den Augen verloren. Ich hoffe ihr wisst, wie viel mir das bedeutet.

Zuletzt danke ich meiner Familie, insbesondere meiner Freundin Sarina Becker. Ihr habt mir stets dabei geholfen, die richtigen Entscheidungen zu treffen, meine Hochs mit mir gefeiert und mir bei meinen Tiefs beigestanden. Ich wüsste nicht, was ich ohne euch machen würde.